Dosimetry and Radiobiology of Ultrahigh Dose-Rate Radiotherapy Delivered with Low-Energy X-rays and Very High-Energy Electrons

by

Alexander Hart
MSc, University of Victoria, 2021

A Dissertation Submitted in Partial Fulfillment of the
Requirements for the degree of

Doctor of Philosophy

in the Department of Physics and Astronomy

Dosimetry and Radiobiology of Ultrahigh Dose-Rate Radiotherapy Delivered with Low-Energy X-rays and Very High-Energy Electrons

by

Alexander Hart
MSc, University of Victoria, 2021

Supervisory Committee

Dr. Magdalena Bazalova-Carter, Supervisor
Department of Physics and Astronomy

Dr. Steve Perlman, Outside Member
Department of Biology

Dr. Wayne Beckham, Departmental Member
Department of Physics and Astronomy

Abstract

Radiotherapy is a powerful tool in oncology, from curative treatments to pain relief in palliative care. However, the efficacy of radiotherapy is limited by side effects caused by damage to healthy tissues. Ultrahigh dose-rate radiotherapy (UHDR-RT) has emerged as a possible method of reducing damage to normal tissues while maintaining the ability to control the progression of cancer. UHDR treatments are delivered three orders of magnitude faster than conventional dose-rate radiotherapy (CDR-RT). To reach the dose rates associated with UHDR-RT, novel radiation sources have been developed, spanning a wide range of radiation types, energies, and time structures of delivery. These include kilovoltage x-rays produced by a shutter-controlled x-ray tube, and very high energy electrons (VHEE) accelerated to 200 MeV at high energy physics laboratories. Testing the capability of these sources requires specialized dosimeters and radiobiological models which are not commonly used in traditional radiotherapy.

In this work, plastic scintillation detectors (PSDs) of various compositions were used to measure dose from both 120 kVp x-rays and 200 MeV electrons. Experiments with the shutter-controlled x-ray tube demonstrated that lead-doped polystyrene PSDs can be used as accurate dosimeters for dose-rates of up to 40.1 Gy/s and for pulse widths of 1 - 100 ms. At the CERN linear electron accelerator for research (CLEAR) the ability of PSDs to respond linearly with dose and independent of dose rate with 200 MeV electrons was assessed as well as the radiation hardness of the probes. Polystyrene-based PSDs maintained linear light output with dose up to 125.2 Gy per pulse. After receiving tens of kGy within one day, PSDs showed reduced light output. However, they exhibited dose-dependent recovery, and maintained linearity of output with dose per pulse.

To explore the radiobiological effects of the same radiation sources, *Drosophila melanogaster* were irradiated as larvae and were monitored for effects on their development. It was shown that UHDR 120 kVp x-rays are capable of reducing normal tissue damage in flies compared to CDR treatments. At 22 Gy, the UHDR irradiated flies had a longer median lifespan, while at 24 Gy they survived to adulthood at higher rates than the corresponding CDR groups. Irradiations of *D. melanogaster* with 200 MeV and 9-20 MeV over a range of doses from 10 - 45 Gy at both UHDR and CDR were also performed. The dose response curves allowed for an *in vivo* determination of the relative biological effectiveness (RBE) of VHEE beams, calculated to be between 0.97 and 1.01. This work establishes that PSDs and *D. melanogaster* are useful platforms for characterizing the physical and radiobiological properties of novel UHDR-RT sources.

Contents

List of Tables

List of Figures

Acknowledgements

First and foremost, I wold like to thank Magdalena Bazalova-Carter for her excellent supervision. I am indebted to her for her tireless support, veritable encouragement, and occasional hard truths. Most of all, I appreciate the freedom she gave me to do the work that interested me most. One of my main motivations for pursuing a PhD was to develop the independence and creativity to pose questions worth asking and to chase down the answers. Thank you for helping me towards that goal.

It has been a great privelege to be a member of the XCITE lab for the past three years. I have learned so much from members past and present, and the hill would be a lot steeper to climb without each of your help. I would like to give special thanks to Nolan Esplen, Jon Eby, and Jade Fischer for helping me to wrangle flies.

My project would have been impossible without a very long list of collaborators who were incredibly generous with their time and expertise. I would like to thank the Perlman lab, especially Jan Dudzic and Jameson Clarke for educating me on fruit flies and entertaining my mad scientist impulses. Without my friends in Quebec, Cloe Giguere and François Therriault-Proulx, I would know a lot less about optical dosimetry. It still seems like a fever dream that my project involved multiple trips to CERN to irradiate fruit flies. Thank you to everyone at CLEAR and EPFL for enabling this project, especially Manjit Dosanjh, Joseph Bateman, Vilde Rieker, and Thomas Esmangart de Bournonville.

I think my PhD would have taken significantly longer if I didn't have such an amazing community of friends helping me stave off burnout. Thank you to Hayley Smith, Liam McDougal, Matt Gwilliam, Kirsten Aasen, and Jericho O'Connell for putting up with me. I am really thankful for all the wonderful people who have joined the Salish sea swimmers. Thank you for teaching me that uncomfortable things are worth leaning into. I never regret a cold swim. And to Devon Richtsmeier, thank you for being there through it all these past five years.

Finally, I would like to acknowledge my wonderful family. The ways that they have supported me throughout my education are too many to enumerate here. It is a great privilege to be able to spend years pursuing a PhD and I owe that to them.

Chapter 1

Introduction

Cancer is one of the leading causes of death worldwide, and is the top cause of mortality for Canadians. As of 2021, it is estimated that 40% of Canadians will receive a cancer diagnosis during their lifetimes, and 25% will die from it [1]. The most common types of disease include lung, breast, colorectal, and prostate cancers, all of which can be treated effectively with radiation therapy alone or in combination with chemotherapies. Currently, radiation therapy is used in approximately 50% of all cancer cases, which includes both curative and palliative treatments [2].

Following Lord Roentgen's 1895 discovery of x-rays, radiation was immediately translated into clinical practice. One year later, and just three days after announcing Roentgen's discovery, Emil Herman Grubbe treated a breast cancer patient with kilovoltage x-rays produced by an x-ray tube [3]. During the next several years, Henri Becquerel discovered radioactivity, and Marie and Pierre Curie began to explore the biophysical effects of radium [4]. From the first uses of radiation as a cancer therapy, clinicians and patients observed control of tumour progression, and pain relief. However, it would be decades before even a partial understanding of the biological mechanism of radiation, or *radiobiology*, would be developed. Radiation therapy primarily works by damaging deoxyribonucleic acid (DNA) in tumour tissues. When the tumour cells fail to repair the damage, the effect is *cytotoxic*, or lethal to the tissue. The rapid proliferation of cancer cells stops, and the growth of the tumour is controlled [5]. Of course, normal tissues are also susceptible to radiation damage, which manifest as side effects including burns, bleeding, and loss of organ function. These normal tissue toxicities limit the dose that can be delivered to the tumour.

Modern radiation therapy has advanced by developing tools to sculpt dose distributions around a patient's anatomy, protecting organs-at-risk (OARs) and maximizing the damage to the tumour. The most common radiotherapy techniques employed in Canada, center on using electron linear accelerators to deliver megavoltage x-ray treatments. These machines feature x-ray image guidance to make sure the dose is delivered to the target, and use

digitally controlled multi-leaf collimators (MLCs) to shape the beam, all contained within a rotating gantry system as shown in Figure 1.1. In the last 50 years, significant work has been done to develop techniques for intensity modulated radiotherapy (IMRT), in which treatments are delivered from different beam angles and intensities to improve the resulting dose distributions. The pinnacle of this work was Karl Otto's volumetric modulated arc therapy (VMAT) which uses a dynamic MLC aperture and fluctuating dose-rate within a 360 degree delivery to limit dose to OARs [6]. An example of a planned VMAT dose distribution is shown in Figure 1.2.

Figure 1.1: A Varian TrueBeam linear accelerator (Palo Alto, California, USA) which is used to treat patients with megavoltage electron and x-ray beams. [7]

Medical physicists and radiation oncologists have also explored radiation modalities other than electrons and x-rays produced by ∼20 MeV linear accelerators in an effort to tailor physical dose distributions to specific disease sites and patient anatomy. This has included using protons to treat ocular melanomas [9] and pediatric patients [10], as well as heavy ion beams to target deep-seated tumours. On the frontier of radiotherapy are very high-energy electrons (VHEE), which have energies of 100 - 250 MeV. VHEE beams deposit their energy much deeper in tissue than 20 MeV electrons and can result in physical dose distributions that protect OARs [11]. They may also cause different amounts of biological damage for a given dose compared to megavoltage electrons and x-rays routinely used to treat patients. The

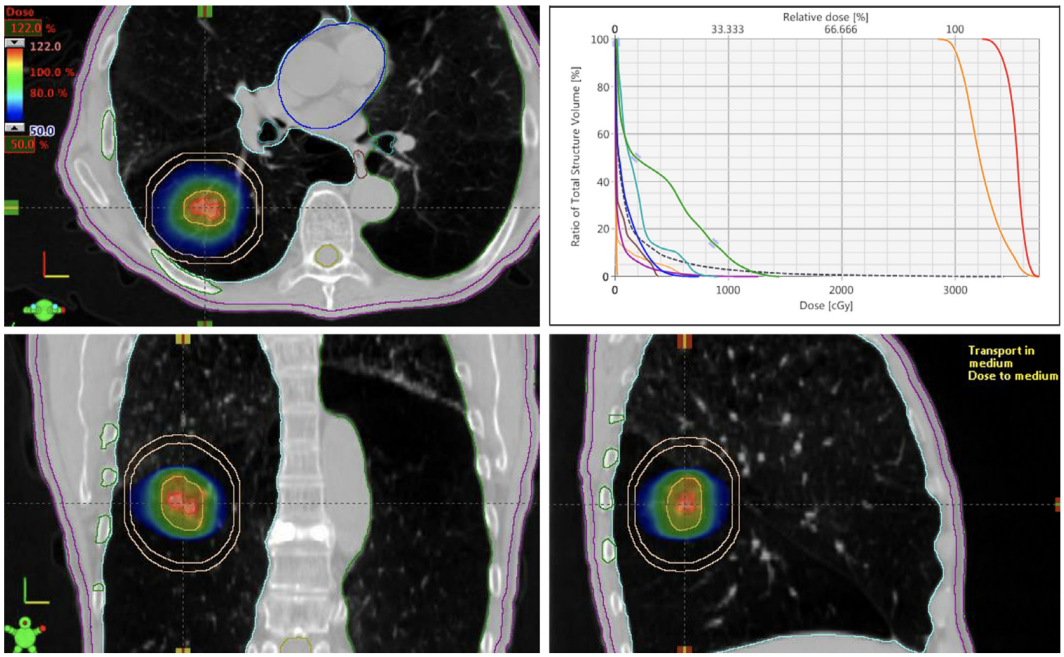

Figure 1.2: VMAT plan for treatment of a lung tumour with 6 MV x-rays. Axial, coronal, and saggital views of the dose distribution are shown (anti-clockwise from top left). The prescription dose is delivered to the planning treatment volume (PTV) contoured in orange. The dose volume histogram (DVH) shown in the top right displays the dose received by the PTV as well as several OARs including ribs, spinal cord, and normal lung. Adapted from Pokhrel *et al.* [8].

comparative magnitude of biological damage caused by different radiation beams is called the relative biological effectiveness (RBE). The RBE of new radiation modalities must be well characterized in order to predict the efficacy of radiotherapy treatments.

Another technique that has gained significant attention in the last decade is ultrahigh dose-rate radiotherapy (UHDR-RT), which is delivered approximately three orders of magnitude faster than conventional dose-rate radiotherapy (CDR-RT). Radiobiological research has shown promising results in exploiting UHDR irradiation to spare normal tissues while effectively controlling tumour progression, which is widely referred to as the FLASH effect [12, 13]. Over the previous decade, FLASH has been used to demonstrate a decrease in acute and late radiation toxicities while maintaining tumor cell kill [14]. The difference between the dose which causes intolerable normal tissue damage and the dose required to control the tumour growth is referred to as the therapeutic window, shown in Figure 1.3. By reducing the damage to normal tissues while maintaining the tumourcidal efficacy, this window can be widened.

UHDR-RT has been a gateway for physicists to bring technical innovations from high energy physics particle accelerators back to applications in cancer therapy for the first time

in several decades. This has unleashed a steady stream of new UHDR dedicated beamlines in experimental facilities, and companies investing in the development of new UHDR-capable clinical machines. However, in order to justify translating new delivery techniques into the clinic, a case must be made for the biological benefit of UHDR-RT relative to CDR-RT.

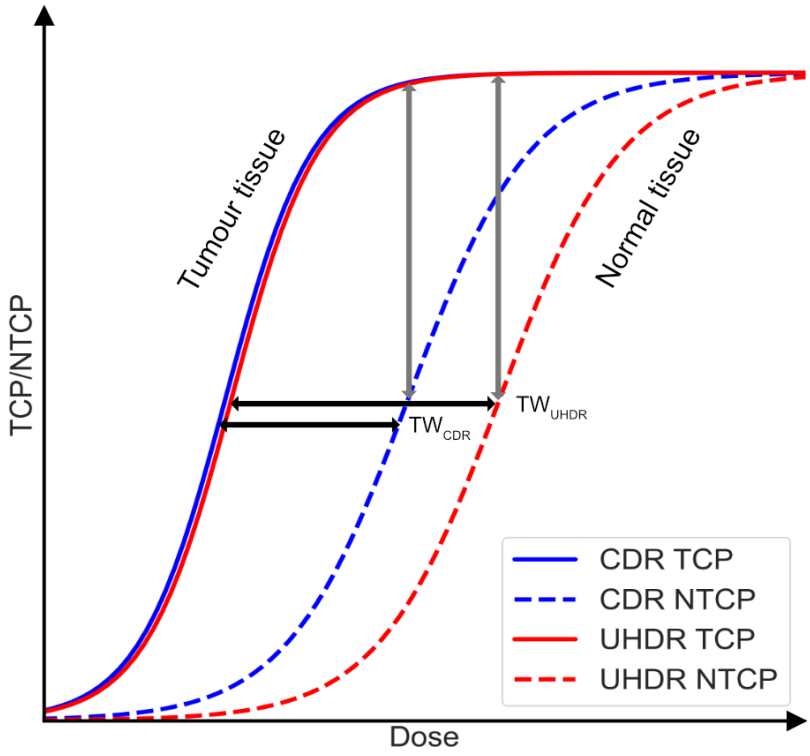

Figure 1.3: Depiction of the therapeutic window (TW) in radiotherapy and the hypothesized differential effect of UHDR-RT on normal and tumour tissues. Dose escalation increases the rates of both normal tissue complication probability (NTCP) and tumour control probability (TCP). By moving to UHDR from CDR treatments, the TCP may be increased for a given NTCP.

While the potential benefits of UHDR-RT are tantalizing, a rigorous characterization of the FLASH effect and the radiation sources that can cause it is needed before widespread clinical translation is advisable. Of the many challenges to this goal, the work presented in this thesis will deal with two: the dosimetry of UHDR sources, and the difference in radiobiological effects of sources operating at UHDR or CDR and at energies spanning kilovoltage x-rays and VHEE.

1.1 Contributions of this work

1.1.1 Plastic scintillation detectors

UHDR-RT neccesitates new radiation sources and/or delivery techniques with time structures that complicate the use of traditional dosimeters such as ionization chambers and radiochromic film. Plastic scintillation detectors (PSDs) are an alternative dosimeter with possible solutions to this problem. When irradiated, PSDs emit optical light of an intensity proportional to the absorbed dose [15, 16]. PSDs have high temporal resolution and have been suggested to be dose-rate independent, which may allow them to be used as online dosimeters of UHDR sources [17, 18]. In the work presented in this thesis, the response of PSDs were tested with kilovoltage x-rays and VHEE beams both operating at UHDR. The ability of PSDs to respond linearly with dose and dose-rate was assessed as well as the radiation hardness of various scintillator materials. The author performed all of the experiments and data analysis for the PSD investigations described in this thesis. The VHEE beamline was operated by staff at CERN.

Figure 1.4: The CLEAR VHEE beamline at CERN (a) and the author along with collaborators on VHEE experiments.

1.1.2 Fruit fly radiobiology

The understanding of the radiobiological effects of UHDR are still developing. While early clinical trials have begun using protons [19, 20], and UHDR electrons [21], the fundamental mechanisms behind the FLASH effect remain unclear. There are also less common radiation modalities being introduced as possible UHDR-RT sources, including kilovoltage x-rays and

VHEE. The biological effects of these beams need to characterized, preferably with a high-throughput model that would allow for insights into the mechanism behind the FLASH effect. *Drosophila melanogaster* are a potential model that has been used extensively in the past for radiobiology experiments and is currently used for cancer drug development. In this work, *Drosophila* were irradiated with both kilovoltage x-rays and VHEE. The physiological response of normal tissues to both CDR and UHDR was observed. The author performed all of the fly irradiations described in this thesis (with beam operation provided by CERN staff for VHEE experiments). Follow-up of flies and qPCR analysis for VHEE experiments was performed by collaborators at the EPFL. All data analysis presented was performed by the author.

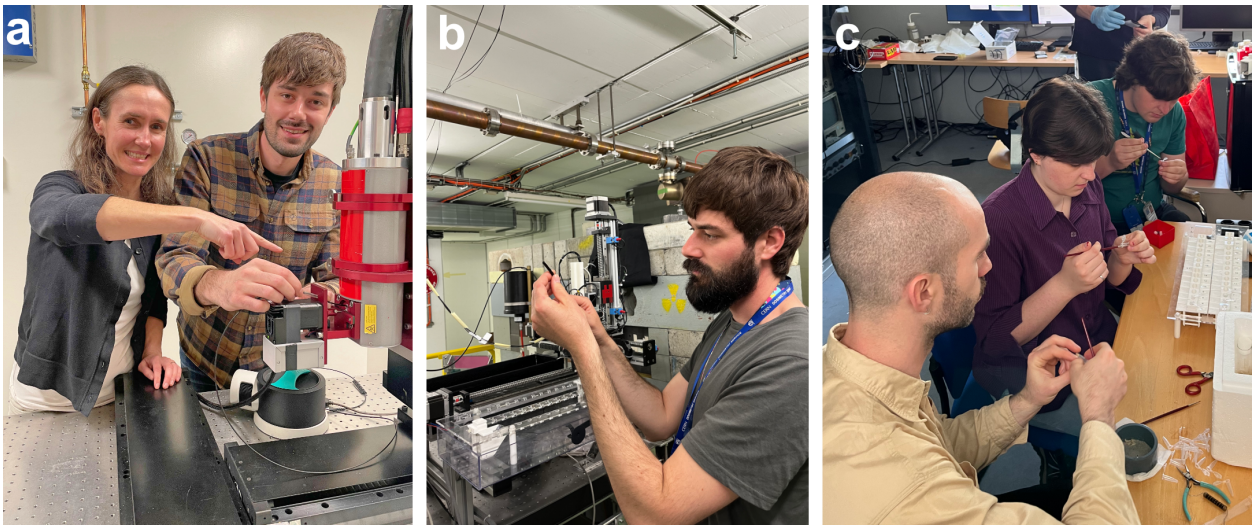

Figure 1.5: The author and his supervisor using PSDs to measure dose from kilovoltage x-rays (a), and VHEE (b). Collaborators immobilizing *Drosophila* larvae for irradiations (c).

1.2 Structure of the thesis

The first three chapters of this thesis are dedicated to the relevant background to contextualize the novel work presented here. Chapters 2, and 3 present the basic physics and radiobiology underpinning the experiments and summarize the state-of-the field. The following section of the thesis contains the novel contributions of this work. PSD dosimetry and fruit fly experiments with UHDR low-energy x-rays are detailed in chapters 4 and 5, respectively. VHEE studies follow in chapters 6 and 7. Finally, concluding remarks on the entire body of work and potential applications and future research directions are discussed in chapter 8. The author performed all irradiation experiments with PSDs and flies contained

within this work. Follow-up and care for the flies described in chapter 5 was principally done by the author with help from the Perlman lab. Post irradiation tracking of flies described in chapter 7 was handled by the Lemaitre lab. All data analysis presented in the thesis was conducted by the author.

Chapter 4 was published in *Physics in Medicine and Biology* in 2022 [22]. Chapter 6 was published in *IEEE Sensors* in 2024 [23]. Chapter 5 is under review for publication in the *Journal of Radiation Research* and won an award for best oral presentation at the FLASH Radiotherapy and Particle Therapy (FRPT) conference in Barcelona (2022). Chapter 7 is being prepared for manuscript submission, was presented at FRPT in Toronto (2023, oral presentation), and will be presented at the American Association of Physicists annual meeting in Los Angeles (2024, oral presentation).

Chapter 2

Physics of Radiation Therapy

Safe and effective radiation therapy is enabled by the development of precise and accurate dosimetry methods. This chapter is dedicated to describing the underlying physical principles and equipment used to produce and measure ionizing radiation. While these tools are well developed for CDR-RT, application to UHDR sources provides a new set of challenges.

2.1 Interactions of ionizing radiation with matter

To understand how radiation sources can deliver curative and biologically damaging doses, we must begin with the basic particle-level interactions between ionizing radiation and matter. For the work discussed in this thesis, the interactions of photons and electrons with matter are most relevant.

2.1.1 Photons

The likelihood of a particle undergoing any particular interaction type is referred to as the cross-section (σ). For x-ray beams, we also define the linear and mass attenuation coefficients (μ and μ/ρ), which are composed of the cross-section for all interaction types and depend on the energy of the photons. The mass attenuation coefficient can be used to describe how the intensity (I) of an x-ray beam decreases as it passes through a medium of density ρ, and thickness t according to

$$I = I_0 e^{-(\mu/\rho)\rho t} \tag{2.1}$$

where I_0 is the initial intensity of the x-ray beam. This section will describe each of the possible photon interactions and how they contribute to the total cross-section. The probability of any of these processes occurring, or *cross section*, depends on the atomic number of the medium (Z) and the energy of the incident photon (E).

Rayleigh scattering: Also called coherent scattering, Rayleigh scattering is an elastic collision between an incident photon and an entire atom. While the path of the photon is diverted, no energy is transferred in the process. The cross-section for Rayleigh scattering is proportional to $(Z/E)^2$.

Photoelectric effect: The photoelectric effect (PE) is the most dominant interaction for low-energy x-ray beams. PE contributes significantly to imaging dose and radiotherapy with orthovoltage beams but is less relevant to megavoltage radiotherapy. During a PE interaction, a photon interacts with an atom, ejecting an electron from its orbit, and the photon ceases to exist. The kinetic energy of the photon is completely transferred to the ejected electron. PE is dominant at photon energies below 100 keV, and the likelihood of interaction is proportional to Z^3/E^3. In the event that a PE interaction removes an orbital electron from an inner shell, an electron from a higher energy can *fall* to take its place, emitting a *characteristic* x-ray with energy equal to the difference in binding energies of the two electrons. The inner shell electron can also be replaced by another electron via internal conversion processes, resulting in the ejection of a *Meitner-Auger* electron [24]. These low energy electrons (1-10 keV) can also be exploited for cancer therapies [25].

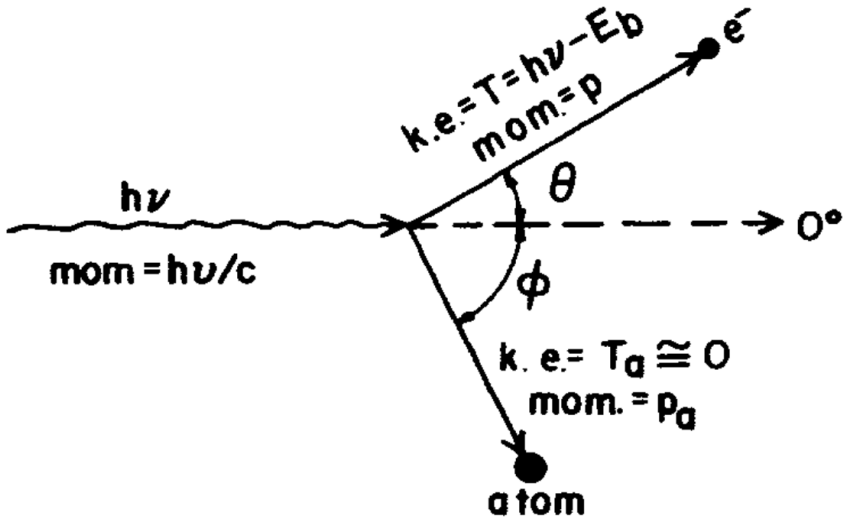

Figure 2.1: Depiction of a PE event. After the electron departs with angle, relative to the incident photon, the atom also recoils. Adapted from Attix [26].

Compton scattering: For radiotherapy with megavoltage linear accelerators, the dominant photon interaction is incoherent, or Compton scattering. In a Compton scattering event, the incident photon loses some of its energy through an inelastic collision with an orbital electron, continuing at a scattered angle, θ, dependent on the loss of energy. The

energy of the scattered photon is given by

$$h\nu' = \frac{h\nu}{1 + \alpha(1 - cos\theta)} \tag{2.2}$$

where $h\nu$ is the energy of the incident photon, $\alpha = h\nu/0.511$ MeV. The cross-section for Compton scattering is described by the Klein-Nishina formula, which decreases with increasing photon energy, and can be considered independent of Z [27].

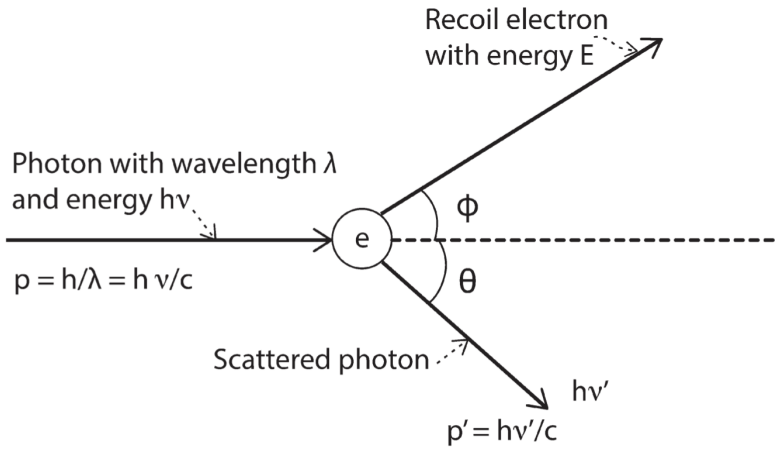

Figure 2.2: Kinematics of a Compton scattering event. Adapted from Johns and Cunningham [27].

Pair and triplet production: Energetic photons can also interact directly with the coulombic field of an atomic nucleus. If the incident photon has an energy exceeding the threshold of 1.022 MeV, the photon can be absorbed and produce an electron-positron pair. Triplet production can also occur if the interaction involves an orbital electron, resulting in kinetic energy being transferred to the created electron-positron pair as well as an original orbital electron. For triplet production to occur the threshold energy is raised to 2.044 MeV. Downstream from pair or triplet production, the positron will come to rest and annihilate with an electron, producing two 0.511 MeV photons. The cross-section for pair production roughly follows a logarithmic relationship with photon energy, increasing steeply above the threshold and then approaching a constant value. The cross-section is also proportional to Z. As shown in Figure 2.3, pair and triplet production becomes the dominant photon interaction with matter above energies of 10 MeV.

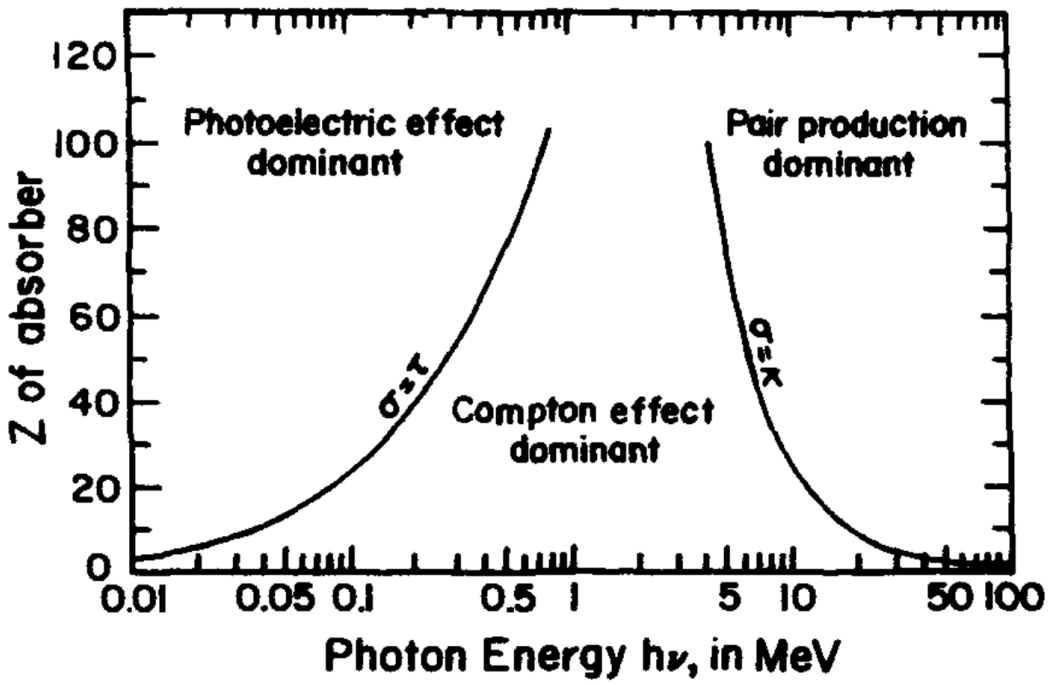

Figure 2.3: Dominance of photon interaction type as a function of Z and photon energy. Adapted from Attix [26].

2.1.2 Electrons

While energetic photons can transfer energy to matter through the interactions just described, it is primarily electrons that deposit dose by directly ionizing the irradiated medium. Electrons, either secondary electrons generated by x-ray beams or primary electrons produced by accelerators, interact with orbital electrons through Coulombic interactions. Electrons also lose energy by interacting with the electric fields surrounding charged particles and nuclei in a medium. As the path of the incident electron is deflected, it loses kinetic energy be emitting *bremsstrahlung* x-rays (the German term for 'braking radiation'). The bremsstrahlung x-rays carry energy away from the site of their production and deposit dose downstream through creation of secondary electrons, also called delta rays.

Stopping power: To quantify the loss of energy from electrons as they pass through a medium, we use *stopping power*, which is defined as the energy lost per path length by a charged particle, and is typically described in units of [MeV/cm] or [keV/μm]. Stopping power is divided into two sub-quantities: radiative and collisional. The radiative stopping power is the energy lost through bremsstrahlung photons and is not accounted for in absorbed dose. Collisional stopping power refers to the loss of energy through ionizations, and for electrons is defined by

$$S_{col} = \frac{1}{\rho}\left(\frac{dE}{dX}\right)_{col} = 2\pi r_0^2 N_e \frac{\mu_0}{\beta^2}\left[\ln\frac{E^2(E+2\mu_0)}{2\mu_0 I^2} + \frac{E^2/8 - (2E+\mu_0)\mu_0 \ln 2}{(E+\mu_0)^2} + 1 - \beta^2 - \delta\right] \tag{2.3}$$

where N_e is the number of electrons per gram, E is the kinetic energy of the electron, μ_0 is the rest mass ($\mu_0 = m_0c^2$), β is the relativistic speed, and I is the mean excitation energy. The final term in brackets, δ, is a density correction term that reduces the effect of the electric field at a distance from the incident electron. This formalism was first described by Bethe and Heitler [28]. An approximation for the radiative stopping power is given by

$$S_{rad} = \frac{1}{\rho}\left(\frac{dE}{dX}\right)_{rad} = 4r_0^2 \frac{N_e Z E}{137}\left[\ln\frac{2(E+\mu_0)}{\mu_0} - \frac{1}{3}\right] \tag{2.4}$$

A closely related quantity to collisional stopping power is the *linear energy transfer* (LET), also called the *restricted* stopping power, which is used to describe the energy deposited locally per path length of a radiation beam. LET and stopping power have the same units. LET is considered more relevant to the biological damage caused by radiation than stopping power and can be useful in assessing the relative effectiveness of different particle types and energies [29]. LET can be calculated using

$$\begin{aligned} L_\Delta &= \frac{1}{\rho}\left(\frac{dE}{dX}\right)_{col} \\ &= 2\pi r_0^2 N_e \frac{\mu_0}{\beta^2}\left[\ln\frac{2(E+2\mu_0)(E-\Delta)\Delta}{\mu_0 I^2} + \frac{E}{E-\Delta} + \frac{\frac{\Delta^2}{2} + \mu_0(2E+\mu_0)\ln(\frac{E-\Delta}{E})}{(E+\mu_0)^2} + 1 - \beta^2 - \delta\right] \end{aligned} \tag{2.5}$$

where the symbols have the same meaning as in equation 2.3, with the addition of an energy cutoff term, Δ. The Δ term governs the energy limit of the delta rays that will contribute to LET. As Δ increases, so does the LET, reaching the unrestricted S_{col} at its limit. The collisional and radiative stopping power as a function of electron energy for water, polystyrene, and tungsten is shown in Figure 2.4. The collisional stopping power is proportional to Z, and decreases with increasing electron energy. For VHEE beams, the radiative stopping power becomes significant.

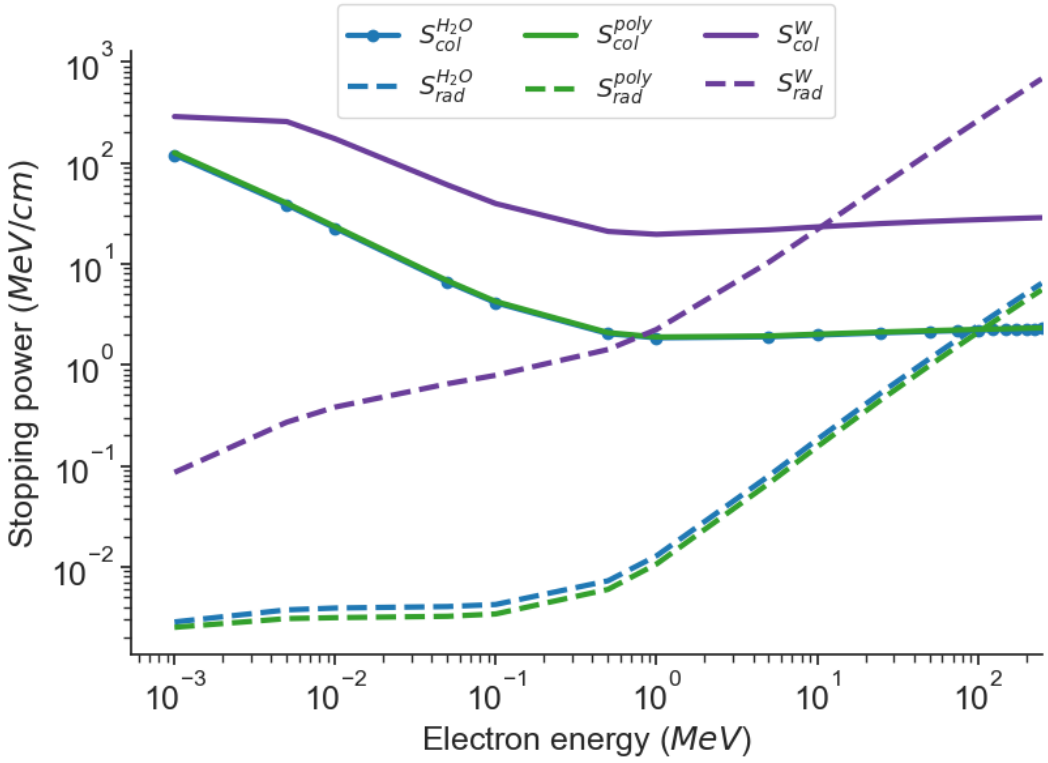

Figure 2.4: Radiative and collisional stopping power of electrons in water, polystyrene, and tungsten calculated from NIST ESTAR database [30].

Cherenkov: Electrons deposit the vast majority of their energy when their path intersects with or travels very close to other charged particles or nuclei. However, they can also weakly interact with atoms at greater distances, exciting orbital electrons and losing only a few eV. This energy transfer is negligible in the context of radiological beams, accounting for less than 0.1% of the energy lost [26]. As the excited orbital electrons relax, they emit a bluish light called *Cherenkov* radiation. The angle of the emitted light, θ, relative to the path of the electron is given by

$$\theta = arccos\left(\frac{1}{\beta n}\right) \tag{2.6}$$

where n is the index of refraction of the medium. As the electrons traverse the medium, unaffected by the index of refraction, they are able to travel faster than the generated Cherenkov light (in the medium). This leads to a kind of optical *sonic boom*, a blue flash observable even by the naked eye under the right conditions. Under the high intensity conditions of UHDR VHEE beams, the Cherenkov light is visible using a normal optical camera as shown in Figure 2.5. There is a material dependent energy threshold for the production of Cherenkov. For water the threshold is 264 keV [31].

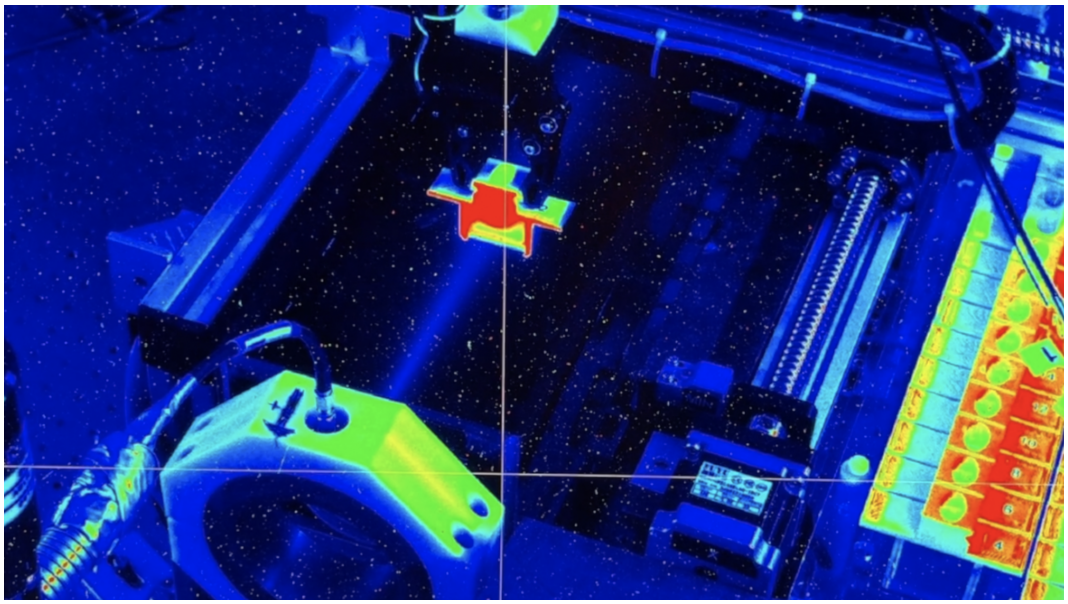

Figure 2.5: A cone of Cherenkov light produced by a UHDR VHEE beam travels through a water tank.

2.2 UHDR Radiation Sources

UHDR-RT has been studied with many different sources and radiation types including electrons, x-rays, protons, and other heavy ions. The vast majority of pre-clinical radiobiological studies and clinical trials have been conducted with 6-20 MeV electron linear accelerators [32], proton cyclotrons [19], and x-ray synchrotorons [33]. There are advantages of using different particle types and energies for specific treatment sites, based on their geometry and position relative to OARs. An important characteristic of a radiation beam is the percent depth dose (PDD), which describes the relative dose deposition as a function of depth in tissue. Figure 2.6 shows the PDDs for x-rays produced by a 120 kVp x-ray tube as well as electrons ranging in energy from 5 to 250 MeV. Kilovoltage x-rays deposit most of their dose at the surface, making them ideal for treating superficial lesions without damaging normal tissues below, but generally inadequate for targeting deeper tumours. Electrons produced by clinical linear accelerators are usually in the range of 6-20 MeV and penetrate a few cm into tissue before exhibiting rapid dose fall off at greater depths, making them also best suited for superficial lesions and post operative radiotherapy. Proton depth dose curves (not pictured in Figure **??**) feature a narrow*Bragg peak* at depth where a large amount of energy is deposited. This makes protons very effective at delivering conformal dose distributions around radiosensitive anatomy and are often employed for pediatric cases where secondary cancers are a major concern. Proton cyclotrons are significanly more expensive than conven-

tional x-ray and electron devices which prevents their widespread use in radiotherapy clinics. VHEE beams are able to target much deeper tumours than 6-20 MeV electrons, due to their reduced lateral scattering [34]. They are also less susceptible to range uncertainties caused by heterogeneous tissues than proton beams of similar energies [35].

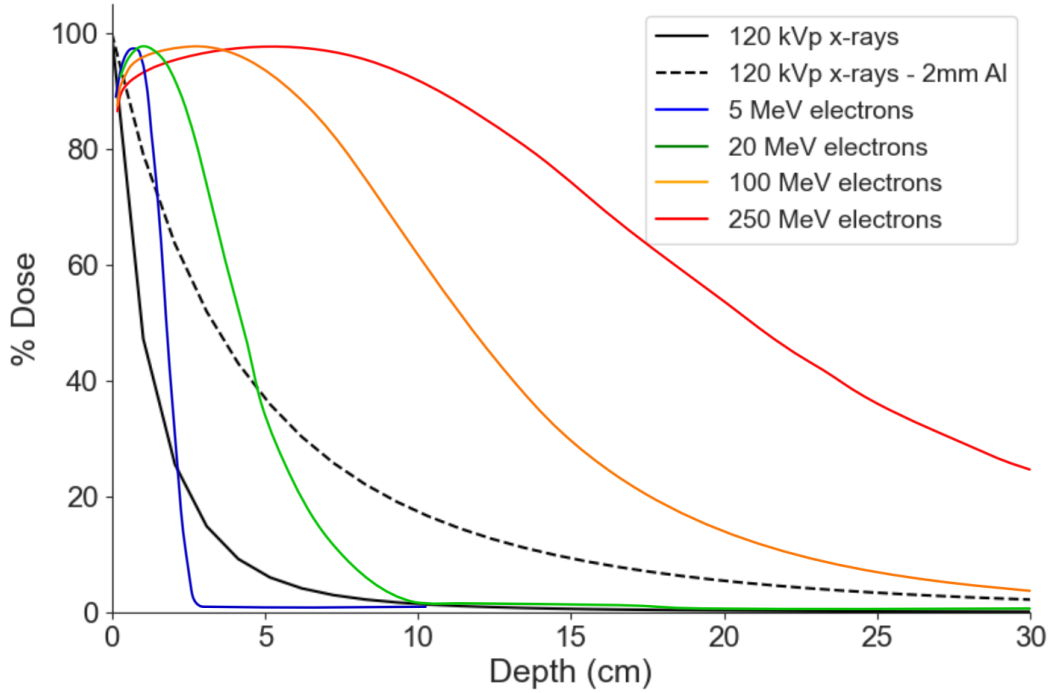

Figure 2.6: PDDs of 120 kVp x-rays with and without 2 mm Al filtration compared to electrons ranging from 5 to 250 MeV.

Throughout this thesis, beams are referred to as UHDR which cover a wide range of parameters. UHDR Dose rates referred to as UHDR are broadly categorized by the lower limit on average dose rate of 40 Gy/s, which are approximately three orders of magnitude higher than CDR dose rates. However, an extremely broad range of average dose rates have been referred to as UHDR, from 10^2 Gy/s [36] to 10^8 Gy/s [37]. Additionally, the fine details of the time structure used to deliver the dose may be as or more important than the average dose rate. The dose-per-pulse, dose rate within the pulse, inter-pulse spacing, number of pulses, and total delivery time may all have significant impacts on the biological effects of the beam. The effect of dose rate within the pulse and delivery time are described in Figure 2.7. For these reasons any conflation of the term UHDR and the advantageous biological effects of FLASH should be cautioned and one should also be careful to detail as many parameters of the time structure of dose delivery as possible.

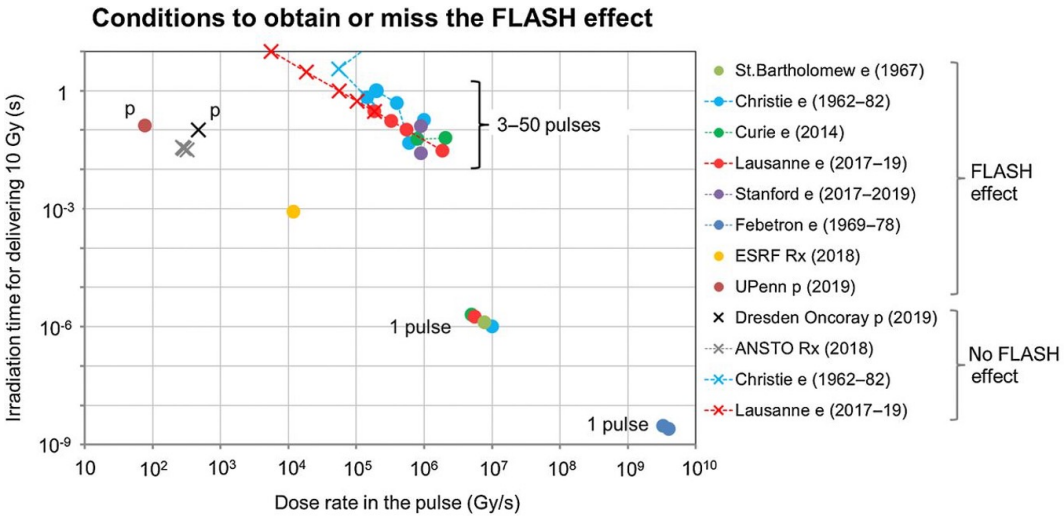

Figure 2.7: The ability to elicit the FLASH effect may depend on the pulsed dose rate and total delivery time. Adapted from Montay-Gruel *et al.* [38].

The work described in this thesis is bipartite, with the first half devoted to the measurement and radiobiological effects of UHDR kilovoltage x-rays, while the second half will discuss experiments with electron beams spanning conventional energies (9-20 MeV) up to 200 MeV VHEE. Following is a description of the relevant radiation sources and the state of the field regarding their development and use.

2.2.1 Kilovoltage x-ray sources

To produce kilovoltage x-rays, a cathode ray tube accelerates electrons from a cathode to an anode in the presence of an electric field provided by a high voltage source. The anode is made of a high-Z material, typically tungsten due to its elevated melting point. Upon collision with the anode, electrons deposit their energy and emit bremsstrahlung x-rays as shown in Figure 2.8.

The spectrum of x-ray energies produced by an x-ray tube is determined by the material of the anode, and the *tube voltage* or strength of the electric field provided by the high voltage source. The energy of x-ray tubes are typically described by their tube voltage in units of peak kilovoltage (kVp), which is the maximum energy of the bremsstrahlung x-rays emitted from the anode. Filtration of the x-rays results in *beam hardening*, or an upwards shift of the mean energy as shown in Figure 2.9. This results in a more penetrating beam, as shown in the 120 kVp beams with and without filtration in Figure 2.6, but also reduces the intensity. For the UHDR x-ray tube experiments in this work, the beam intensity was maximized by using minimal filtration. Only the inherent filtration of the tungsten anode and beryllium window were used.

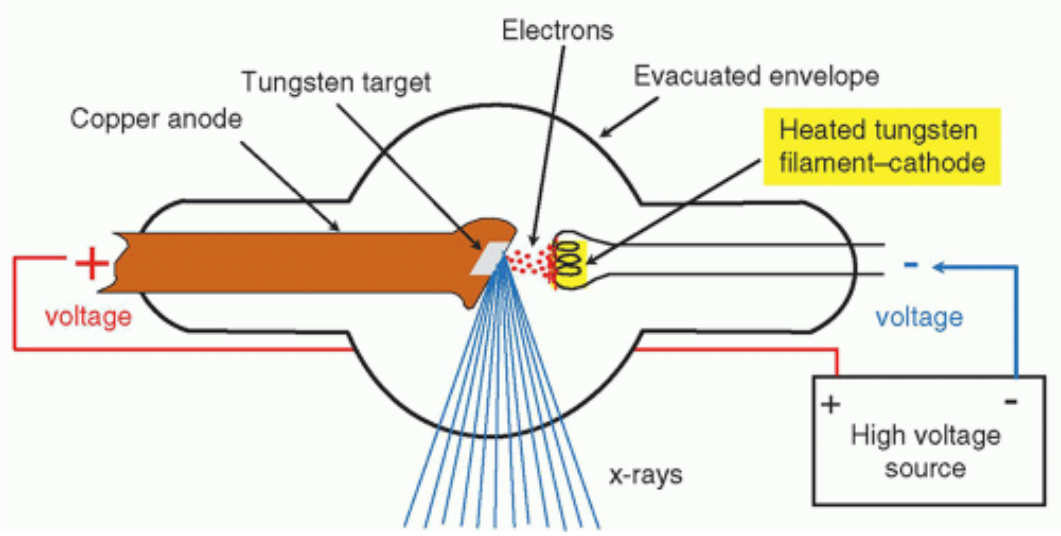

Figure 2.8: Schematic of a basic x-ray tube including evacuated chamber, hot cathode, and tungsten target mounted within the anode. Adapted from Bushberg [39].

The dose-rate of the x-ray tube is dependent on the rate of flow of electrons from the cathode to anode, or tube current (measured in mA). Other than increasing the tube current, the simplest way to increase the dose-rate of a radiation source is to reduce the source-to-surface distance (SSD). The intensity of isotropic radiation beams, including bremsstrahlung x-rays, follow an inverse square law (ISL) where $I \propto 1/SSD^2$. By reducing the SSD of a conventional 160 kVp diagnostic x-ray tube to less than 3 cm from the focal spot, Bazalova-Carter *et al.* demonstrated that dose-rates in excess of 100 Gy/s could be achieved [40]. This method has since been advanced by using dual x-ray tubes with rotating anodes in a parallel opposed geometry to improve the penetration depth and heat loading [41, 42]. Another limitation to x-ray tube based UHDR-RT is the ramp-up time for x-ray tubes to reach stable operation as well as terminating the beam at precise time intervals to control dose delivery. This has been overcome by utilizing a shielded aperture with a fast shutter [18]. The x-ray tube and shutter assembly used throughout this thesis is shown in Figure 2.10.

2.2.2 Megavoltage electron accelerators

Electrons with energies in the megavoltage range are most often produced by linear accelerators (linacs), which use radio-frequency (RF) electromagnetic waves to accelerate charged particles in a linear path within an accelerator waveguide [43]. The waveguide, an evacuated pipe with donut-shaped cavities, accelerates electrons through an oscillating electric field in the microwave range produced by a klystron. The waveguide design can be standing-wave or

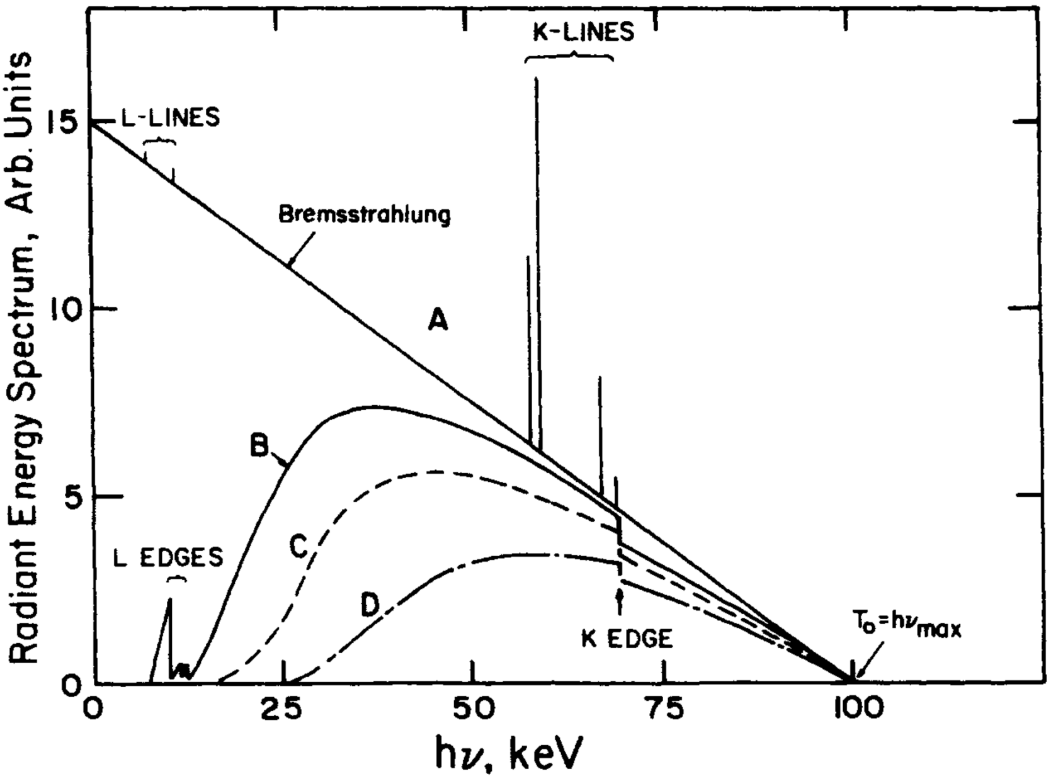

Figure 2.9: Spectra produced by a 100 kVp x-ray tube with varying levels of filtration including: none (A), 0.01 mm W anode filtration (B), additional 2 mm Al (C), 0.15 mm Cu and 3.9 mm Al in addition to anode filtration (D). Adapted from Attix (1986) [26].

traveling-wave, with standing-wave designs being more common due to their shorter length. In a linac, electrons gain energy from the electric field as they travel through the waveguide at relativistic speeds. Eventually the electrons can collide with a heavy metal target to produce bremsstrahlung x-rays used in cancer treatment as shown at the end of the diagram in Figure 2.11.

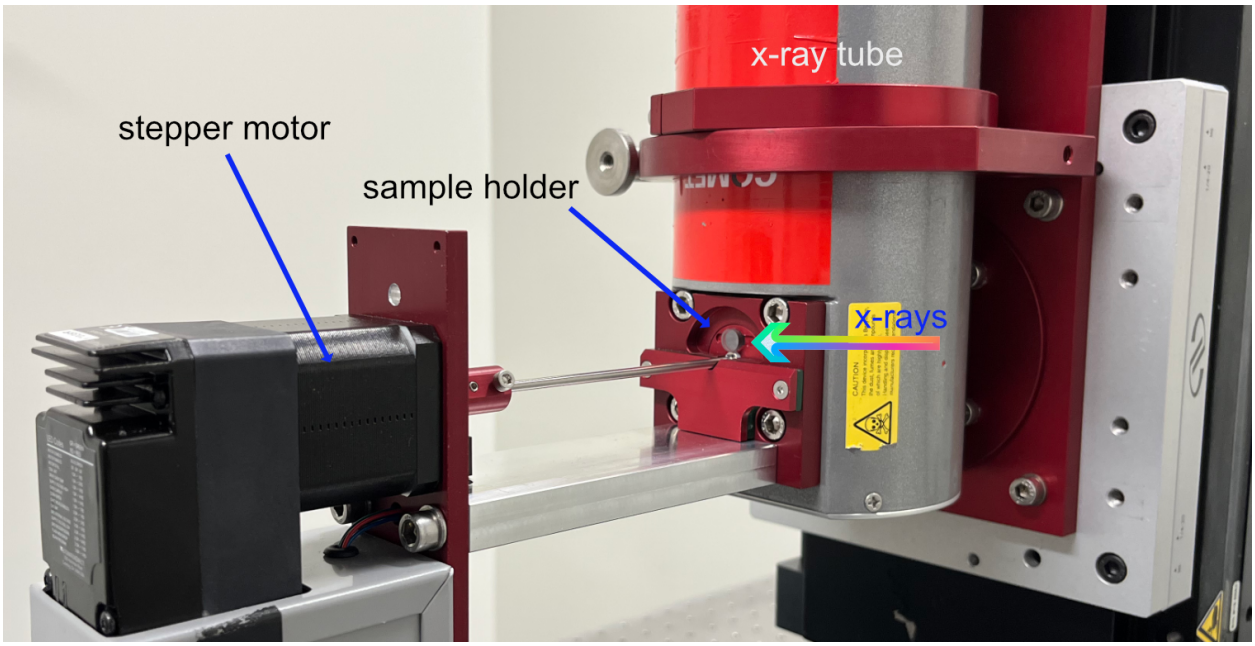

Figure 2.10: X-ray tube with shutter assembly attached. An acrylic cylinder used for immobilizing larvae is inserted into the sample holder.

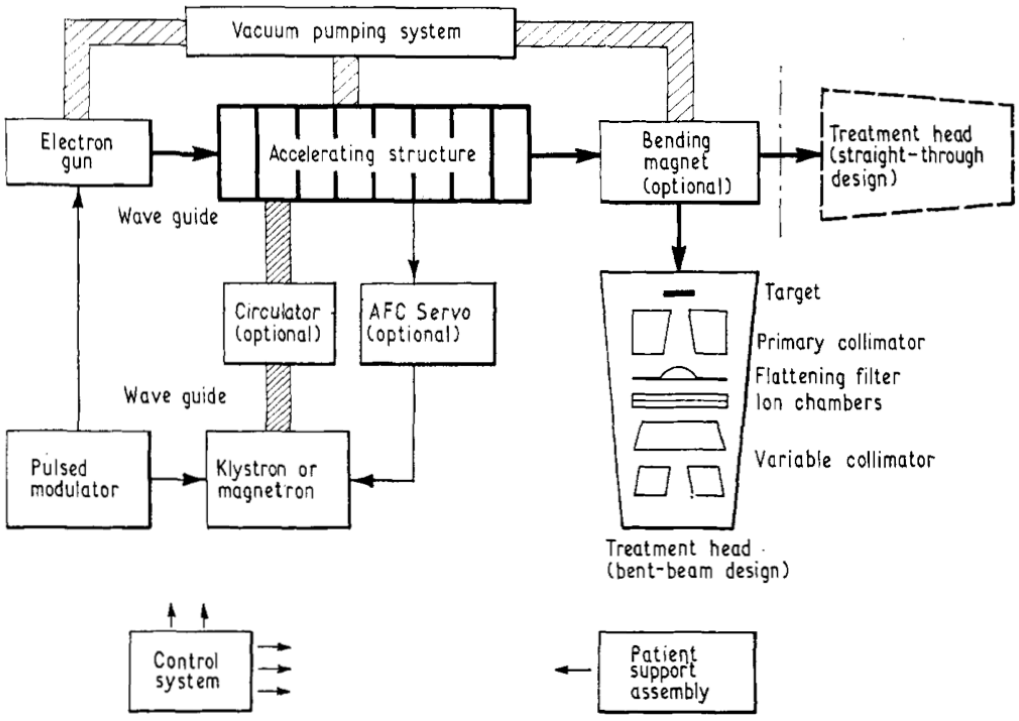

Figure 2.11: Diagram of a medical linac used for treating patients with x-rays produced by a conversion target. Linacs can treat patients with electron beams by removing the target and flattening filter from the beam path. Adapted from Karzmark [43].

The frequency of microwave power, and geometric design of the corresponding accelerating structures are determining factors in the efficiency and energy achievable by linacs. The linacs widely used in radiotherapy to accelerate electrons up to 20 MeV operate at S-band frequencies of ∼3 GHz. Recent developments in linac design have explored using C-band (4 - 8 GHz), and X-band (8 - 12 GHz) designs [44]. Higher frequencies allow for more efficient acceleration for a given waveguide length, but are limited by RF breakdown [45].

2.2.3 Very high energy electron accelerators

Historically, betatrons or racetrack microtrons were the first accelerators used to generate electrons at energies greater than 50 MeV [46]. These were prone to activation and high background dose rates, and did not catch on for clinical treatment. The VHEE source used for the experiments described in this work is the CERN Linear Electron Accelerator for Research (CLEAR) [47]. The accelerator technology used in the CLEAR beamline was originally developed at the Compact Linear Collider (CLIC), which was originally proposed as a potential successor to the large hadron collider (LHC) in the search for physics beyond the standard model [48]. The CLEAR facility, which evolved from CLIC Test Facility 3, currently uses the 25 m long CALIFES injector beamline followed by an additional 16 m beamline to accelerate electrons to 200 MeV. The beamline schematic is shown in Figure 2.12. CLEAR uses two 3 GHz klystrons, each delivering up to 120 MW per pulse at repetition frequencies of 10 Hz. Future plans for CLEAR include resuming studies with 12 GHz RF power to increase the acceleration gradient [49]. In contrast to the thermionic electron guns typically used by clinical linacs, the electron beam at CLEAR is generated by a laser-activated photo-cathode made of Cs_2Te [50]. The end of the user beamline features an in-air test stand which facilitates dosimetry and radiobiology experiments of VHEE beams [51, 52].

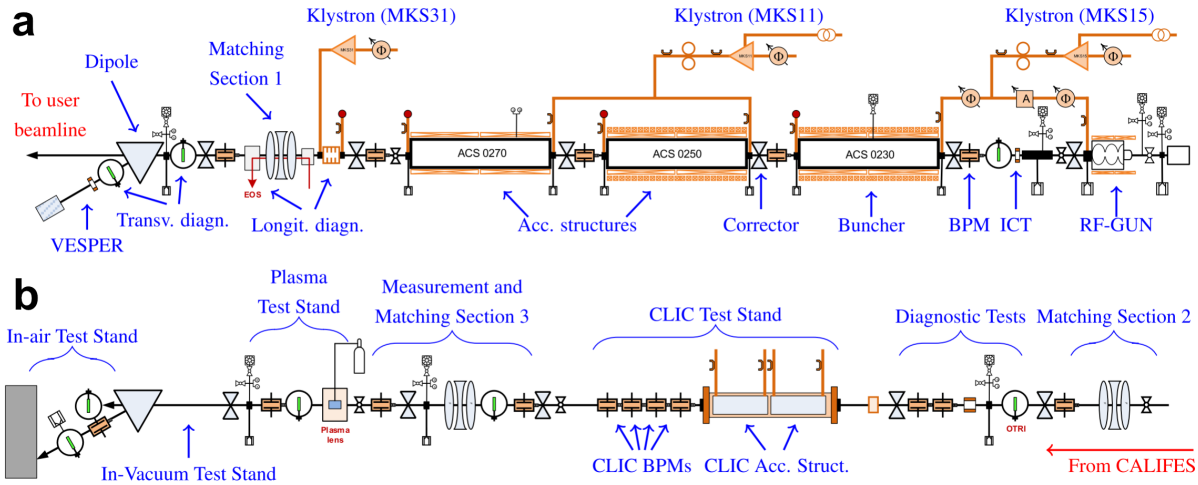

Figure 2.12: Schematic of the CLEAR beamline, including the CALIFES injector (a), and the user beamline (b). Adapted from Gamba [47].

At least two other test facilities have been proposed or are already built which will be capable of producing VHEE beams. In the UK, the Compact Linear Accelerator for Research and Applications (CLARA) accelerator uses an S-band accelerator to reach energies of 35 MeV. The design for the planned expansion to CLARA is to use a booster and additional S-band linacs to reach 250 MeV and operate at 100 Hz [53]. The Photo Injector Test facility at DESY in Zeuthen (FLASHlab@PITZ) currently produces 22 MeV electrons at UHDR utilizing a high brightness source [54]. PITZ can deliver bunch charges of up to 5 nC at MHz repetition rates which results in peak dose rates of up to 10^{14} Gy/s, making it the highest intensity source described here. There are plans to increase the beam energy to 250 MeV.

Clinicians and companies are looking beyond basic research with VHEE beams towards development of machines for clinical use. Researchers from Lausanne University Hospital (CHUV) and CERN have been collaborating with the company THERYQ to adapt the accelerator technology developed at CLIC and CLEAR into a commercial treatment machine, called FLASHDEEP. The machine is expected to produce electron beams with energies between 100 and 200 MeV [55]. At Sapienza/INFN, the SAFEST (SApienza Flash Electron Source for radioTherapy linac) is being developed using a C-band accelerating structure at 5.712 GHz [56]. The proposed design is expected to achieve energies between 60-160 MeV over a length of 3-4 meters, which would make it considerably more compact than current VHEE test facilities and would be compatible with existing medical linac vaults. Other experimental VHEE beamlines include the 170 MeV SPARC at INFN [57]. The beam parameters of various VHEE sources are summarized in Table 2.1.

Table 2.1: Comparison of beam parameters of current and proposed VHEE sources. *Denotes proposed expansions to currently existing linacs. Adapted from Fischer *et al. (submitted 2024)* and Ronga *et al.* [46]

Accelerator	Energy (MeV)	Repetition Rate (Hz)	Bunch Charge (nC)	Bunch Length (ps)	Dose rate (Gy/s)	Status
CLEAR	30 - 220	0.8 - 10	0.005 - 1.6	0.1 - 10	$>10^8$	Active
SAFEST	60-160	>100	0.035	20	$>10^6$	Proposed
CLARA	15-250	10	0.02 - 0.1	0.3 - 5	Not published	Proposed*
PITZ	22-250	1-10	<5	0.1-60	$>10^{14}$	Proposed*
SPARC	170	0.1-10	0.06	0.87	Not published	Active

2.3 Dosimetry

Absolute dosimetry methods, in which the measurement directly determines dose in Gy, include: *calorimetry* (dose dependent temperature change) [58], Fricke dosimetry (oxidation of ferrous ions into ferric ions) [59], and ionometric dosimetry (measurement of ion-pairs in a standard air chamber) [60]. These absolute dosimetry methods are typically laborious and fail to meet some of the other requirements of a practically useful dosimeter. Reference dosimeters can be calibrated in a standards lab to provide a measurement traceable to an absolute dosimeter. Relative dosimeters are typically cross-calibrated against reference dosimeters or normalized to specified conditions and then used to measure radiation sources with greater practicality.

2.3.1 Determination of absorbed dose

In radiation therapy, dose is defined by the energy deposited by charged particles per unit mass, and is measured in SI units of Gray (Gy), which are equivalent to [J/kG]. The dose delivered by a radiation source can be measured with either absolute or relative dosimeters. In the context of absolute dosimetry, the quantity of interest is *absorbed dose* which is described as $d\overline{E}_{ab}/dm$, where $d\overline{E}_{ab}$ is the mean energy imparted to an infinitesimal mass, dm [27]. Photon beams transfer energy to a medium by first imparting their energy to charged particles via the interactions described earlier in this chapter such as PE and compton. Immediately after the transfer of energy, a quantity called *Kerma* can be defined as

$$K = \phi \cdot (\mu/\rho) \cdot \overline{E}_{tr} \tag{2.7}$$

where ϕ is the photon fluence, μ/ρ is the mass attenuation coefficient, and $\overline{E}_{tr}$ is the average energy transferred to electrons in each interaction. After transferring their energy to electrons in the medium, all the energy is not immediately deposited by the electron. Some may be carried away and lost through bremsstrahlung further down the path, this results in Kerma and absorbed dose occurring in different locations. In the case where there is *charged particle equilibrium*, i.e. the same number of electrons entering a volume as leaving it, absorbed dose is defined as

$$D = \phi \left(\frac{\mu}{\rho}\right) \overline{E}_{ab} = K(1-g) \tag{2.8}$$

where $\overline{E}_{ab}$ is the kinetic energy transferred to electrons, g is the fraction of energy transferred to electrons that is subsequently carried out of the volume of interest by bremsstrahlung. The product of μ/ρ and $\overline{E}_{ab}$ is the mass energy absorption coefficient, μ_{ab}/ρ. To determine absorbed dose where there is not equilibrium with Kerma is more complicated and requires considering the collisional stopping power of electrons. It is typical to use ionization chambers to measure the charge liberated by radiation beams under reference conditions. The absorbed dose-to-water for low LET radiation sources can then be determined using

$$D_{water} = \frac{Q}{m}\left(33.97\frac{J}{C}\right)\overline{S}_{air}^{water} \tag{2.9}$$

where Q is the charge of ions produced in a volume with mass, m, and $\overline{S}_{air}^{water}$ is the ratio of electron collisional stopping powers in water and air for the range of electron energies present in the beam. Additional correction factors are necessary to correct for the spectrum of electron energies and the geometry of the detector, as well as ambient temperature and pressure.

2.3.2 Radiation detectors

While accurate determination of absorbed dose using the formalism described in the section 2.3.1 is one aspect of dosimetry, there are several other attributes that should be considered as well. These include: spatial resolution, temporal resolution, dose independence (or the ability to measure a wide range of doses), and dose-rate independence. Application to UHDR radiotherapy has widened the necessary operating ranges of dosimeters for each of these parameters. UHDR sources are often small fields (on the order of mm in size) and doses are delivered in sub-second treatment times, necessitating both high spatial and temporal resolution. Another important attribute is the *tissue equivalence* (or water equivalence) of a dosimeter. Though the response of the dosimeters discussed in this section are generally

agnostic of the energy of the incident radiation beam, they may over or underestimate dose-to-water under certain conditions, making them poor surrogates for determining dose to a patient.

2.3.3 Ionization chambers

Ionization chambers operate by detecting liberated electron charge when ionizing radiation creates ions within a gas-filled chamber. A voltage is applied between the shell of the chamber and anode which protrudes into the chamber as shown in Figure 2.13. The liberated electrons are collected at the anode, and measured using an electrometer. The resulting charge is then used to determine the absorbed dose at the point of measurement, using versions of the formalism described in equation 2.9. The clinical linear accelerators used for 6-20 MeV electron experiments in this work were calibrated using the AAPM TG-51 protocol [61]. For dose measurements of the UHDR x-ray tube source the AAPM TG-61 in-air method was used [62]. Ionization chambers can be fabricated using a variety of designs, including cylindrical [63], parallel plate [64], and free air chambers [65], each suited for different applications. The specific formalism used to determine absorbed dose is governed by the quality of the radiation beam and the design of the ionization chamber.

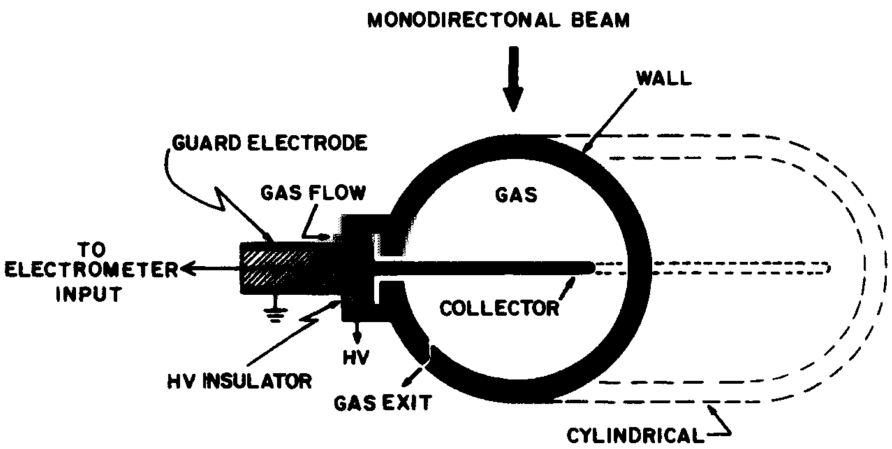

Figure 2.13: Design of a spherical/cylindrical gas-filled ionization chamber. Adapted from Attix [26].

Ionization chambers have limited spatial resolution on the order of several mm. They are typically implemented in an absolute or reference dosimetry capacity where large sensitive volumes reduce measurement noise. The temporal resolution of ionization chambers is limited by the readout speed of the corresponding electrometer, typically 0.5 seconds. They can provide online dosimetry for linacs operating at CDR though they suffer from decreased ion collection efficiency at UHDR [66]. This is the principal issue in using ionization chambers

for dosimetry in a UHDR-RT context. For beam time structures with greater than 10 Gy per pulse, the ion collection efficiency degrades and requires laborious corrections [67].

2.3.4 Radiochromic film

Radiochromic films are planar dosimeters that become darker in response to ionizing radiation. Their design consists of a thin radio-sensitive layer sandwiched between two protective polyester sheets. Radiochromic films undergo a self-developing process through a polymerization reaction induced by radiation exposure, leading to darkening of the film proportional to the absorbed dose. The pixel value or optical density of the film is then measured and converted to absorbed dose. Films offer advantages over ionization chambers due to their high spatial resolution, and tissue equivalence across a wide range of energies relevant to radiotherapy [68, 69]. They are commonly used for determination of two-dimensional dose distributions in a radiation therapy context [70].

The calibration process for films involves generating calibration curves to correlate the darkening of the film with known absorbed dose values. This calibration is typically done by exposing the films to doses using a linear accelerator. They are commonly cross-calibrated against an ionization chamber under the same irradiation conditions. After exposure, the films are scanned using a flatbed scanner to measure the optical density of the darkened areas. The optical density is then converted to absorbed dose through the calibration curve, which establishes the relationship between radiation dose and pixel value as shown in Figure 2.14.

Image processing is an essential part of film dosimetry. Regions of interest (ROIs) are defined on the scanned image where the response of the film is quantified. The mean pixel value within these ROIs are measured to establish the color-channel dependent relationship between the known radiation doses D and pixel values according to

$$D = \frac{(ax_c + b)}{(x_c + c)} \tag{2.10}$$

where x_c is the red, green, or blue pixel value, and a, b, and c are fit parameters [71]. The calibration curves of this form can then be used to transform pixel value images into dose maps for additional analysis. For all the film dosimetry in this thesis, either the green or red channel was used alone. As can be seen in the calibration curves in Figure 2.14, noise in the blue channel pixel value would result in large uncertainties in dose measurements. Typically, background (0 Gy) dose points are included on the calibration curve. In experimental conditions, measured dose from un-irradiated background films are subtracted from the dose maps of irradiated films. While software tools like FilmQA Pro (Ashland Advanced

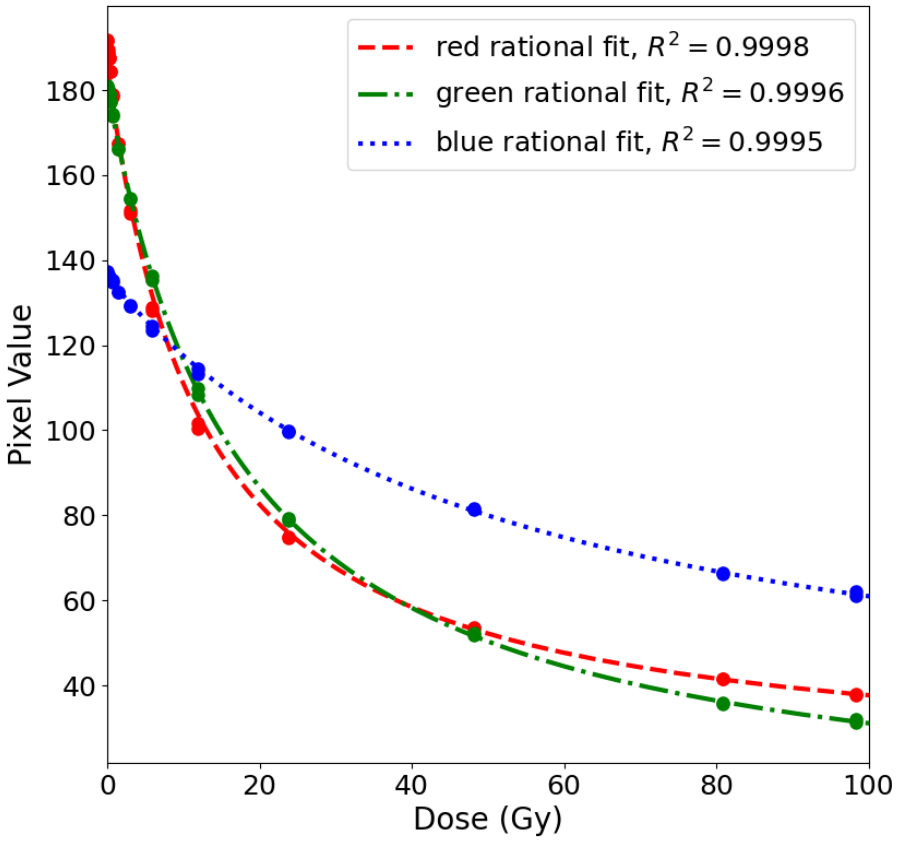

Figure 2.14: Example calibration curve for EBT-XD film. Independent calibration curves are generated for the red, green, and blue channels using a rational fit.

Materials, Bridgewater, NJ) and ImageJ (National Institutes of Health) are commonly used for this analysis [72], the film dosimetry presented in this thesis was conducted using codes created in Python 3.10.

Films offer the highest spatial resolution of any dosimeter, with specifications as low as 25 μm [73]. This allows for detailed two-dimensional dose distribution measurements, which is an asset for UHDR-RT with small fields. In contrast to the other dosimeters discussed in this thesis, films do not provide any temporal information. Films instead give the integrated dose over the duration of the dose delivery. The response of films does not depend on dose rate, demonstrating linear response with dose when exposed to high dose-per-pulse beams at least up to 8×10^{11} Gy/s [11]. Films have also been shown to be accurate over a wide range of doses. For example, Gafchromic™ EBT-XD (Ashland Advanced Materials) has demonstrated accuracy within 1% over the range 0.4-40 Gy [74]. New readout techniques continue to be developed which extend their usable range even further [75]. Films show energy dependence, especially at low x-ray energies [76] and with high LET radiation sources [77], which can impact the accuracy of dose measurements.

2.3.5 Plastic scintillation detectors

Radioluminescence is a phenomenon where materials emit optical light after absorbing energy from ionizing radiation. Electrons within the material are excited downstream of the basic photon and electron interactions with matter described earlier in this chapter. As excited molecules subsequently relax to their ground states, they emit fluorescence and phosphorescence light, which both fall under the umbrella of *scintillation*. The intensity of the light produced by the radioluminescent material, or *scintillator*, is directly proportional to the energy absorbed, and is independent of the initial energy of the incident particle [78]. This light can therefore be detected and used to determine the absorbed dose in the active scintillator volume, and subsequently be used as a surrogate for absorbed dose-to-water. Cherenkov light produced by charged particles is also related to absorbed dose but unlike scintillation light is emitted anisotropically. This complicates dosimetry based primarily on Cherenkov detection [79, 80], and generally renders it a contaminant in scintillation dosimetry [15].

History of scintillators

In 1903, British physicist and radio chemist Sir William Crookes accidentally created the first scintillation detector when he spilled radium bromide onto a surface of zinc sulfide. As he carefully recovered the expensive alpha-emitter with the aid of a magnifying glass he noticed discrete flashes of light arranged in a 'turbulent luminous sea' as the alpha particles struck the zinc sulfide, a scintillating material [81]. Crookes refined his crude optical dosimetry method into a device called the *spinthariscope* which was capable of counting individual radioactive decay events.

In the century that followed, many scintillating materials were developed for applications in medicine. These materials broadly belong to two camps: inorganic, and organic (or plastic) scintillators. Inorganic scintillators, typically composed of high-Z elements, attenuate x-rays more efficiently than plastics and have found uses in medical imaging [39]. These include CsI for x-ray computed tomography (CT) [82], LSO for positron emission tomography (PET) [83], and CWO for onboard MV imaging with a linac [84]. These applications benefit from a material with a high cross-section, capable of maximizing signal-to-noise ratios with low count rates. Plastic scintillating materials however, have found more traction in high fluence environments, including radiotherapy [85] and high energy physics experiments [86]. Organic scintillators can be made from crystalline materials like anthracene and stilbene, liquids including benzene, and polymers such as polyvinyltoulene and polystyrene [87], which will be discussed extensively throughout this thesis.

The first study of PSDs for dosimetry of radiotherapy beams was conducted by Murai

et al. in 1964 who irradiated a $28 \times 28 \times 15$ cm cubic plastic scintillator [88]. They were able to determine the dose delivered to the volume by integrating the photoelectric current measured by a photomultiplier tube (PMT). In 1992, Beddar *et al.* published a pair of articles on PSDs for use in radiotherapy which are considered the foundational works in this field [15, 16]. There has also been interest in the development of two dimensional PSDs composed of scintillating sheets [89] and fibers [90]. In the realm of high energy physics, PSDs have been used for experiments on the proton synchrotron [91] and the large hadron collider [92] at CERN.

Physical properties of Scintillators

PSDs are a subset of radioluminescent detectors that use plastic-based scintillating materials to detect ionizing radiation. Early PSDs, such as the one described by Figure 2.15, used a scintillator as well as a clear fiber (for detecting Cherenkov) each coupled to a separate photomultiplier tube (PMT) via a transparent light guide [15]. Most contemporary PSD systems use solid state photodetetors including photodiodes and charge-coupled devices (CCDs) which do not require a stable high-voltage power supply and allow for multiple PSDs to be connected to a single readout device [93, 94].

One advantage of PSDs is their ability to deliver high spatial resolution. Advances in the manufacturing of scintillating materials have made it possible to fabricate probes with limiting dimensions down to 10 μm [17], though active scintillator dimensions of 0.1 to 1 mm are more common [95, 96]. This high spatial resolution allows PSDs to overcome the volume averaging effect associated with most ionization chambers, and yields better agreement with films as shown in Figure 2.16. This may be particularly important in the application to UHDR dosimetry which is often associated with steep dose gradients, especially at experimental facilities with small beam sizes.

While PSDs are capable of nearing the high spatial resolution and dose/dose-rate independence of film, they stand alone in their ability to provide high temporal resolution. The response time of the scintillating material to ionizing radiation is on the order of nanoseconds (depending on the composition) and is limited by the speed of the electronic readout. State-of-the-art CCD systems are capable of temporal resolutions of 2.5 ms [97]. The tissue equivalence of scintillation detectors depends on the composition of the scintillating material.

The active element of PSDs are composed of a bulk medium coupled to an aromatic hydrocarbon and often, additional organic fluors to facilitate wavelength shifting [98]. The PSDs used throughout this thesis utilize polyvinyltoulene plastic scintillators, or polystyrene scintillating fibers as the active radioluminescent element. Scintillating fibers are differentiated from plastic scintillators by polymethylmethacrylate (PMMA) cladding surrounding

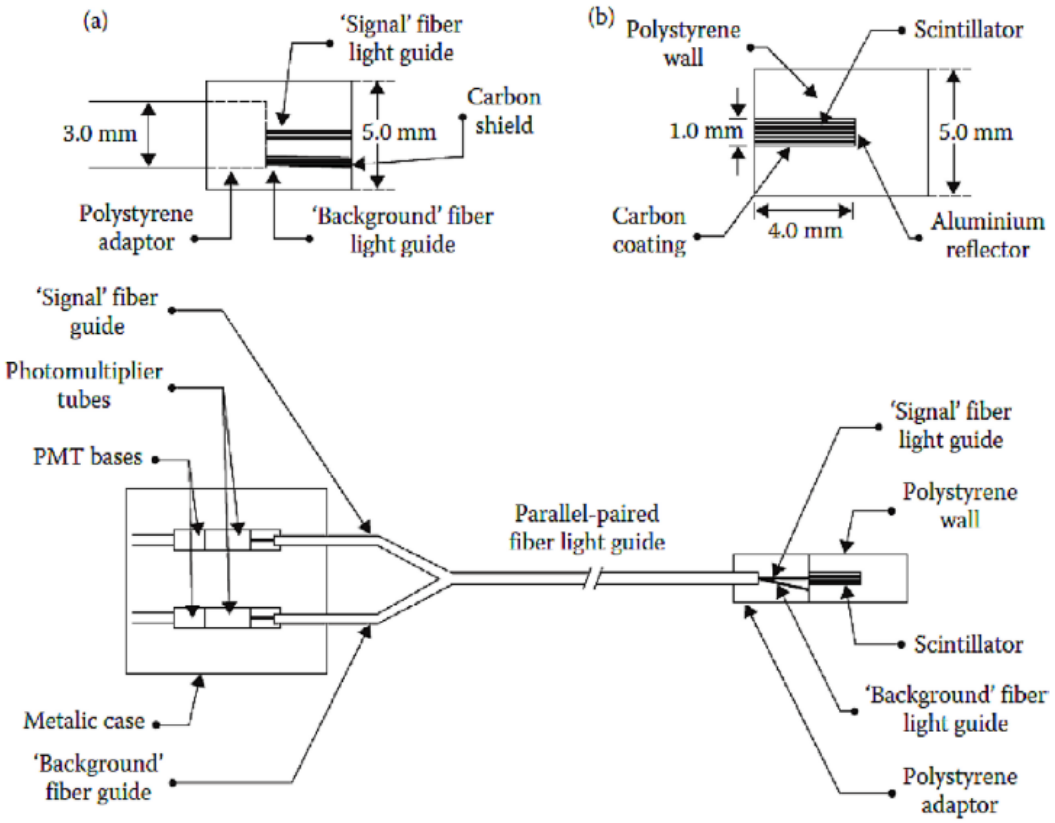

Figure 2.15: Schematic of the PSD design used by Beddar *et al.* in the first dosimetric characterization of PSDs [15]. The Cherenkov signal is detected by a clear fiber connected to a separate PMT in order to correct the PSD signal.

the fiber [99], which aids in total internal reflection and transport of scintillation light into the optical fiber as shown in Figure 2.18.

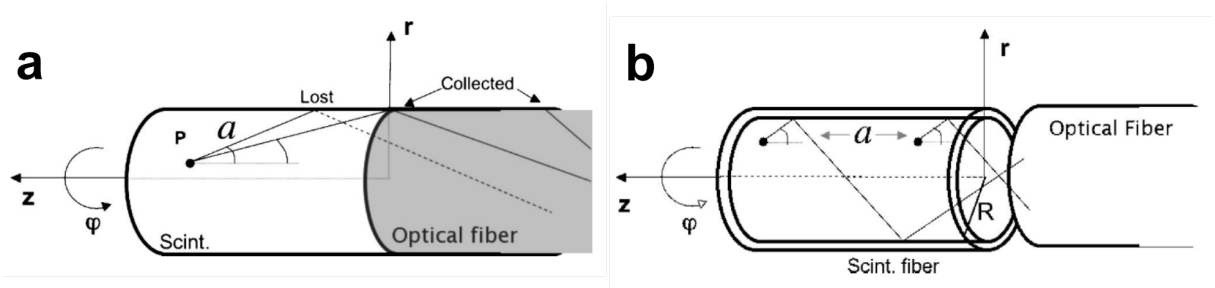

Figure 2.17: Schematics of PSDs fabricated from plastic scintillators (a), and scintillating fibers (b). The PMMA cladding on the scintillating fiber increases the efficiency of transmitting light to the optical fiber. Adapted from Archambault *et al.* [100].

Scintillation photons, which are produced isotropically within the scintillator volume, can only be transmitted to the optical fiber if they are incident to the optical fiber at an

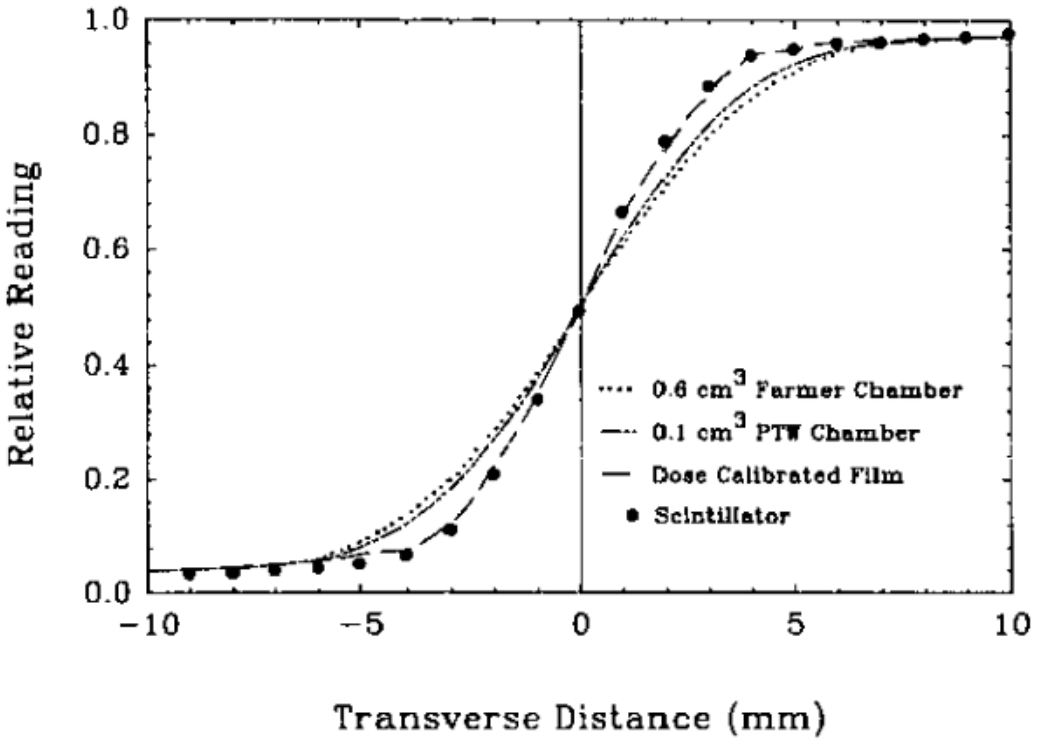

Figure 2.16: Profiles of a half-blocked ^{60}Co beam were measured by Beddar *et al.* with a 1 mm diameter PSD as well as film and two common ionization chamber types [16]. The PSD signal shows excellent agreement with film.

acceptance angle less than α, determined by

$$\alpha = sin^{-1}\left(\frac{1}{n_{sci}}\sqrt{n_{co}^2 - n_{cl}^2}\right) \tag{2.11}$$

where n_{sci}, n_{co}, and n_{cl} are the refractive indices of the scintillating fiber, optical fiber, and cladding, respectively [100]. Scintillation fibers increase the acceptance angle compared to plastic scintillators by surrounding the scintillating volume with a material of lower refractive index. Scintillating fibers also mitigate the optical effects of physical damage and do not require perfectly polished surfaces.

In response to ionizing radiation plastic scintillating materials produce 7,000 to 10,000 photons per MeV absorbed, corresponding to an efficiency of ∼2.5% [85]. As stated previously, the light yield efficiency of a scintillator is generally independent of the energy of the incident radiation beam. However, when exposed to high LET radiation beams, PSDs can experience a kind of temporary radiation damage or saturation of their scintillation efficiency called *ionization quenching* [101]. This becomes relevant for protons and heavy ions near the Bragg peak [98] as well as photo-electrons with energies below ∼125 keV [102]. Birk developed an empirical formula to describe the effect of stopping power on the scintillation

efficiency, given by

$$dL/dx = \frac{A \times dE/dx}{1 + kB \times dE/dx} \tag{2.12}$$

where dL/dx is the is the light output per path length of the incident particle, dE/dx is the depth dependent stopping power, A is the *un-quenched* scintillation efficiency, and kB is the Birk quenching constant [78]. For low LET radiation, $dL/dx \approx A \times dE/dx$, and for high LET radiation it becomes $dL/dx \approx A/kB$. Using Birk's formula Wang *et al.* experimentally determined the depth dependent quenching correction factors for PSDs used to measure 73 to 230 MeV proton beams [103].

Stem corrections

PSD signals can become contaminated with Cherenkov produced within the scintillator and optical fiber as well as fluorescence from within the optical fiber. These contaminant signals are referred to as *stem effects* and in many cases must be corrected for to provide accurate determinations of dose. The first technique, proposed by Beddar *et al.* was to simply subtract the isolated Cherenkov and fluorescence signal using a two fiber system [16]. Single fiber approaches were subsequently developed which exploit differences in the spectra of the different radioluminescence types. While the spectra of Cherenkov and fluorescence signals overlap with the desired scintillation signal, differences in their peak wavelength and intensity can be used to remove them. Cherenkov light peaks in the blue-violet range, which de Boer *et al.* exploited by using plastic scintillators with high concentrations of wavelength-shifting fluors. The resulting green and orange light emitted by the PSDs could more easily be distinguished from the undesired Cherenkov light [104].

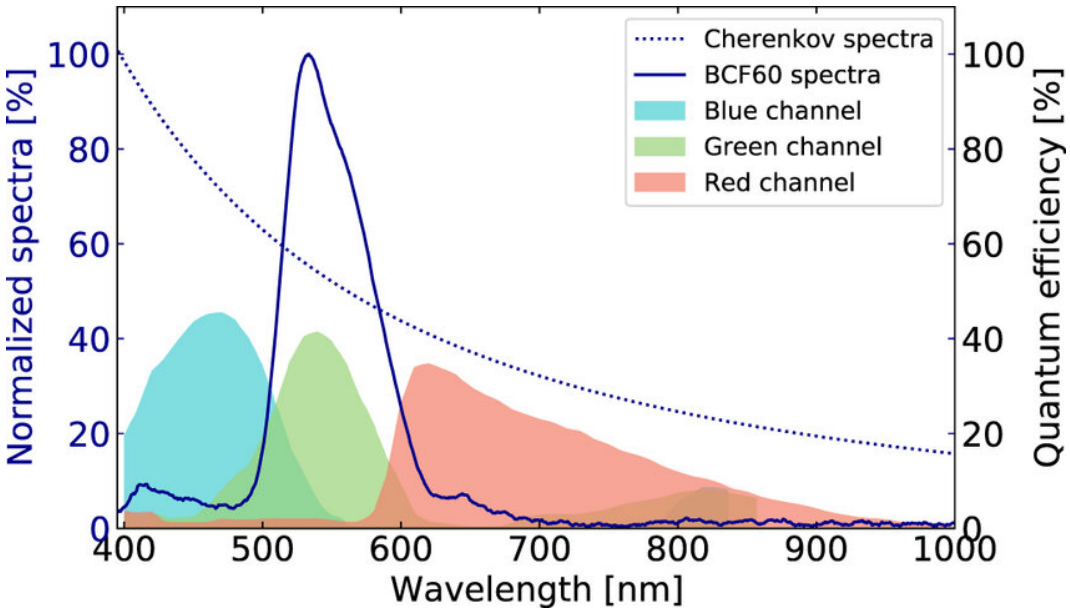

Figure 2.18: Measured spectra of BCF-60 (Luxium Solutions, Hiram, OH), a commonly used PSD. The total signal is shown along with the isolated Cherenkov contribution and the resulting spectra from three filters that can be used to discriminate and subtract stem effects. Adapted from Cloutier *et al.* [31].

Modern stem correction methods take advantage of the ability to measure the optical spectrum using CCDs [105]. Multispectral [106] and hyper spectral approaches [107] are able to discriminate the scintillation spectra from contaminants and increase the accuracy of PSDs for small-field dosimetry [108]. To apply these spectral removal techniques, the energy and angular dependence of the contamination signals can also be exploited. Cherenkov light has an energy threshold of $\sim$ 180 keV in plastics [109], while fluorescence does not have an energy threshold. Additionally, the Cherenkov signal reaches a maximum intensity at $\sim$41° to the incident radiation beam. This allows for the signals to be isolated by measuring the spectral output at the beam angles corresponding to the minimum and maximum Cherenkov signal. The stem effect contribution of fluorescence is also mitigated by using PMMA optical fibers which have a lower fluorescent yield than silica, which was used previously [110].

2.3.6 Comparison of dosimeters

A comparison of the detector types discussed in this section is shown in Table 2.2. Due to their high spatial and temporal resolution, as well as their potential dose-rate independence, scintillation detectors (including PSDs) offer clear advantages over ionization chambers and radiochromic films. The work presented in this thesis will also explore the tissue equivalence of PSDs of various compositions.

Table 2.2: Summary of attributes relevant to UHDR-RT for common dosimeter types. *Temporal resolution of PSDs depends on the readout device and can be much faster, 2.5 ms was the limiting resolution for the platform used in this thesis. Adapted from Romano *et al.* [111].

Detector	Spatial Resolution	Temporal Resolution	Dose-rate Independence
Ionization Chamber	Poor (>2 mm)	Good (∼0.5 s)	Poor ($\leq 10^2$ Gy/s)
Radiochromic Film	Excellent (<0.1 mm)	None	Excellent ($\geq 8 \times 10^{11}$ Gy/s
Scintillator Detector	Good (<0.5 mm)	Good (<2.5 ms*)	Excellent ($\geq 10^9$ Gy/s)

Chapter 3

Radiobiology of Ultrahigh Dose-Rate Radiotherapy

The biological mechanisms behind UHDR radiotherapy and the FLASH effect are still under active investigation, with hypotheses focusing on oxygen depletion [112, 113], immune-mediated responses [114, 115], and DNA damage [116, 117]. Studies have utilized various model organisms such as mice [33], mini-pigs and cats [13], zebrafish embryos [118], and cell cultures [119] to explore the effects of FLASH radiotherapy on different tissues and tumour types. These studies have highlighted the potential of FLASH radiotherapy to maintain tumour control while sparing normal tissues, paving the way for further preclinical investigations and clinical trials to establish its safety and efficacy in human patients.

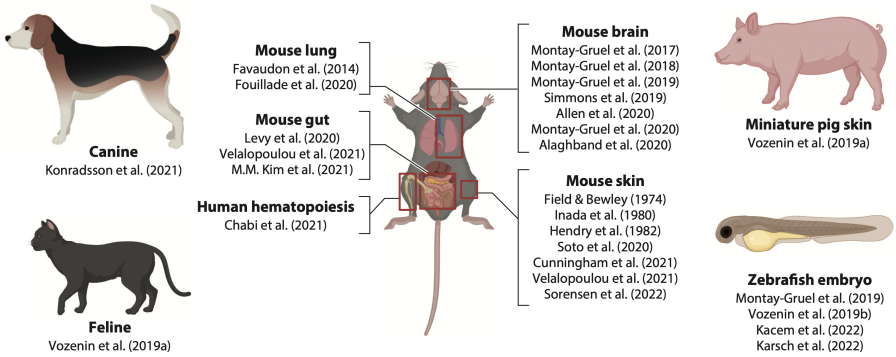

Figure 3.1: Radiobiological models frequently used for assessing the effects of UHDR-RT on normal tissues. Adapted from Limoli [120].

This chapter will give a primer on the historical background of UHDR radiotherapy and the current understanding of the radiobiological FLASH effect, including possible mechanisms. *Drosophila melangoaster* will be introduced as a model organism for studying cancer therapies and as a potential candidate for FLASH experiments.

3.1 History of FLASH Radiobiology

The first published observation of a sparing effect from UHDR irradiation was an experiment performed by Dewey and Boag in 1959 [121]. The bacterium *Serratia marcescens* were irradiated with x-rays and electrons produced by a 1.5 MV linear accelerator in the presence of different oxygen conditions. They noticed that delivering doses of 10 - 20 krads with electrons in single 2 microsecond pulses (dose rates of $5 - 10 \times 10^7$ Gy/s) in normal oxygen conditions resulted in survival fractions consistent with conventional dose rate irradiations (0.1 Gy/s) in anoxic conditions. Under the anoxic conditions (100% nitrogen) the UHDR and CDR treatments had similar clonogenic survival. Contrary to the results of Dewey and Boag and the current heterodox understanding of FLASH, in 1966 Hornsey and Alper found that the lethal dose for mice *decreased* with increasing dose-rate [122]. In the 1970's, additional mouse studies showed normal tissue sparing under UHDR conditions [123, 124]. Early *in vitro* studies of HeLa cells and Chinese hamster cells also showed reduced damage from UHDR sources [125, 126].

3.1.1 Pre-clinical FLASH

The field of FLASH radiotherapy lay largely dormant until 2014, when a group based at CHUV in Lausanne investigated the potential for reducing normal tissue toxicities in mice while maintaining tumour control after UHDR electron treatments [12]. Favaudon *et al.* observed a differential effect where lung fibrosis was reduced with UHDR irradiation compared to CDR (0.03 Gy/s) while also effectively repressing the growth of lung tumours. This seminal paper also established a speed limit of sorts for CDR-RT, stating that dose rates in excess of 40 Gy/s could be considered capable of inducing the FLASH effect. While this work has come under scrutiny and generated controversy [127], it has served as the nexus for a new sub-field of research within radiotherapy.

In the following years the ability to reduce normal tissue toxicities in a variety of normal tissue types using UHDR beams was confirmed. Early studies continued to focus on mice, including the ability to reduce side effects of brain irradiation with electrons [33] and x-rays produced by a synchrotron [128]. Skin sparing effects were then demonstrated in mini-pigs and in cat patients while effectively controlling tumours [13]. However, a clinical trial of cat cancer patients was terminated early due to the development of severe late toxicities (bone necroses) in the UHDR-RT arm which was not observed with cats treated with CDR-RT [129]. A sample of the studies focusing on the response of tumour and normal tissues to UHDR and CDR-RT is presented in Tables 3.1 and 3.2.

One way to quantify the magnitude of the FLASH effect is with a normal tissue *dose*

modifying factor, defined as:

$$DMF = \frac{D_{UHDR}}{D_{CDR}} \tag{3.1}$$

where D_{UHDR} and D_{CDR} are the doses required to reach the same level of normal tissue toxicity. The reciprocal of the DMF, the *FLASH Factor*, is also sometimes used [130]. UHDR has been shown to cause a FLASH effect across a diverse set of species and normal tissue types with DMF values between 1.3 and 1.8 [131].

Most pre-clinical studies of UHDR-RT have utilized a single delivery of the full prescription dose, rather than a fractionated delivery as is common practice with CDR-RT [132]. There is however, conflicting evidence on the impact of fractionation on the magnitude of the FLASH effect. Montay-Gruel *et al.* found that the neurocognitive sparing effects and efficacy of slowing glioblastoma growth with 6 MeV electron UHDR-RT were conserved when the dose was split into three fractions [38]. Sorensen *et al.* measured skin toxicitiy after UHDR-RT with protons and found that splitting the dose across multiple fractions reduced the normal tissue sparing effect [133]. When three fractions were used, UHDR-RT had equivalent toxicity to CDR-RT.

3.1.2 Early Clinical Translation of FLASH

Given the ability of UHDR beams to demonstrate sparing effects of similar magnitudes across several mammalian models within a few years of the 'rediscovery' of FLASH, clinicians felt comfortable moving towards clinical translation. The first patient to be prescribed UHDR-RT was treated in Lausanne in 2019 [32]. A 75 year old man with multiresistant CD30+ T-cell cutaneous lymphoma was given 15 Gy in 90 ms (∼167 Gy/s mean dose rate) to a 3.5 cm diameter tumour. This treatment resulted in control of the tumour, measured at 5 months follow-up, and demonstrated the safety of implementing UHDR-RT for skin lesions. The first clinical trial for UHDR-RT, began enrolment in November 2020 [134]. FAST-01, which was sponsored by the radiation device vendor Varian, included 10 patients and was designed to test the feasibility, and efficacy of UHDR protons to treat painful bone metastases. This non-randomized trial showed consistent clinical results with conventional radiotherapy [19]. The path to clinical translation has continued for protons with the FAST-02 trial [20]. Additional clinical trials with electrons for treatment of skin lesions are also underway with a Phase II randomized trial [21].

Table 3.1: Selection of UHDR irradiations of tumour models. Adapted from Gao *et al.* [135].

Model	Total dose (Gy)	UHDR dose rate (Gy/s)	Radiation source type	Outcome	Reference
NMRI mice with FaDu cells	17.4 and 19.7	$\geq 10^9$ (Pulse mode)	SNAKE (proton)	isoefficacy	Zlobinskaya [136]
C57BI/6J mice with	18	40	(proton)	UHDR improved efficacy	Rama [137]
Cat, T2/T3N0M0 squamous-cell-carcinoma	25–41	130–190	Kinetron/Oriatron 6e (electron)	isoefficacy	Vozenin [13]
Human, CD30+ T-cell cutaneous lymphoma	15	167	Oriatron eRT6 (electron)	isoefficacy, tissue sparing	Bourhis [32]
Mice, pancreatic cancer flank tumors	15/12–18	78	IBA Proteus Plus (proton)	isoefficacy	Diffenderfer [138]
Mice, total abdominal irradiation	16	216	N/A (electron)	isoefficacy	Levy [139]
Mice, with head and neck cancer	15	115	Varian Probeam (proton)	isoefficacy	Cunningham [140]
Mice injected with glioblastoma cells	25	2.5×10^3 to 7.8×10^6	Oriatron eRT6 (electron)	isoefficacy	Montay-Gruel [38]
Mice. Total body irradiation	4	200	OriatroneRT6 (electron)	isoefficacy	Chabi [141]

Table 3.2: Selection of UHDR irradiations of normal tissues. Adapted from Gao *et al.* [135].

Model	Total dose (Gy)	UHDR dose rate (Gy/s)	Radiation source type	Normal tissue sparing	Reference
Mice	10	>100	Oriatron 6e (electron)	Yes	Montay-Gruel [33]
Mice	10–22	210	N/A (electron)	Yes	Loo [142]
Mice	10	37	ESRF (X-ray)	Yes	Montay-Gruel [128]
Mice	30	200–300	Varian 21EX (electron)	Yes	Simmons [143]
Mice	15/17.5/20	40	N/A (proton)	Yes	Abel [144]
Mice	16	37	Varian 2100 IX (electron)	No	Venkatesulu [145]
Mice	13–22	120	IBA C230, (proton)	Yes	Zhang [146]
Mice	8	4.4×10^6	Oriatron eRT6 (electron)	Yes	Alaghband [147]
Mice	5.2/4	>20	N/A (electron)	Yes	Fouillade [148]
Mice	16	216	N/A (electron)	Yes	Levy [139]
Mice	12–18	78	IBA Proteus Plus (proton)	Yes	Diffenderfer [138]
Mice	35	57	Varian Probeam (proton)	Yes	Cunningham [140]
Mice	4	200	Oriatron eRT6 (electron)	Yes	Chabi [141]
Mice	30/45	69–124	IBA Proteus Plus (proton)	Yes	Velalopoulou [149]
Mice	7.5–12.5	>280	6-MeV electron linear accelerator	Yes	Ruan [150]
Mice	12.7–587	44.4	IMBL (X-ray)	No	Smyth [151]
Mice/zebrafish	10/14	37	ESRF (X-ray)	Yes	Montay-Gruel [152]
Zebrafish embryos	0–45	100	UPTD (proton)	No	Beyreuther [153]
Zebrafish embryos	26	105 (mean)	ELBE (electron)	Yes	Pawelke [154]
Pig skin	22–34	300	Kinetron (electron)/Oriatron 6e (electron)	Yes	Vozenin [13]
Human lung fibroblasts	20/10	100/1000	RARAF (proton)	Yes	Buonanno [155]

3.2 Potential mechanisms of FLASH

After the immediate physical effects of ionizing radiation occur, a cascade of chemical and biological processes are set into motion, including the formation of reactive oxygen species (ROS), and cellular pathways to repair damage. The timescale of these processes is described in Figure 3.2. UHDR-RT, which is characterized by mean dose-rates greater than 40 Gy/s, generally results in sub-second treatments. Conventional treatments however, at dose-rates of ≤ 0.1 Gy/s, take on the order of minutes [156]. The FLASH effect therefore interacts with a different set of processes downstream from the physical effects generated by UHDR-RT than conventional RT. This section will explore a few possibilities for how these processes may be disrupted in a way that leads to the FLASH effect.

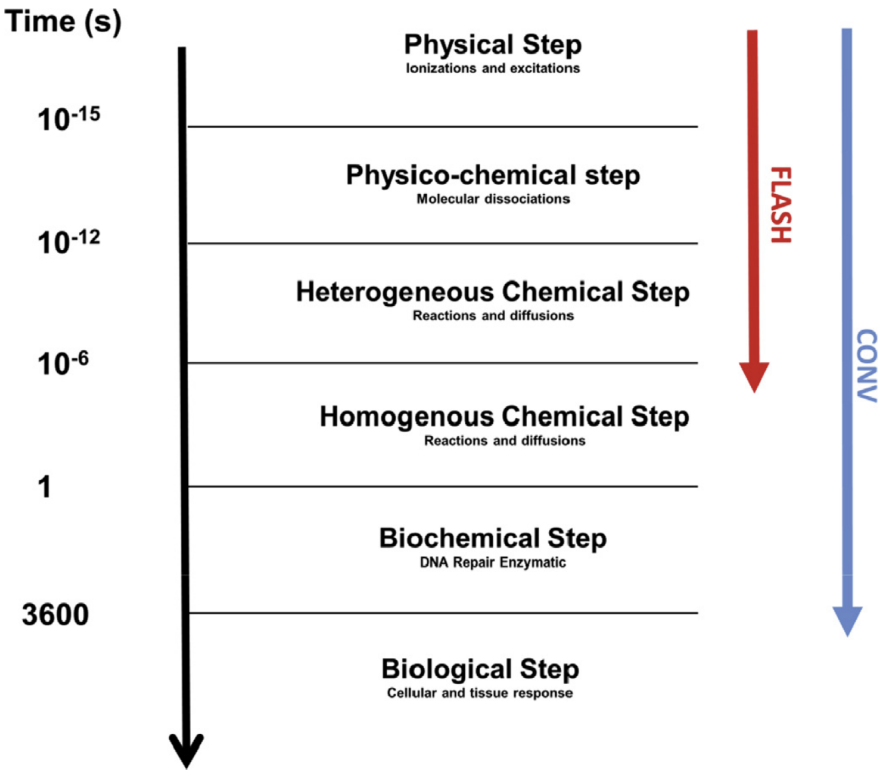

Figure 3.2: Timeline of the physical, chemical, and biological processes involved in the response to ionizing radiation. Adapted from Vozenin [157]

3.2.1 Oxygen

The role of oxygen in triggering the FLASH effect has gained attention from the first studies of UHDR irradiations, with Dewey and Boag speculating that rapid depletion of local oxygen after a single large radiation pulse could confer radio-resistance [121]. Dewey and Boag

confirmed this a decade later [158]. This idea was expanded on by Ling *et al.* in 1978 when they irradiated mamallian cells with UHDR and estimated the time-scale of oxygen mediated radiosensitivity to be on the order of 3×10^{-3} s [159].

To understand why oxygen has been such a popular explanation for driving the mechanism underlying the FLASH effect we need to examine the role that oxygen typically plays in radiotherapy. The *oxygen effect* refers to the enhancement of the therapeutic or detrimental effects of ionizing radiation due to the presence of oxygen. The radiolysis of water produces free radicals, including solvated electrons and hydrogen radicals (e^-_{aq} and $^{\cdot}H$), that can cause DNA damage. In an oxygenated environment, these radicals also create superoxide and hydroperoxyl ($O_2^{\cdot -}$ and $HO_2^{\cdot}$) which make the DNA damage harder to repair (referred to as *fixed damage*) [160, 161]. Conversely, in the absence of oxygen (hypoxic conditions), cells become more resistant to radiation-induced damage. To quantify this effect, radiobiologists use the oxygen enhancement ratio (OER), which is defined as

$$OER = \frac{D_{p_1}}{D_{p_2}} \tag{3.2}$$

where D_{p_1} and D_{p_2} are the required doses to reach the same biological effect under hypoxic (p_1) and normoxic conditions (p_2). Typically, the OER for low-LET radiation (e.g. x-rays, and electrons) ranges from 2.5 to 3.5 at high dose levels [160]. The OER decreases as the linear energy transfer (LET) of the radiation increases, with high-LET radiation (e.g. alpha particles, neutrons) having an OER close to 1. The OER can also depend on factors such as the tissue type, oxygen partial pressure, and the chosen biological endpoint. Tumour tissues are typically hypoxic due to poor vasculature, which can confer radio-resistance, making them difficult to treat effectively. The differential OER between well-oxygenated normal tissues surrounding hypoxic tumours can result in increased side effects when delivering tumour controlling doses. A potential mechanism for FLASH is therefore the induction of temporary hypoxia in normal tissues, effectively pushing the OER towards unity.

In order to determine whether FLASH could be harnessing the power of the oxygen effect, we must consider the timescale of oxygen depletion relative to the time structure of UHDR and conventional dose rate beams. Based on the work by Ling *et al.* it is estimated that cells in a monolayer are able to restore normal intracellular oxygen concentrations in $\sim 10^{-2}$ s [113, 159]. The rate of oxygen diffusion and cellular metabolism is also dependent on the cell type (including cell diameter), and availability of ambient oxygen. Studies of the mechanistic role of oxygen in causing the FLASH effect have focused on *in silico* [162], and *in vitro* tests [163], where the oxygen kinetics can be well understood. The results of these studies have diverged, with several concluding that oxygen could only have a marginal

role in the FLASH effect [164] or that it could only cause tissue sparing in already hypoxic tissues [113]. Montay-Gruel *et al.* tested the impact of oxygen concentration *in vivo* by allowing anesthetized mice to breath carbogen during irradiation. They found that oxygen concentrations greater than normoxic conditions reversed the cognitive sparing effects of UHDR-RT [152].

3.2.2 Immune Response

Reduced Damage to Circulating Immune Cells

Another possible explanation for the FLASH effect is that by reducing the total treatment time with UHDR-RT, a decreased volume of circulating blood is irradiated. This circulating blood contains immune cells which play a role in protecting normal tissues post irradiation. Jin *et al.* performed a computational study which concluded that immune cell killing could be reduced to ∼80 % using UHDR-RT [114]. This study suggested that the dose-rate threshold for FLASH would be dependent on total volume irradiated. Galts and Hammi later showed that UHDR-RT with pencil-beam scanning protons could be used to spare circulating lymphocytes for brain patients [115].

Modulation of the Tumour Micro-environment

UHDR-RT may also alter the tumour micro-environment in a way that changes the mechanism of tumour control, without necessarily changing the efficacy. Kim *et al.* found that UHDR-RT increased the production of ROS while simulataneously decreasing activation of myosin light chain and γH2AX (which are markers for lethal DNA damage) relative to CDR-RT [119]. They hypothesized that normal tissues would be more efficient at removing ROS through metabolic processes than tumour tissues. Their results also suggested that UHDR-RT allows immune cells to more efficiently infiltrate tumour tissues.

3.2.3 DNA Damage

Incidence of damage

The final potential FLASH mechanism presented here is differences in the induction of DNA single-strand breaks (SSBs) and double-strand breaks (DSBs) compared to CDR-RT. Perstin *et al.* found that UHDR was associated with reduced induction of SSBs and DSBs in plasmid DNA, compared to CDR-RT [116]. They observed greater differential in SSBs which might suggest the FLASH effect may be more effective in reducing non-lethal DNA damage which can lead to late effects, rather than the most acute forms of DNA damage. This reduced

DNA damage from UHDR-RT was confirmed by Fouillade *et al.* with an *in vitro* study of lung cells [148].

Impaired DNA Repair in Tumour Cells

Tumour cells often have defects in DNA repair pathways, such as BRCA1 mutations, which can lead to improper repair of DSBs. The 53BP1 protein, which is crucial for DNA repair, may be deferentially affected by UHDR in normal versus tumour cells. In normal cells, the reduced DNA damage under UHDR-RT may lead to fewer 53BP1 foci and less error-prone DNA repair pathways like non-homologous end joining. In contrast, tumour cells with BRCA1 deficiencies may be unable to properly repair the DNA damage induced by UHDR-RT, leading to more cell death and genomic instability [165].

3.3 Drosophila melanogaster

Drosophila, commonly known as the fruit fly, is a widely used model organism in biology and cancer research. There are at least 1,600 documented species in the diverse genus *Drosophila* [166]. The focus of this thesis will be *Drosophila melanogaster*, which will be referrred to as simply *Drosophila* throughout this chapter. Several advantages of *Drosophila* over the mammalian models prevalent in the FLASH literature discussed previously include: low-cost, short life cycle, genomic characterization, and logistical practicality.

3.3.1 Life Cycle

The life cycle of *Drosophila* is approximately 10 days from egg to emerged adult fly as shown in Figure 3.3. *Drosophila* undergo complete metamorphosis, with distinct embryonic, larval, pupal, and adult stages. The embryonic stage lasts 24 hours, followed by three larval instars (development stage between moulting) over 5 days, a pupal stage of about 6 days, and finally the adult stage which can last 60-100 days [167]. The exact duration of each life stage and overall lifespan is related to environmental stresses including temperature, crowding, and substrate [168]. The transition from larva to pupa involves a dramatic remodeling of tissues, while the pupal stage is a non-feeding, immobile phase of metamorphosis. *Drosophila* can develop spontaneous tumours as they age, making them a useful model for studying cancer progression.

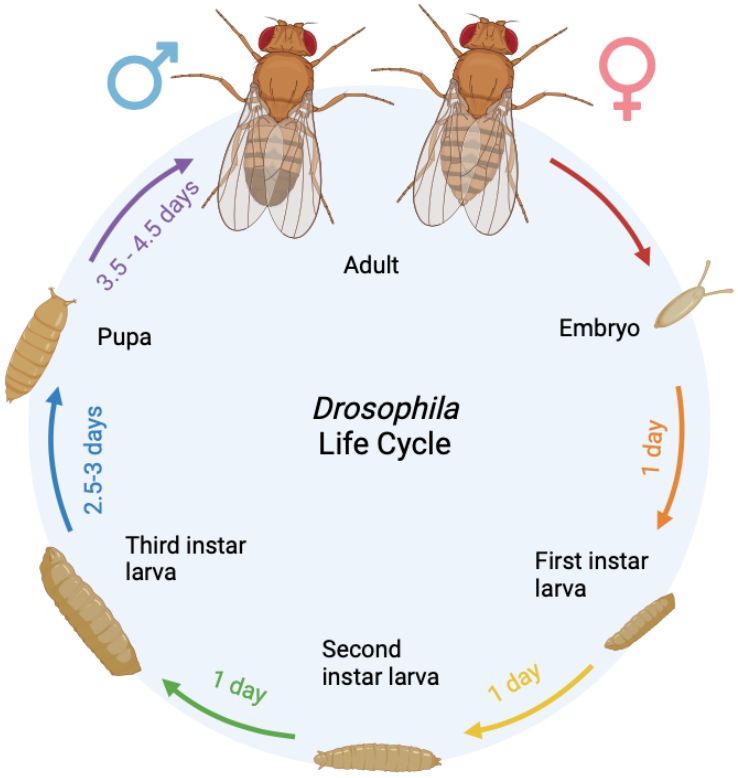

Figure 3.3: Life cycle of *Drosophila* from embryo to adult takes ∼10 days at 25°C.

3.3.2 Anatomy and Development

The *Drosophila* larval body consists of a head, thorax, and abdomen totalling a length of ∼3mm. Larvae develop a well-developed digestive system, respiratory system, and nervous system. These tissues (which have homologs in humans as shown in Figure **??**) can be used to study disease. Also present in the *Drosophila* larva are *imaginal discs*, which are clusters of cells which become functional tissues in the adult flies, including: wings, eyes, legs, and genitals. These imaginal discs are groups of undifferentiated epithelial cells that can be monitored throughout development to study cell fate and even transplanted between flies [169]. The third instar larval stage is the final and largest larval stage, which is typically used to study tumourigenesis [170]. During the third instar, the imaginal disc cells divide rapidly, leading to a ∼1000-fold increase in the size of the discs. The cells present in *Drosophila* imaginal discs show properties similar to mammalian epithelial cells and are amenable to cellular transformation. The rapidly growing imaginal disc tissues, such as the wing disc and eye-antenna disc, are commonly used models to study cancer-related processes in *Drosophila* larvae.

Adult *Drosophila* have a relatively simple body plan consisting of a head, thorax, and

abdomen. The head contains the eyes, antennae, and mouth-parts. The thorax has three pairs of legs and two pairs of wings. The abdomen contains the digestive and reproductive organs. The species name *melanogaster*, or 'black-bellied', refers to the characteristic solid-colored lower abdomen of adult male flies which differentiates them from females. Adult flies reach sexual maturity within a few days of emergence from the pupal case. A single female fly can produce 400-500 offspring, laying about five eggs at a time. *Drosophila* larva and adults are omnivores, surviving on a variety of diets including decomposing fruits and yeasts. They can also exhibit carnivorous and cannabalistic diets, with larva feeding on the carcasses of adult flies [171]. The flies used for experiments included in this thesis were raised primarily on a diet of Carolina instant *Drosophila* medium (a potato starch based diet).

3.3.3 History of fruit fly radiobiology

Drosophila have been central to the study of radiobiology since before the development of the linear accelerators commonly used for radiotherapy in 1953 [172]. Herman Joseph Muller's fruit fly experiments in 1926-1927 led to him receiving the Nobel prize for the discovery of x-ray mutagenesis [173]. Research conducted by Muller's students also contributed directly to the development of the linear-no-threshold (LNT) model for radiation protection, which posits that there is 'no safe dose' of ionizing radiation [174, 175]. This work has faced scrutiny [176] and some have even suggested that there may be benefits to low doses of radiation, a so-called 'hormetic' effect [177].

Dose-rate radio-biology using *Drosophila* models has recently re-gained attention, but the field has been limited to very low dose rates (on the order of CDR or lower). Low dose rate priming doses of 0.2 Gy have been shown to reduce DNA damage and impact gene expression [178]. Other groups have studied the effects of low dose rate background irradiation from cosmic rays by shielding *Drosophila* deep underground. These works have demonstrated a link between dose rate and genetic and phenotypic responses [179, 180]. There is evidence that there may be a radio-adaptive response (RAR) which confers a radio-resistance to tissues pre-irradiated with low dose rate ionizing radiation [178].

3.3.4 *Drosophila* model of cancer

Beyond their important place in the early history of radiobiology, there are good reasons to renew radiobiology experiments with *Drosophila*. One of the strengths of the *Drosophila* model is the well documented genome (i.e. the *Drosophila* Genetic Reference Panel [181]), which contains valuable parallels to human genetics. Most importantly for cancer research, flies have orthologs to humans (genes with common ancestors) for up to 75% of disease

causing genes [182]. Many human cancer genes have orthologs in *Drosophila* that were first discovered and characterized in the fly. For example, the tumor suppressing genes lethal giant larvae (*lgl*) [183] and discs large (*dlg*) [184] were initially identified in *Drosophila* and later found to have human counterparts involved in tumourigenesis.

Two cellular phenomena first discovered in *Drosophila* that have led to important developments in the understanding of human cancer and its treatment include cell competition, and compensatory proliferation. Cell competition, which was discovered in the wing discs of *Drosophila* larvae, is a process in which unusual cells are detected by comparing to surrounding cells within a tissue. Cells which are deemed potentially aberrant or oncogenic are activated to initiate apoptosis (genetically-controlled cellular death) [185]. This has a powerful tumour suppressing capability, which was later found to exist in mammals. Compensatory proliferation was also first observed in the wing discs of *Drosophila* larvae [186]. In this case, irradiated larvae suffered reduction of up to 60% of proliferating cells in their imaginal wing discs and yet were able to form fully functioning wings as adult flies [187]. This introduced the possibility that dying cells are able to communicate with their neighbors and cause them to increase the rate of proliferation to overcome radiation-induced tissue damage.

Due to their diminutive size and low cost *Drosophila* is a model that could provide greater statistics while also offering a genetic model with direct homologs [188, 189]. Models for a number of human cancers have been developed for both larvae and adult flies which can be used to develop new therapies [190]. Additionally, there are significant logistical advantages to working with fruit flies: no research ethics board approval is required, and results with large numbers of flies at various life stages can be generated quickly. Unlike murine models which are typically irradiated one mouse at a time, many larvae or adult flies can be treated simultaneously.

Drosophila can be used to model various aspects of cancer progression, including tumor initiation, growth, invasion, and metastasis. Flies expressing oncogenes like RasV12 or Src64B in specific tissues can develop tumors that recapitulate key hallmarks of human cancers [191]. The *whole-organism* nature of the *Drosophila* model allows for the study of tumor-host interactions and systemic effects like cancer cachexia. The speed, low cost, and genetic tractability of *Drosophila* make it an excellent platform for high-throughput screening to identify new cancer drug targets and test potential therapeutic compounds [192]. *Drosophila* models have been used to validate findings from human cancer studies and uncover novel mechanisms of tumorigenesis [193].

In summary, *Drosophila* is a powerful model organism that has significantly advanced our understanding of the genetic basis of cancer. Its unique advantages, including rapid life cycle, genetic tools, and conservation of cancer-related pathways, make it an invaluable

complement to mammalian models in cancer research.

3.3.5 FLASH experiments with flies

Earlier in this chapter, some of the most influential works on the FLASH effect were highlighted, including studies of mice, mini pigs, cats [33, 13], and the early clinical trials with human patients [19]. Each of these studies is limited by relatively poor statistics. High throughput models, including *Drosophila* are needed in order to reduce statistical noise and deliver clear answers regarding the UHDR parameter space compatible with achieving the FLASH effect.

One possible experimental design is to deliver whole-body irradiations to third instar larvae with different dose rates spanning CDR and UHDR. The progression of the flies can then be tracked through pupae and to adulthood as shown in Figure 3.4.

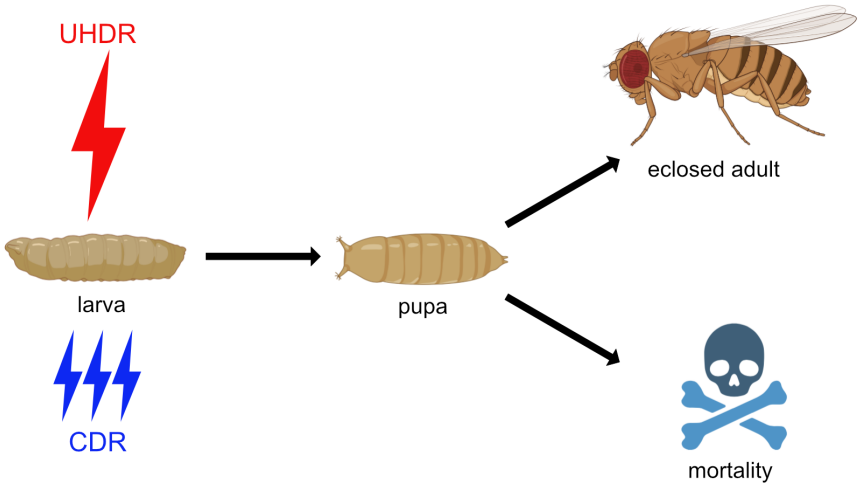

Figure 3.4: Third instar larvae can be irradiated with either UHDR or CDR to the same doses and tracked through pupae and adulthood to score eclosion.

Beyond a certain dose threshold, some subset of irradiated flies will fail to fully develop and emerge (or eclose) from the pupal case. *Eclosion*, which is a surrogate for survival, can be calculated according to:

$$eclosion = \frac{n_{adults}}{n_{pupae}} \tag{3.3}$$

where n_{adults} is the number of live adult flies that fully eclose, and n_{pupae} is the number of larvae that reaches the pupal stage post irradiation. This experimental design represents a simple approach to determine the overall physiological response of *Drosophila* to ionizing

radiation. In this thesis work, this basic framework was used as a method to explore the influence of dose, dose-rate, particle type, and energy on the radiobiology of normal tissues.

Chapter 4

Lead-doped Scintillator Dosimeters for Detection of Ultrahigh Dose-rate X-rays

The following work was published in *Physics in Medicine and Biology* in 2022 and can be found at the following DOI: 10.1088/1361-6560/ac69a5.

4.1 Summary

Objective: Lead-doped scintillator dosimeters may be well suited for the dosimetry of FLASH-capable x-ray radiotherapy beams. Our study explores the dose rate dependence and temporal resolution of scintillators that makes them promising in the accurate detection of ultrahigh dose-rate (UHDR) x-rays.

Approach: We investigated the response of scintillators with four material compositions to UHDR x-rays produced by a conventional x-ray tube. Scintillator output was measured using the HYPERSCINT-RP100 dosimetry research platform. Measurements were acquired at high frame rates (400 fps) which allowed for accurate dose measurements of sub-second radiation exposures from 1 to 100 ms. Dose-rate dependence was assessed by scaling tube current of the x-ray tube. Scintillator measurements were validated against Monte Carlo (MC) simulations of the probe geometries and UHDR x-ray system. Calibration factors converting dose-to-medium to dose-to-water were obtained from simulation data of plastic and lead-doped scintillator materials.

Main Results: The results of this work suggest that lead-doped scintillators were dose-rate independent for UHDR x-rays from 1.1 to 40.1 Gy/s and capable of measuring conventional radiotherapy dose-rates (0.1 Gy/s) at extended distance from the x-ray focal spot. Dose-to-water measured with a 5% lead-doped scintillator detector agreed with simulations within 0.6%.

Significance: Lead-doped scintillators may be a valuable tool for the accurate real-time dosimetry of FLASH-capable UHDR x-ray beams.

4.2 Introduction

Ultrahigh dose-rate (UHDR) radiotherapy (RT) aims to simultaneously reduce treatment times and increase the quality of cancer treatment. By triggering the so-called FLASH effect, UHDR treatments can potentially spare damage to healthy tissue, when compared with conventional low dose-rate RT (CONV-RT), while delivering an isoeffective dose to tumours in sub-second irradiations [12][194][32][13]. Adoption of a UHDR treatment paradigm, in which single-fraction or hypo-fractionated FLASH-RT schedules might be conceived [38], could foster improved patient outcomes, by increasing the therapeutic index and freezing organ motion, while also providing opportunities to increase patient throughput in the clinic. Radiobiologists, however, do not yet fully understand the mechanisms by which UHDR radiotherapy can engage the sought after benefit of the FLASH effect [113][114].

To elucidate the biological mechanisms behind FLASH, and maximally exploit the defining tissue sparing effects, it is essential that the dosimetric properties of the requisite UHDR radiation sources are characterized both accurately and reproducibly. To date, the FLASH effect has been observed with several types of particle radiation, including electrons [33], protons [195], and heavy ions [119] in addition to x-rays [196], which will be the focus of this work. However, the ability to measure dose accurately and precisely at FLASH-compatible dose rates (often referenced as >40 Gy/s), and across various radiation modalities, remains a primary concern. Various dosimeters commonly employed to measure CONV-RT dose rates, which are on the order of 0.1 Gy/s, have been shown to be inappropriate for this task due to strong dose-rate dependencies. Examples notably include, ionization chambers and some solid state (i.e. diode) detectors, which offer online measurement capabilities that are vital to a rapid real-time UHDR beam monitoring system and can enable current cut-off under off-normal beam conditions. This is especially true for pulsed radiation sources which may employ very high dose-per-pulse (DPP), for which saturation effects can become difficult to correct, inclusive of the electron linear accelerators that are ubiquitous within the literature for FLASH-RT [67][194]. As such, there yet remains a need to adapt or find new traceable reference dosimeters as well as relative dosimetry techniques that can enable dose monitoring for patient treatments, especially where active dosimetry is concerned.

X-rays produced by linear accelerators for CONV-RT are routinely measured with ionization chambers and radiochromic film. Ionization chambers are commonly used as reference dosimeters with a traceable calibration and offer the capacity for online dose monitoring. Moreover, they can be successfully employed in continuous UHDR x-ray [197] and proton sources [198][199] with careful application of conventional protocols (i.e. TRS 398), assuming the source may be considered continuous. Unfortunately, they also require laborious

dose-rate dependent calibration factors, complicating their use for commonly-used pulsed (i.e. linear accelerator) radiation sources which can produce dose rates spanning the range suitable for CONV-RT and FLASH-RT [67]. Film, on the other hand, provides excellent spatial resolution, but lacks the temporal resolution needed for dosimetry of UHDR beams. Specifically, the response of film to ionizing radiation changes over time and generally requires careful post-irradiation redoubt procedures, and are incompatible with the real-time dosimetry needs of FLASH-RT in view of clinical translation. Nevertheless, the dose-rate independence [200][201] of radiochromic film makes it well suited to pre-treatment dose verification and quality assurance protocols.

In contrast with the previously mentioned technologies, plastic scintillator dosimeters, which respond to ionizing radiation by emitting optical light, may be a suitable alternative for UHDR dose measurements due to their dose-rate independence and high temporal resolution [15][16][17][18]. Further, the ability to read out the signal from scintillators in real-time conveys a clinical advantage over dose-integrating dosimeters by enabling online dosimetry and beam monitoring compatible with adaptive radiotherapy protocols [202]. The relative tissue-equivalence of plastic scintillators without inorganic doping also confers a distinct advantage by circumventing the need for additional energy dependent correction factors that may complicate the calculation of dose-to-water (or tissue). This contrasts with inorganic scintillators which trade tissue-equivalence for superior radiation hardness and detection efficiency [203]. While inorganic scintillators offer reduced temporal resolution compared to organic materials by an order of magnitude, they maintain fast decay times in the range of tens of nanoseconds [204]. To date, some evidence supporting the use of scintillation detectors in UHDR x-ray fields exists for point measurements in kilovoltage synchrotron beams [17] and for proton and electron beams using various 2D detectors [79]. Nevertheless, plastic scintillators, while demonstrated to be excellent dosimeters for CONV-RT, must be further tested in the short time-intervals and at ultrahigh dose-rates characteristic of FLASH-RT [95].

In this work, we demonstrate the feasibility of using plastic scintillators and hybrid lead-doped scintillators for dosimetry of continuous, low energy (80 to 120 kVp) UHDR x-rays produced by a conventional x-ray tube equipped with a beam shutter system [40][18]. Temporal resolution is assessed by measurement of sub-second irradiations and dose rate independence (i.e. linearity of response to dose rate) is investigated by measuring both UHDR and CONV-RT dose rates with the same x-ray source.

4.3 Materials and methods

4.3.1 Ultrahigh Dose Rate X-ray System

All irradiation experiments described in this work were conducted using an MXR-160/22 conventional x-ray tube (Comet, Flammatt, Switzerland). The x-ray tube was modified with an in-house designed, removable shutter system (Figure 4.1), allowing samples to be placed within 2.5 cm of the x-ray focal spot and exposed to x-rays for a user-defined duration [18]. The beryllium window of the x-ray tube was positioned 1.69 cm from the x-ray focal spot and recessed 0.75 mm from the face of a 2.5 mm thick tungsten shutter wheel which shielded samples from radiation exposure. The shutter wheel rotated a 1 mm wide rectangular slit using a stepper motor to allow UHDR x-rays to reach the scintillators placed in a 0.2 mL test tube (Fisher Scientific, Nepean, ON, Canada). Using this system, dose rates of 114 Gy/s to water have been achieved [40]. The dose rate can be scaled by adjusting the tube current and the total dose delivered to a sample can be specified by changing the speed of the shutter wheel.

4.3.2 Scintillator Detectors

Four scintillators with different material compositions were used to measure light output in response to UHDR x-rays. Each of the scintillators was constructed according to the schematic shown in Figure 4.1 and the composition detailed in Table 4.1. The active scintillating volumes were 3.6 mm long with a diameter of 0.97 mm. A cap 3.6 mm long and 2.5 mm in diameter sealed the active volume from light contamination and protected it from physical damage. The dimensions of each of the probes were verified with x-ray images acquired using a photon-counting detector.

Table 4.1: Material composition of scintillators by mass and their mass densities.

Probe	**Composition**	**Density (g/cm^3)**
BCF-10	C: 92.6%, H: 7.74%	1.050
Pb 0.5%	C: 91.66%, H: 7.84%, Pb: 0.5%	1.101
Pb 1.4%	C: 90.85%, H: 7.75%, Pb: 1.4%	1.194
Pb 5%	C: 89%, H: 6%, Pb: 5%	1.562

4.3.3 Scintillator measurements

In this work, scintillator response to UHDR x-rays was characterized by radiation experiments within the x-ray shutter system. Dose rate independence was evaluated by varying

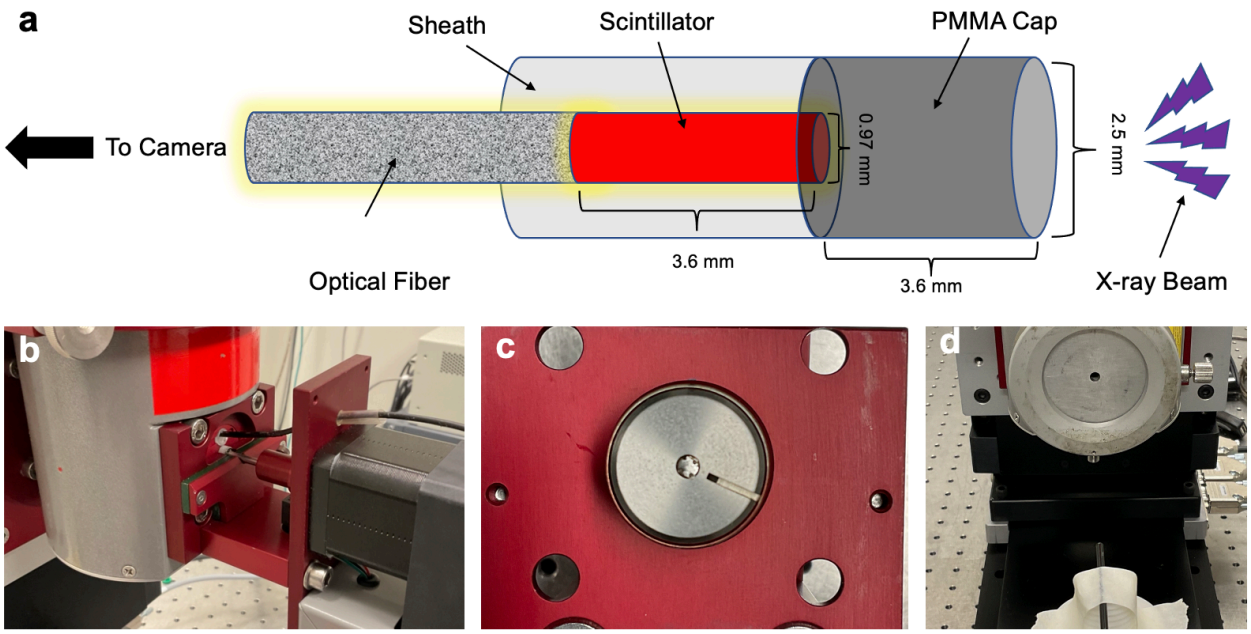

Figure 4.1: A schematic of the scintillator construction and orientation relative to x-rays (a). Experimental setup with a scintillator placed in the x-ray shutter system (b), with the 2.5 mm thick tungsten shutter wheel allowing x-rays to pass through the 1 mm wide slit (c). Measurements at extended SDD were taken without the shutter system in place, and a 5 mm diameter collimator shaping the beam (d).

tube current from 1.0 to 37.5 mA at a fixed exposure setting of 50 ms. The temporal resolution of each scintillator was investigated using 80 kVp 25 mA x-rays and shutter exposure settings from 1 to 100 ms. The shutter exposure setting controls the rotational speed of the shutter wheel. Slower speeds result in longer exposures to x-rays as the 1 mm rectangular aperture sweeps across the sample holder. Energy dependence experiments were conducted by irradiating each scintillator with 80, 100, and 120 kVp tube voltages with a fixed tube current of 25 mA and a shutter exposure setting of 50 ms. Scintillator measurements outside the shutter system at source-to-detector distances (SDDs) of 10 to 20 cm were also conducted at 80 kVp, 2.5 mA, to verify the ability to measure CONV-RT dose rates. For these measurements, the 5% Pb scintillator was taped to a motion stage and the x-ray beam was shaped with a 5 mm diameter lead collimator as shown in Figure 4.1d.

Scintillator light output was measured using the HYPERSCINT dosimetry research platform (HYPERSCINT-RP100, Medscint, Quebec, Canada). All scintillator measurements were acquired over 5 second intervals, with a frame rate of 400 fps (2.5 ms integration time). A background reading was acquired and subtracted from measurement for each scintillator on each day of data acquisition. For all scintillator irradiation experiments, three trials were recorded.

4.3.4 Monte Carlo simulations

The scintillator measurements in this study were validated and normalized using Monte Carlo (MC) simulations of the irradiation setup and probe geometries. Phase-space files for 80, 100, and 120 kVp tube voltages with 21.6×10^6, 26.8×10^6, and 31.6×10^6 photons, respectively, were produced with EGSnrc/BEAMnrc [205] and then used in TOPAS [206][207] to score dose within the active scintillator volume of each scintillator. The x-ray shutter system and scintillator geometries shown in Figure 4.1 were accurately modelled within TOPAS using probe compositions listed in Table 4.1. The components of the scintillators were modeled as described by Cecchi *et al.* [18]. The simulated probe geometry was determined using the x-ray image of the 5% Pb probe (the active scintillator was visually discernible due to the high concentration of Pb). The same probe geometry (shown in Figure 6.1) was used for each of the scintillator material compositions. In addition to the lead-doped and plastic scintillators, a simulation of dose-to-water in the place of the scintillator material using the same probe geometry was included. For each probe, 81 shutter positions were simulated, in 0.5° steps (spanning a 40° rotation). This was repeated 10 times with unique random seeds before combining into a single simulation. Scored dose (Gy) for each shutter position was normalized by the number of initial electrons simulated in the EGSnrc simulation and then scaled by tube current to obtain dose rate (Gy/s). The duration of each shutter position was determined using the angular velocity of the stepper motor for various exposure settings.

4.3.5 Data Analysis

For temporal dose rate profiles, the three trials acquired for each scintillator measurement were aligned using the maximum output and averaged to obtain a single dose rate profile. The measured exposure duration was determined by calculating the full width at half maximum (FWHM) for each scintillator measurement for exposure settings from 1 to 100 ms. The mean and standard deviation of the five measurements at each exposure setting were taken as the measured FWHM and error, respectively. The signal-to-noise ratio (SNR) was calculated for each scintillator according to:

$$SNR = \frac{SO_{max}}{SO_{SD}} \tag{4.1}$$

where SO_{max} is the maximum scintillator output from a 80 kVp, 25 mA, 10 ms exposure, and SO_{SD} is the standard deviation of the scintillator output from 50 frames measured with the shutter wheel blocking the beam.

For dose measurements, the mean and standard deviation of the three integrated scintillator signals were calculated as the measured dose and error, respectively. Scintillator output recorded in arbitrary units of light output was normalized using MC simulation data

for each of the measured probes. For temporal dose rate profiles, scintillator output from each frame was scaled by a correction factor, cf, defined as:

$$cf = \frac{MC_{max}}{SO_{max}} \tag{4.2}$$

Where MC_{max} is the maximum dose rate to medium (Gy/s) calculated from simulations, and SO_{max} is the maximum scintillator output. To compare with simulation data, the measured and simulated profiles were fit with a Gaussian and aligned to their maximum output and dose rate, respectively.

For dose measurements, including dose as a function of tube current, and shutter exposure setting, scintillator output was integrated using the full width at tenth maximum (FWTM). The scintillator measurements were then normalized using the integrated FWTM dose to scintillator material (Gy) of the MC data at 80 kVp and 25 mA tube current. To assess the energy dependence and water equivalency of the probes, calibration factors from dose-to-medium to dose-to-water were calculated from simulations for each scintillator material and tube voltages of 80, 100, and 120 kVp. The calibration factor was defined as

$$\text{calibration factor} = \frac{D_W}{D_{scintillator}} \tag{4.3}$$

where D_W, and $D_{scintillator}$ are the FWTM integrated doses to water and to scintillator material, respectively. The calibration factors were then validated by converting dose-to-medium to dose-to-water for scintillator measurements at each tube voltage and comparing with simulated dose-to-water. All data analysis was conducted using Python (v3.8.2).

4.4 Results

Figure 4.2 shows the measured and simulated dose rate to each scintillator as a function of exposure time for 10-ms and 100-ms shutter exposures. Each measured scintillator temporal profile matched well with MC. Measured SNR for each of the scintillators is listed in Table 4.2. The lead-doped probes showed the highest SNR values, with the 1.4 and 5% probes an order of magnitude greater than the pure plastic scintillator, BCF-10.

The maximum instantaneous dose rates absorbed by the scintillators were calculated from MC simulations for each of the probe compositions and are reported in Table 4.3. Due to the 3.6-mm attenuating cap on each of the probes, only the 5% lead-doped probe absorbed dose rates to scintillator medium above the typical 40 Gy/s UHDR threshold. By scaling tube current from 1.0 to 37.5 mA for a tube voltage of 80 kVp, maximum instantaneous dose rates of 1.1 to 40.1 Gy/s were obtained for the 5% lead-doped scintillator.

Table 4.2: Measured SNR for each scintillator exposed for 100 ms to 80 kVp, 25 mA x-rays.

Scintillator	SNR
Pb 5%	1146.2
Pb 1.4%	1216.9
Pb 0.5%	670.8
BCF-10	140.3

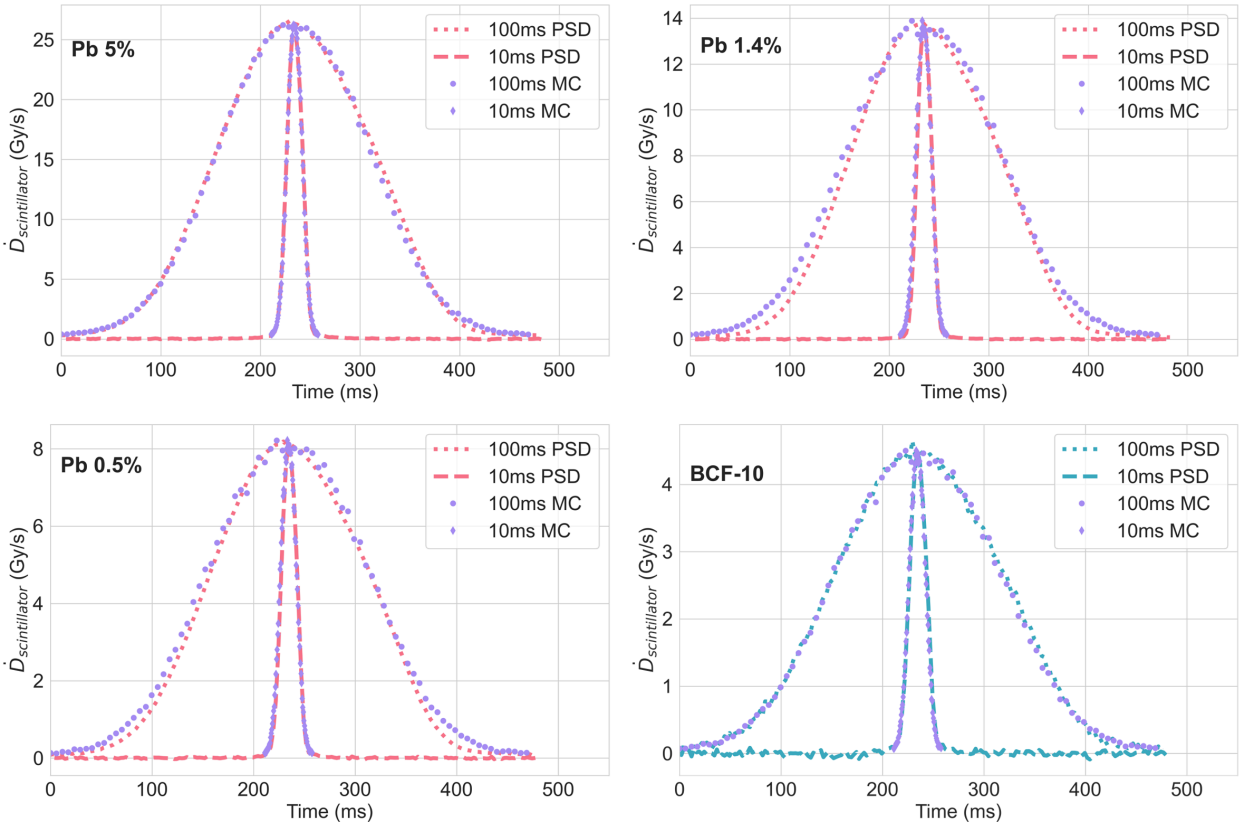

Figure 4.2: Dose rate to medium as a function of time for 10 and 100 ms shutter exposure settings. Measured scintillator output is shown with MC simulations for all probes for 80 kVp 25 mA x-rays.

4.4.1 Shutter time linearity

Normalized scintillator output presented in Figure 4.3 showed excellent agreement with simulations for each of the probes for shutter exposure settings from 1 to 100 ms. Measured dose exhibited a linear relationship with shutter setting for all probes ($R^2 > 0.9999$). The actual exposure time for a sample within the shutter system depended on the dimensions of the irradiated sample. The measured FWHM of the dose rate profiles for the scintillators

Table 4.3: Maximum dose rate to medium (Gy/s) from simulation data for each scintillator composition as well as dose-to-water at 37.5 mA for 80 kVp and 25 mA for both 100 and 120 kVp.

Scintillator	80 kVp	100 kVp	120 kVp
Pb 5%	40.1	35.2	43.0
Pb 1.4%	21.2	18.1	21.0
Pb 0.5%	12.8	10.7	12.3
BCF-10	7.1	5.8	6.6
Water	14.4	11.6	13.1

exhibited a linear relationship with shutter exposure setting, as shown in Figure 4.4.

4.4.2 Tube current linearity

Measured dose presented in Figure 4.5 showed a linear relationship with tube current from 1.0 to 37.5 mA for each of the four scintillators irradiated with a 50 ms exposure setting. The lead-doped scintillators demonstrated the most linear behaviour with $R^2 > 0.999$ compared to the plastic BCF-10 probe with $R^2 > 0.99$.

4.4.3 Response to x-ray tube voltage

Calibration factors converting from dose-to-medium to dose-to-water are shown in Table 4.4. The lead-doped scintillators exhibited greater energy dependence than the BCF-10 probe, with calibration factors decreasing with tube voltage. While the 0.5% Pb probe is near tissue equivalent, with a calibration factor of 1.094, the BCF-10 is the least energy dependent, with a coefficient of variation of 0.68% calculated from the three calibration factors. The energy dependence of the lead-doped probes is also evident from the ratio of maximum dose-rates shown in Figure 4.6. Scintillator output normalized to 80 kVp MC data and converted to dose-to-water using the energy dependent calibrations factors from Table 4.4 agreed with water simulations within 5% for the lead-doped probes, and within 8% for the undoped BCF-10. The 5% Pb probe showed the best agreement with simulations, measuring dose-to-water within 0.6% for both 100 and 120 kVp. The dose-to-water measured from each probe and percent difference from simulated dose-to-water is shown in Figure 4.7.

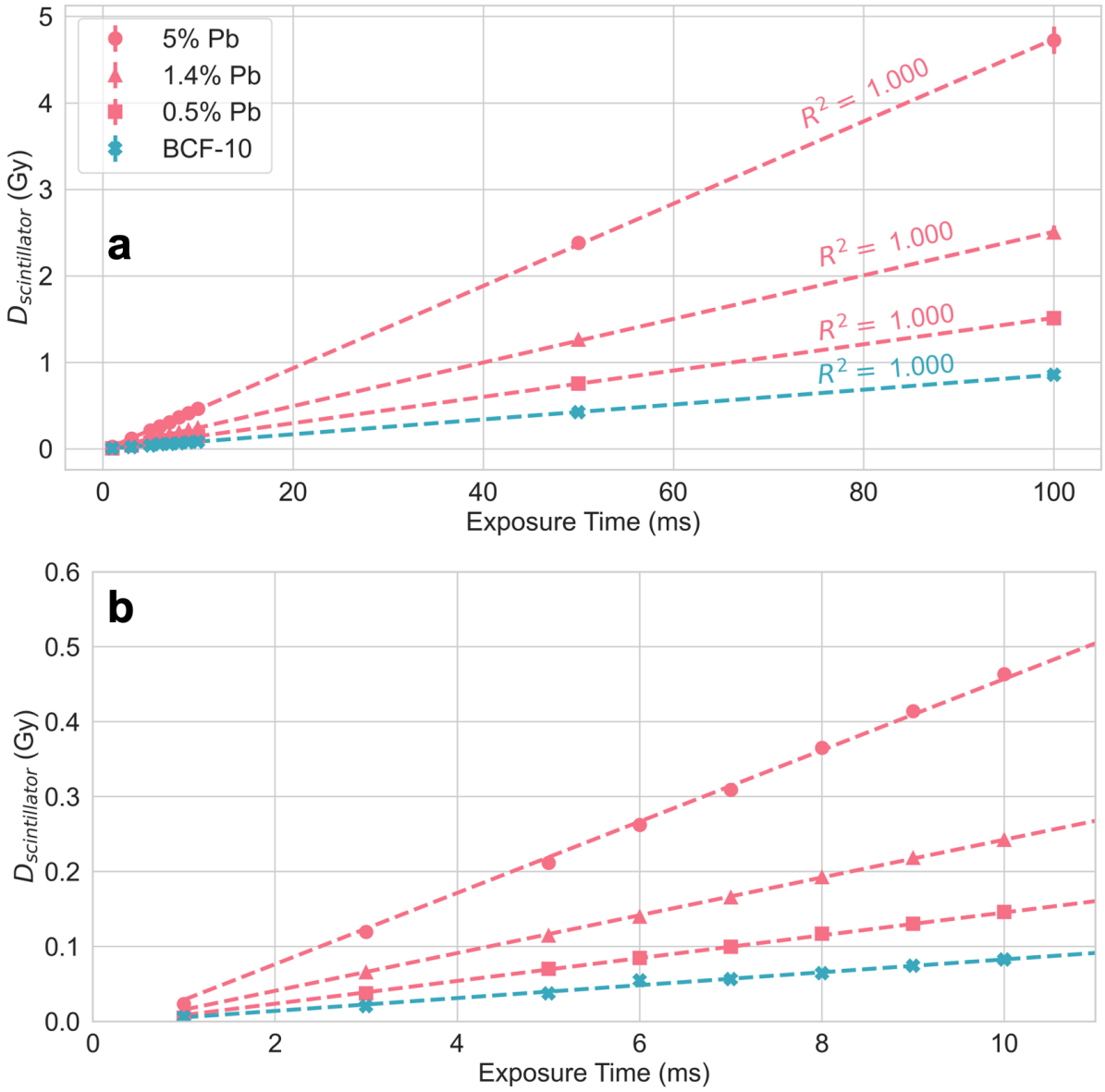

Figure 4.3: Dose linearity with shutter exposure setting: 1 to 100ms (a) and 1 to 10 ms (b) for 80 kVp, 25 mA measured with all probes. The same linear fit is shown in both plots. Scintillator output was normalized to MC data for the 100 ms exposure setting.

4.4.4 Extended SDD measurements

Scintillator measurements taken outside the shutter system at increasing SDD shown in Figure 4.8 confirmed that the dose fall-off follows an inverse square law (ISL). By reducing tube current from 25 mA to 2.5 mA and increasing the distance from the x-ray focal spot, CONV-RT dose rates of 0.1 Gy/s can be obtained by the 5% Pb scintillator at a tube voltage of 80 kVp.

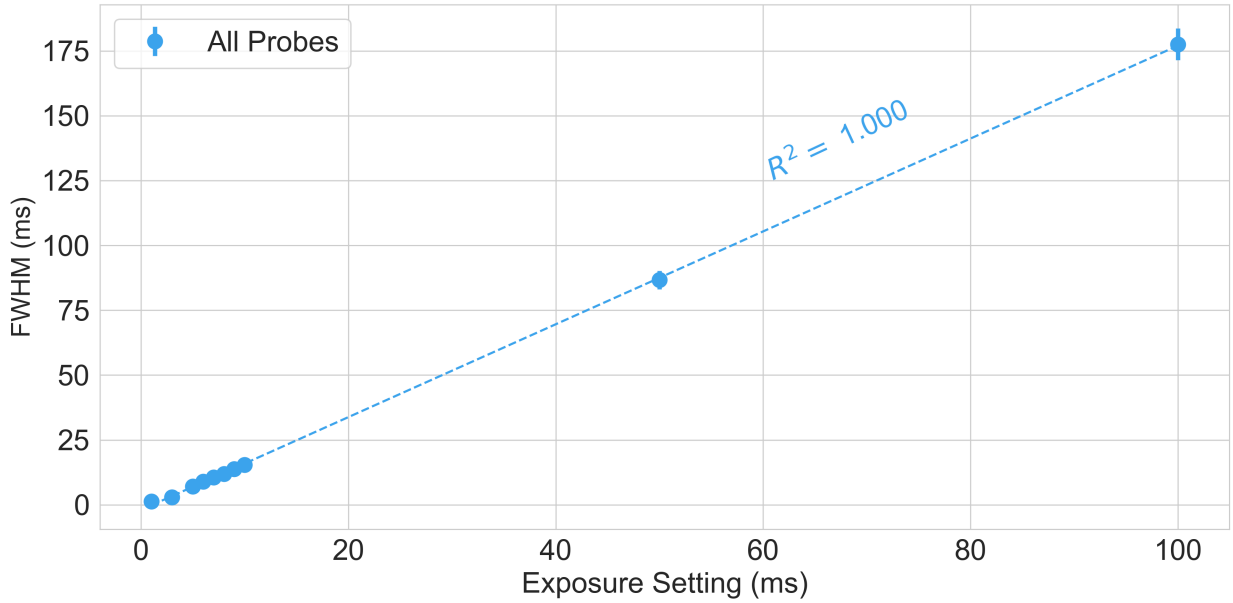

Figure 4.4: Measured FWHM (ms) of the scintillator output as a function of exposure setting. The average FWHM of the five scintillators is shown.

Table 4.4: Calibration factors from dose-to-medium to dose-to-water for each of the scintillator materials. The calibration factor was defined as the ratio of dose-to-water to dose to scintillator material for 80, 100, and 120 kVp tube voltages.

Scintillator	**80 kVp**	**100 kVp**	**120 kVp**	**Mean Cal**	**CV**
Pb 5%	0.370	0.343	0.316	0.331	6.85 %
Pb 1.4%	0.700	0.671	0.637	0.648	3.56 %
Pb 0.5%	1.159	1.126	1.091	1.094	2.28 %
BCF-10	2.059	2.038	2.008	2.013	0.68 %

4.5 Discussion

The principal aim of this investigation was to demonstrate that scintillators maintain dose rate independence and excellent temporal resolution when used to measure UHDR kilovoltage x-rays delivered in sub-second irradiations. After validating the response of each of the probes with MC simulations, we confirmed that the integrated scintillator signal captured at a frame rate of 400 fps followed a linear relationship with exposure durations of 1 to 100 ms, as shown in Figure 4.3. All four probes exhibited dose rate independence, based on linearity of response to varying tube currents as can be seen in Figure 4.5. While all probes were irradiated under the same conditions, because of differences in energy absorption coefficients of the different material compositions, only the 5% lead-doped scintillator absorbed dose

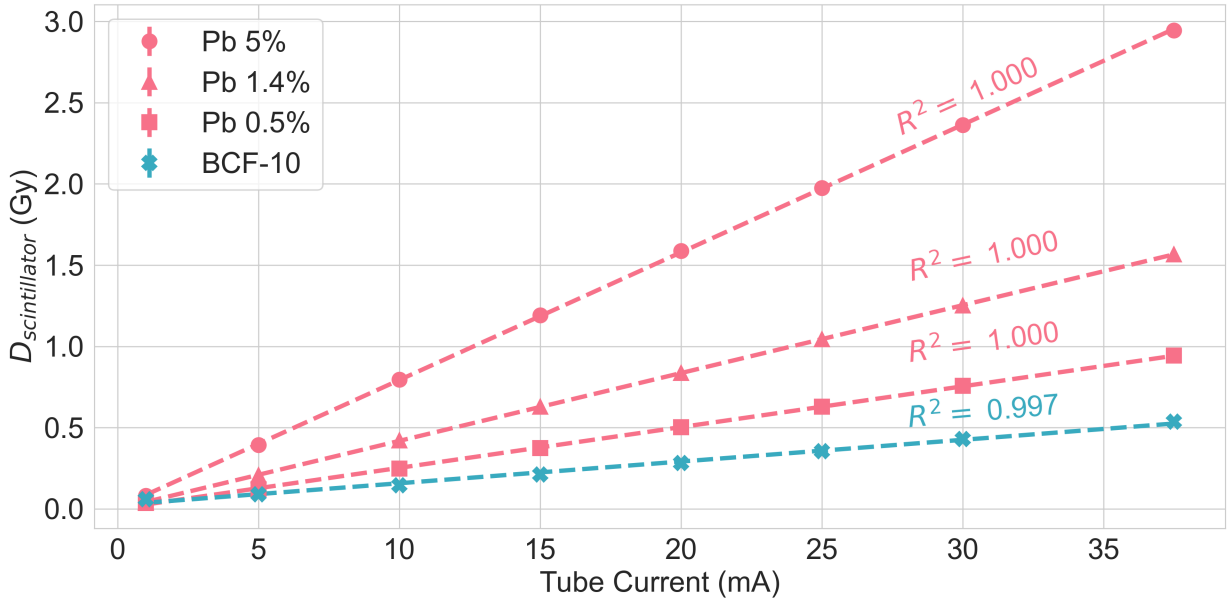

Figure 4.5: Dose linearity with tube current (1.0 to 37.5 mA) for 80 kVp measured with all probes. Measured scintillator output was normalized to MC data for a 50 ms exposure setting and 25 mA tube current. All scintillator measurements were taken at an exposure setting of 50 ms.

rates reaching UHDR of 40.1 Gy/s for a tube voltage of 80 kVp and tube current of 37.5 mA.

The HYPERSCINT-RP100 system used in this work is described and characterized elsewhere [96][208][18]. The spectrometer is composed of an array of cooled photodetectors that collect the spectral information of the light. The signal coming from the optical fiber is therefore spread over numerous photodetectors which allows the recorded signal to be far below saturation. The light detection efficiency of the photodetector array is ~ 2 counts per photon across the spectral range of 400 to 700 nm according to the dosimetric characterization performed by Jean *et al.* [96]. While this relatively high sensitivity could threaten saturation at ultrahigh dose-rates, this can be overcome by reducing the signal integration time and operating at high frame rates, as in this work. It is important to note that the performance characteristics of the scintillators reported in this work apply only to the combination of the scintillators and the HYPERSCINT-RP100 spectrometer together. Regarding scintillation quenching, plastic scintillators have typical response times in the ns range and therefore would not be affected by the dynamic of the beam here. Additionally, any partial dead-time would be accounted for as part of the calibration process. A continuous x-ray beam was used here and may not be subject to the same limitations as a pulsed beam.

The measurements taken at extended SDD confirmed that the unfiltered 80 kVp x-rays

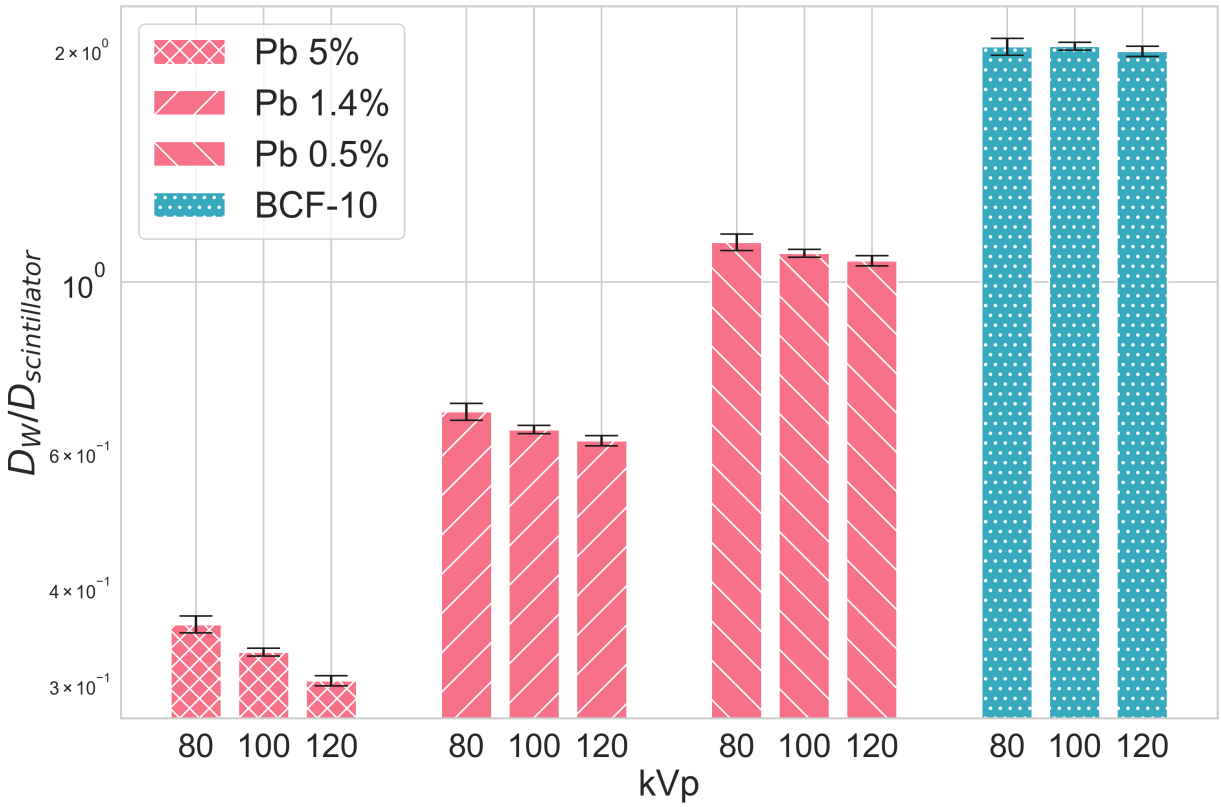

Figure 4.6: Water equivalency of scintillator detectors. The ratio of maximum dose rate to water to maximum dose rate to scintillator material from simulations is shown for tube voltages of 80, 100, and 120 kVp.

produced by the conventional x-ray tube in our system followed an ISL dose-rate fall off and allowed production of both UHDR and CONV-RT dose rates by adjusting tube current and distance from the x-ray focal spot. While the dose absorbed by the plastic scintillators was below the threshold for UHDR, this is due in part to the long 3.6-mm cap. The difference in μ_{en}/ρ between water and the polystyrene-based plastic scintillators (BCF-10) also results in a reduction of absorbed dose by a factor of $\sim$2. This is confirmed by the mean calibration factor of 2.013 for BCF-10 shown in Table 4.4. For irradiations of small biological samples, the dose rates will be >100 Gy/s, as demonstrated in previous studies of this system [18][40]. This system therefore has the ability to serve as a low cost platform for radiobiological investigations of the FLASH effect. Radiation experiments with cellular spheroids and even small animals may be conducted using this system. The use of low energy, continuous x-rays for FLASH-RT is currently an under-investigated corner of the FLASH literature.

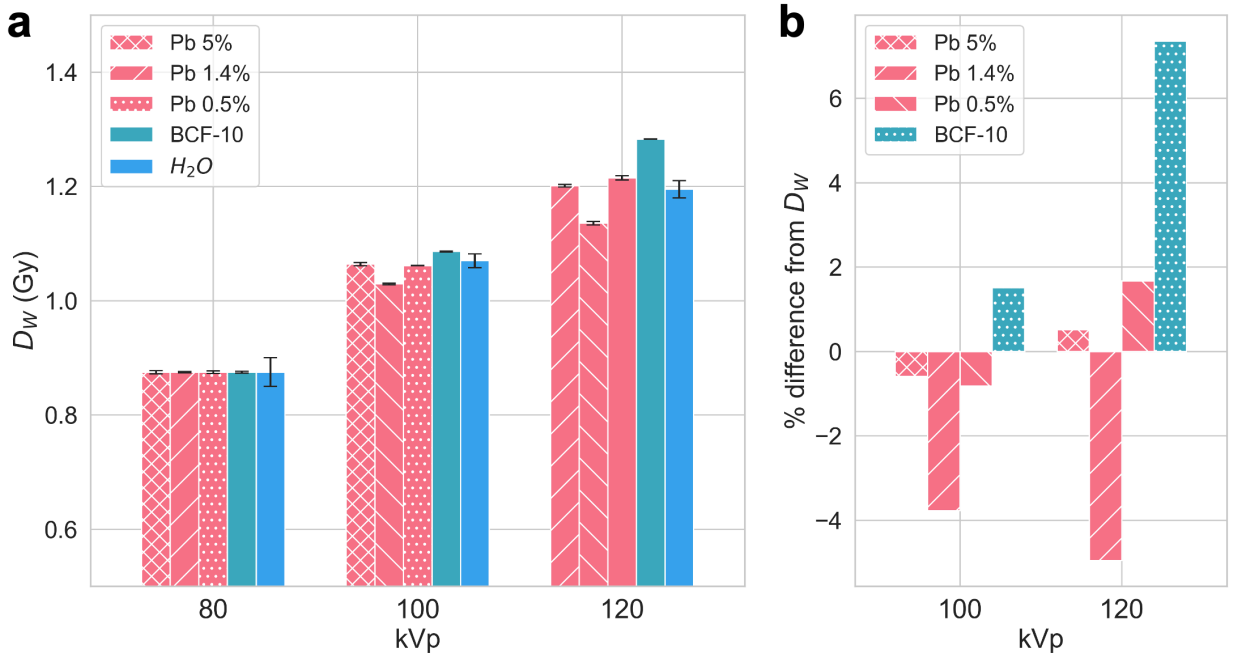

Figure 4.7: Measured dose-to-water for each scintillator detector, irradiated with 80, 100, and 120 kVp x-rays at a tube current of 25 mA and exposure setting of 50 ms. FWTM integrated scintillator output was normalized to dose from 80 kVp simulations for each scintillator material and then converted to dose-to-water (a). Percent difference from simulated dose-to-water is shown for measurements at 100 and 120 kVp (b).

4.5.1 Limitations

The lead-doped scintillators used in this work exhibited the least dose rate dependence. While this property makes lead-doped scintillators a compelling choice for UHDR dosimetry, they have the significant drawback of being non-tissue equivalent. Modifying the BCF-10 probe with a shorter cap would allow investigation of a near tissue equivalent detector at absorbed dose rates above the 40 Gy/s UHDR threshold.

The probe geometry used to simulate all probes was based on measurements from the x-ray images of the 5% Pb scintillator. However, based on the x-ray images of the 1.4 and 0.5% Pb probes, both the PMMA caps and the active scintillator volumes may be slightly shorter. This may explain the narrower temporal dose rate profiles for both 1.4 and 0.5% Pb probes compared with MC shown in figure 4.2. Inconsistencies in probe construction would have a significant impact on the measured SNR reported in Table 4.2. It is expected that SNR would increase with higher concentrations of Pb, but a shorter cap could explain the higher signal measured by the 1.4% Pb probe compared to the 5% Pb probe. Also, if the PMMA cap is less than the simulated 3.6 mm, the x-ray beam would be subject to less beam hardening which could explain the under response to 100 and 120 kVp x-rays of the

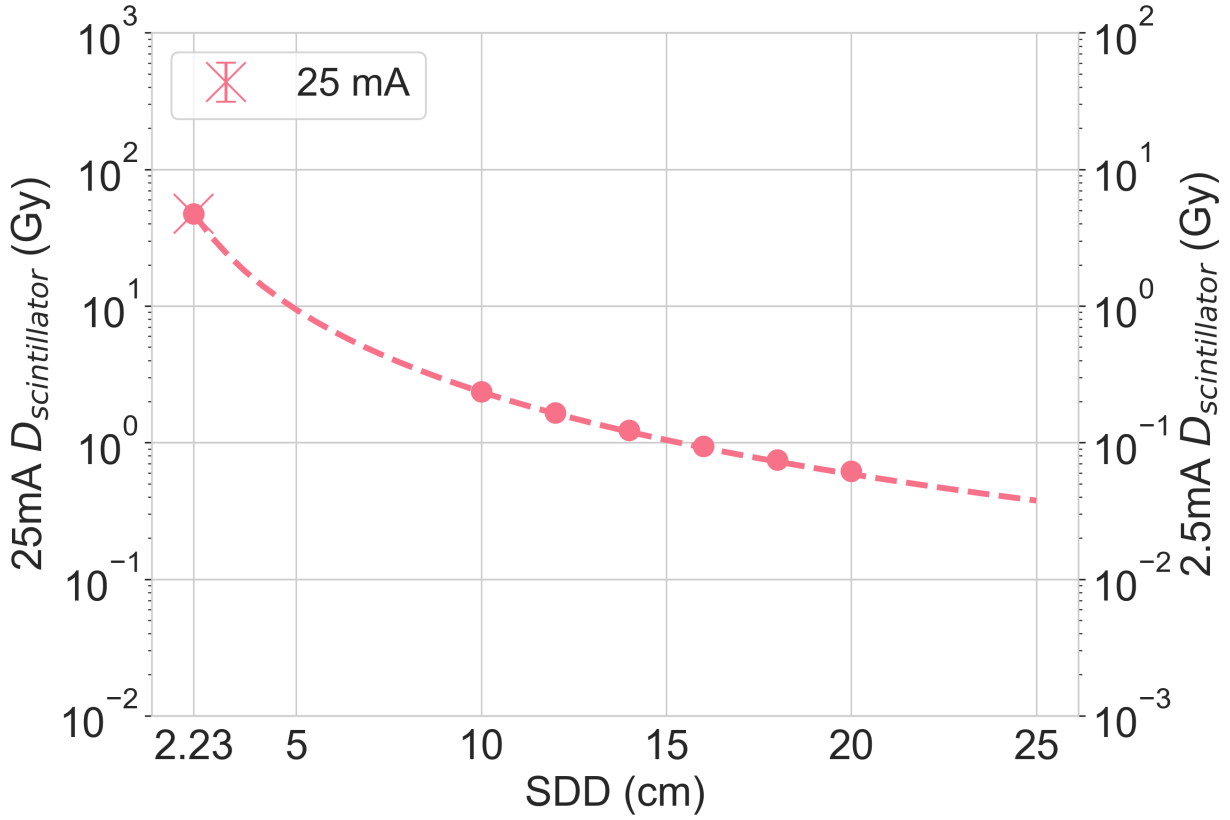

Figure 4.8: Integrated dose fall off at extended SDD for 80 kVp x-rays. Measured dose follows an inverse-square law relationship with distance from the x-ray focal spot. Normalized to 1 second exposure setting.

1.4% Pb scintillator when normalized to 80 kVp data as shown in Figure 4.7.

A noteworthy complication of using scintillators for dosimetry are the stem effects caused by Cherenkov radiation and radioluminescence, which must be corrected for at x-ray energies above the threshold of 178 keV [107][16]. As the highest tube voltage explored in this work was 120 kVp, stem effects were not considered. However, as described by Archer *et al.*, corrections must be applied when measuring higher energy sources with scintillators [17].

The x-ray shutter system used in this work is designed to expose UHDR x-rays to a sample by rotating the 1-mm wide rectangular slit through a single point in the selected exposure time. This results in an exposure time that is dependent on the dimensions of the sample or detector placed in the test tube, which has a diameter of 6.8 mm. The actual exposure time scales linearly as our results in Figure 4.4 show, but this design makes it more difficult to provide accurate dosimetry for samples of varying geometry. A future design which exposes the entire sample holder simultaneously could improve the usefulness of the system for more robust radiobiology studies.

4.6 Conclusion

This work has demonstrated that scintillators are suitable dosimeters for UHDR x-rays produced by a conventional x-ray tube. Experimental measurements with four scintillators of different material composition were compared to Monte Carlo simulations. Our results confirmed that scintillator response is linear with shutter exposure setting from 1 to 100 ms and with tube current from 1.0 to 37.5 mA (corresponding to dose rates of 1.1 to 40.1 Gy/s for the 5% Pb probe). Scintillator measurements of dose-to-water agreed with simulations for tube voltages of 80, 100, and 120 kVp. Finally, by extending the source-to-detector distance and and reducing tube current, conventional dose rates of 0.1 Gy/s were measured.

Chapter 5

High-throughput, low-cost FLASH: Ultrahigh dose-rate irradiation of *Drosophila melanogaster* with low-energy x-rays

The following work is under review for publication by the *Journal of Radiation Research*.

5.1 Summary

FLASH radiotherapy is an emerging technique in radiation oncology that may improve clinical outcomes by reducing normal tissue toxicities. The physical radiation characteristics needed to induce the radiobiological benefits of FLASH are still an active area of investigation. To determine the dose rate, range of doses, and delivery time structure necessary to trigger the FLASH effect, *Drosophila melanogaster* were exposed to ultrahigh dose-rate (UHDR) or conventional radiotherapy dose-rate (CONV) 120 kVp x-rays. A conventional x-ray tube outfitted with a shutter system was used to deliver 17 to 44 Gy doses to third instar *D. melanogaster* larvae at both UHDR (210 Gy/s) and CONV (0.2 - 0.4 Gy/s) dose rates. The larvae were then tracked through development to adulthood and scored for eclosion and lifespan. Larvae exposed to UHDR eclosed at higher rates and had longer median survival as adults compared to those treated with CONV at the same doses. Eclosion rates at 24 Gy were 68% higher for the UHDR group ($p<0.05$). Median survival from 22 Gy was >22 days for UHDR and 17 days for CONV ($p<0.01$). Two normal tissue sparing effects were observed for *D. melanogaster* irradiated with UHDR 120 kVp x-rays. The effects appeared only at intermediate doses and may be useful in establishing the dose range over which the benefits of FLASH can be obtained. This work also demonstrates the usefulness of a high-throughput fruit fly model and a low cost x-ray tube system for radiobiological FLASH research.

5.2 Introduction

The goal of modern radiation oncology is twofold: to deliver a sufficient dose of ionizing radiation to a tumour in order to stop the proliferation of cancer cells and also to minimize harm to normal tissue. Failure to achieve the latter can result in serious side effects and potentially cause additional cancers in the future. The conventional solution to this problem is to increase the conformality of radiotherapy treatments. Through techniques including intensity modulated radiotherapy (IMRT) and advances in the repeatability of patient positioning and image guidance, radiation dose distributions can be carefully sculpted to minimize radiation to healthy tissues [209]. Physicists and radiation oncologists have focused on effectively reducing the physical margins of radiotherapy but recently there has been renewed interest in the radiobiological differences between cancerous and healthy tissue [210]. Radiobiologists have turned their attention to dose rate as a potential tool to find differential biological responses. Many studies have suggested that delivering doses at so-called ultrahigh dose-rates (UHDR, $\geq$40 Gy/s) may cause less damage to normal tissue than conventional dose rates (CONV, $\sim$ 0.1 Gy/s) while maintaining cancer cell kill efficacy [13, 139]. This has been termed the FLASH effect.

Before treating human patients with UHDR radiation sources in hopes of benefiting from the FLASH effect, it is imperative to develop a robust radiobiological understanding of UHDR radiotherapy through animal studies. *Drosophila melanogaster* have been central to the study of radiobiology since before the development of the linear accelerators commonly used for radiotherapy. Herman Joseph Muller's fruit fly experiments in 1926-1927 led to his receiving the Nobel prize for the discovery of x-ray mutagenesis [173]. Research conducted by Muller's students also contributed directly to the development of the linear-no-threshold (LNT) model for radiation protection, which posits that there is 'no safe dose' of ionizing radiation[174, 175]. This work has faced scrutiny [176] and some have even suggested that there may be benefits to low doses of radiation [177]. Dose rate radiobiology using *D. melanogaster* models has recently gained attention, but the field has been limited to very low dose rates (on the order of CONV dose rates or lower). Low dose rate priming doses (0.2 Gy) have been shown to reduce DNA damage and impact gene expression [178]. Other groups have studied the effects of low dose rate background irradiation from cosmic rays by shielding *D. melanogaster* deep underground. These works have demonstrated a link between dose rate and genetic and phenotypic responses [179, 180].

Beyond their historical relevance to radiobiology, there is a compelling case to be made for radiobiological studies of *D. melanogaster* as an excellent model for human cancers. To date, the most influential works on the FLASH effect have included studies of mice, mini

pigs, cats [33, 13], and the early clinical trials with human patients [19]. It remains a serious issue that these studies involve low numbers of subjects with high heterogeneity of results. Development of new high-throughput models, such as *Caenorhabditis elegans*, would be helpful to increase the statistical power of radiobiological studies [211]. *D. melanogaster* is another such model that could provide greater statistics while also offering a genetic model with direct homologs to humans [188, 189]. Models for a number of human cancers have been developed for both larvae and adult *D. melanogaster* which can be used to develop new therapies [190]. Additionally, there are significant logistical advantages to working with fruit flies: no research ethics board approval is required, and results with large numbers of flies at various life stages can be procured on short notice. The life cycle of *D. melanogaster* is approximately 10 days from egg to emerged adult fly.

The irradiations described in this work were performed using a low-cost system based around a conventional x-ray tube [40]. FLASH research is typically an expensive undertaking, with most studies utilizing proton cyclotrons [118, 212] and experimental electron linear accelerators [32, 150]. The work described here seeks to demonstrate the viability and utility of a low-cost irradiation platform coupled with a high-throughput whole-organism. By irradiating late third instar *D. melanogaster* larvae with 120 kVp x-rays at UHDR and conventional dose rates we can gain insights about the range of doses and time structure of UHDR beams that are necessary to elicit the FLASH effect.

5.3 Methods

5.3.1 Flies

Wild-type *D. melanogaster* (Oregon-R) were used in this study. Post irradiation, larvae were placed in a fresh vial with an antifungal grape juice medium [25 ml grape juice, 75 ml water, 2.25 g agar, 0.15 g nipogin] and kept at 24°C. After emergence, adult flies were placed in Carolina Instant *D. melanogaster* Medium and flipped twice weekly. The incubator was set to a 12-hour light and dark cycle.

5.3.2 Irradiation Conditions

Late-third instar were immobilized with double-sided tape on acrylic cylinders for the irradiations. Control groups were given a mock irradiation (immobilized but not exposed to x-rays). Three larvae were immobilized and irradiated simultaneously as shown in Figure 5.1. For each experiment, at least 20 larvae were irradiated. Each experiment was repeated in triplicate on different days, for a total of 60 larvae irradiated per each dose and dose rate group.

5.3.3 Survival Analysis

Flies were scored for eclosion (complete emergence of adults from pupae) starting at 4 days post irradiation. Fractional eclosion for each dose group (eclosed adults/irradiated larvae) was normalized to the percent eclosion from the control group treated on the same day such that:

$$\%\,\text{eclosion} = \frac{\text{irradiated eclosion rate}}{\text{control eclosion rate}} \times 100\% \tag{5.1}$$

Adult flies were also tracked for survival up to 22 days post irradiation. Deaths were scored once daily and flies lost or damaged during transfer were right-censored. After flipping adults into new vials, the previous vials were kept in order to check for offspring production.

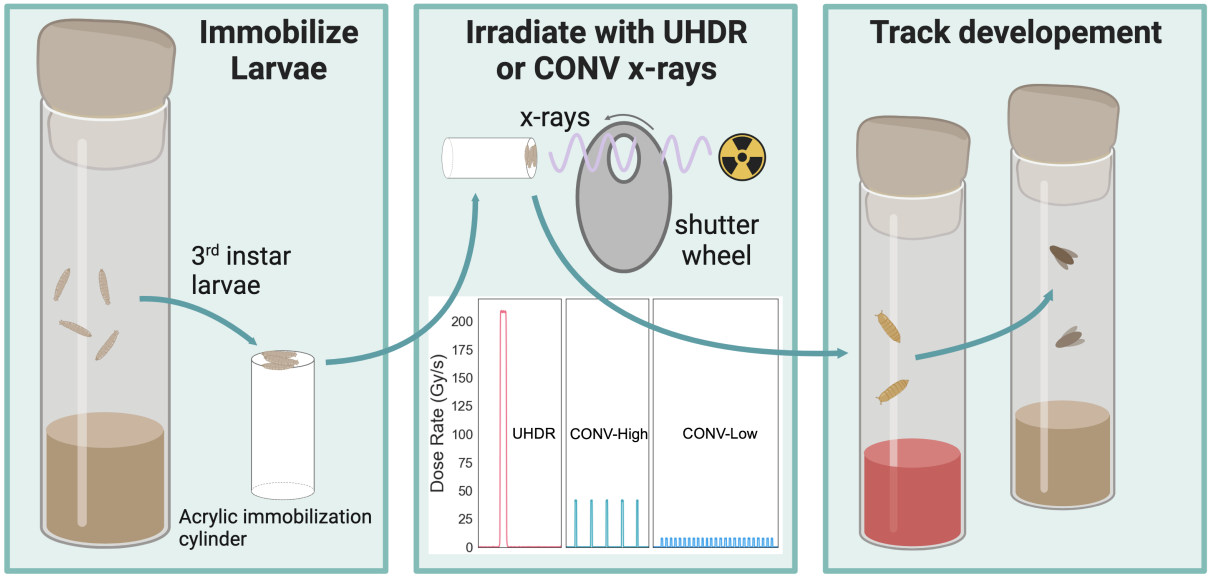

Figure 5.1: Procedure for immobilizing and irradiating third instar larvae *D. melanogaster* within the x-ray tube shutter system. The UHDR and CONV delivery schemes are shown in the second panel.

Statistical Analysis

All statistical analyses were performed with Python 3.8. Mann-Whitney U tests and Student's t-tests were performed to assess differences in eclosion between dose rate groups. Kaplan-Meier lifespan analysis was conducted using the lifelines package [213]. Results were regarded as significant for eclosion at $p < 0.05$. For lifespan analysis, log-rank tests were used and considered significant at $p < 0.01$.

5.3.4 X-ray System and Dosimetry

The irradiations described in this work were conducted using a conventional x-ray tube modified with a shutter system to precisely control exposure times. This system has previously been characterized elsewhere [40, 18, 22]. For these experiments, the tungsten shutter wheel was updated with a 5.1 mm diameter circular aperture as shown in Figure 7.2. This design functions by rotating the aperture into a fixed position for the duration of the exposure. The circular aperture allows for delivery of uniform dose distributions to a ∼5mm diameter area on the acrylic immobilization cylinder. For all irradiations the tube voltage was set to 120 kVp. For UHDR irradiations, a single pulse at a tube current of 25 mA was used. The width of the pulse (exposure duration) was varied between 75 and 200 ms to deliver doses from 17 to 44 Gy. For CONV treatments, tube current was reduced and additional pulses were delivered to reach the same total dose in a delivery time of ∼100 s, yielding average dose rates on the order of typical CONV treatments. CONV delivery regimens consisted of either 5 pulses at 5 mA with 25 second inter-pulse spacing (referred to as CONV-high) or 25 pulses at 1 mA with 4 second inter-pulse spacing (CONV-low) as shown in Figure 5.1. The ability to linearly scale dose rate with tube current and dose with shutter exposure time has previously been demonstrated [22].

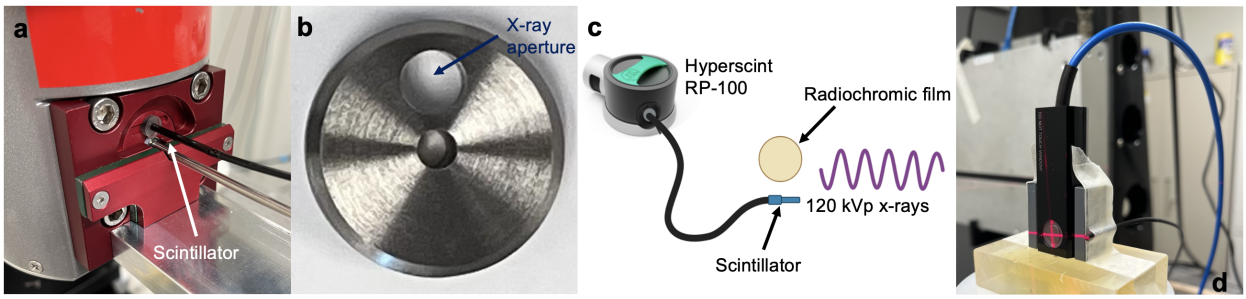

Figure 5.2: Conventional x-ray tube fitted with shutter system (a). Tungsten shutter wheel with circular aperture (b). Schematic of dosimetry methodology (c) and photograph of parallel plate ionization chamber calibration procedure (d).

Dosimetry was performed with plastic scintillator detectors (PSDs), ionization chambers, and radiochromic film to confirm the delivery of consistent doses at both UHDR and CONV dose rates. PSDs and films were calibrated with either a PTW 23342 parallel plate soft x-ray chamber (PTW, Freiburg, Germany) or PTW TN30013 Farmer chamber using the in-air method [214]. Laser cut EBT3 Gafchromic films (Ashland, Bridgewater, NJ) were placed on the surface of the acrylic immobilization cylinders providing a high spatial resolution 2D dose distribution measurement. Films were scanned 24 hours post irradiation with an Epson flatbed scanner (Expression 10000 XL, Epson, Long Beach, CA). Pixel values were

converted to dose using a red channel calibration curve generated with Farmer chamber measurements. PSDs connected to a hyper spectral dosimetry system, Hyperscint RP-100 (Medscint, Quebec City, QC), were used to measure light output from irradiations at a frame rate of 400 Hz.

5.4 Results

5.4.1 Dosimetry

The x-ray shutter system produced uniform 2D dose distributions on the surface of the acrylic cylinders, allowing three larvae to be irradiated simultaneously. PSD and film dosimetry confirmed that doses delivered with UHDR and CONV agreed within 0.1%. High temporal resolution measurements with the PSD also confirmed the time structure of the delivered radiation, i.e. the pulse width and inter-pulse spacing. The average dose rates (over the duration of the treatment) were determined from film measurements: 210 Gy/s for UHDR and 0.2 to 0.4 Gy/s for CONV.

5.4.2 Larva Development

Post irradiation, larvae developed into pupae and then emerged as adult flies several days later. The rate of survival to adulthood decreased with dose as shown in Figure 7.3 and described in Table 5.1. The average eclosion rate from all control groups was 86.1%. The overall dose response curves presented in Figure 7.3a do not differ significantly between UHDR and CONV ($p = 0.841$ from Mann-Whitney U test). However, at a dose of 24 Gy the mean emergence of adult flies was 60.5% for UHDR and 35.9% for CONV ($p = 0.0119$ from Student's t-test). From the sigmoidal fits of dose response, the LD_{50} was calculated to be 25.4 Gy for UHDR and 24.1 Gy for CONV. Eclosion rates for 22 Gy irradiations performed at UHDR and CONV-High and CONV-Low dose rates are presented in Figure 7.3b. The mean eclosion rate for CONV-Low was 4% lower than CONV-High and was not significant ($p = 0.5831$). Five replicates were used for the 24 Gy dose groups (n = 100 for both dose rates).

Irradiated *D. melanogaster* larvae that developed to adulthood showed several signs of physical radiation damage including severe deformity that prevented complete eclosion (which were not scored as emerged adults) and a range of wing malformations. These included wings that failed to completely open or close as well as partially developed wings. Examples of physical radiation damage to adult flies are shown in Figure 5.4.

No offspring were found in vials holding adults irradiated with 26 Gy UHDR (and greater), and 24 Gy CONV (and greater) indicating sterility of adults, though conclusions

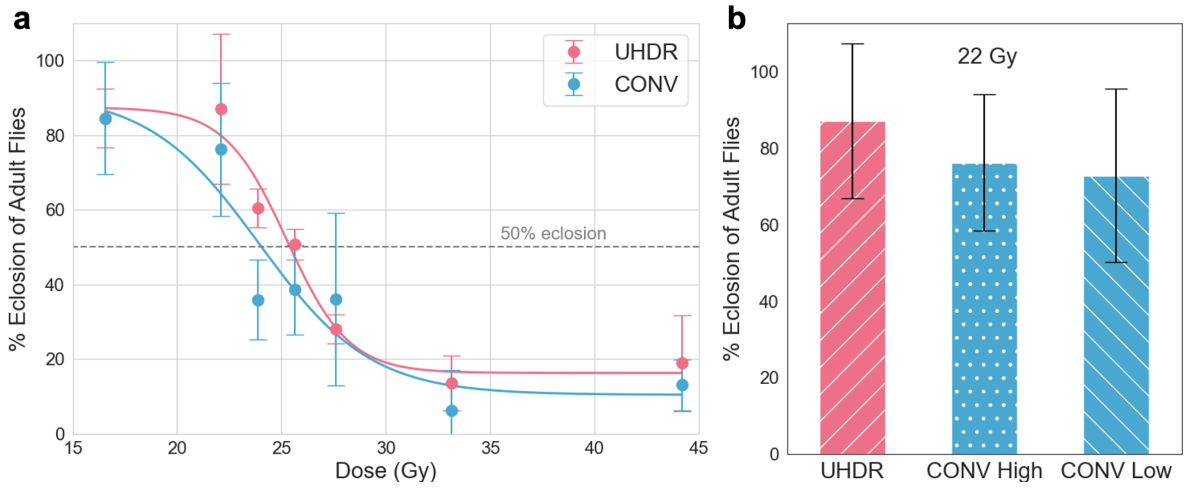

Figure 5.3: Eclosion (emergence as viable adult flies) irradiated with UHDR and CONV with doses from 17 to 44 Gy (a). Error bars show the standard deviation of three replicates (n = 60 for each dose). Comparison of eclosion rates from flies irradiated to 22 Gy with UHDR (1 × 25 mA, CONV-High (5 × 5 mA), and CONV-Low (25 × 1 mA) delivery regimens (b).

Table 5.1: Fraction of irradiated larvae which eclosed as adult flies normalized to control. * Statistically significant differences between UHDR and CONV eclosion rates.

Dose (Gy)	UHDR	CONV	UHDR/CONV	*p*-value
17	0.845	0.846	1	0.5021
22	0.839	0.762	1.10	0.2880
24	0.605	0.359	1.68	**0.0117***
26	0.507	0.386	1.32	0.0909
28	0.28	0.36	0.78	0.7072
33	0.136	0.062	2.17	0.1932
44	0.189	0.131	1.45	0.263

about sex specific sterility cannot be reached. Larvae and pupae were found in vials containing adult flies irradiated with 24 Gy UHDR (and lower), 22 Gy CONV (and lower), and in all vials from control flies.

Larvae irradiated with 24 Gy were scored daily for emergence from the pupal case. Figure 5.5 shows higher emergence of the UHDR irradiated flies compared to CONV at each day post irradiation. Emergence curves appear to be shifted vertically relative to the control group indicating that irradiations are not inducing a delay in eclosion.

Adult flies exposed to 22, 24, and 26 Gy as larvae were scored daily for survival up to 22 days post irradiation. The Kaplan-Meier estimator for probability of survival after irradiation is shown in Figure 5.6 and the median survival times are summarized in Table 5.2. The median survival times were 17 days for flies treated with either CONV-High or

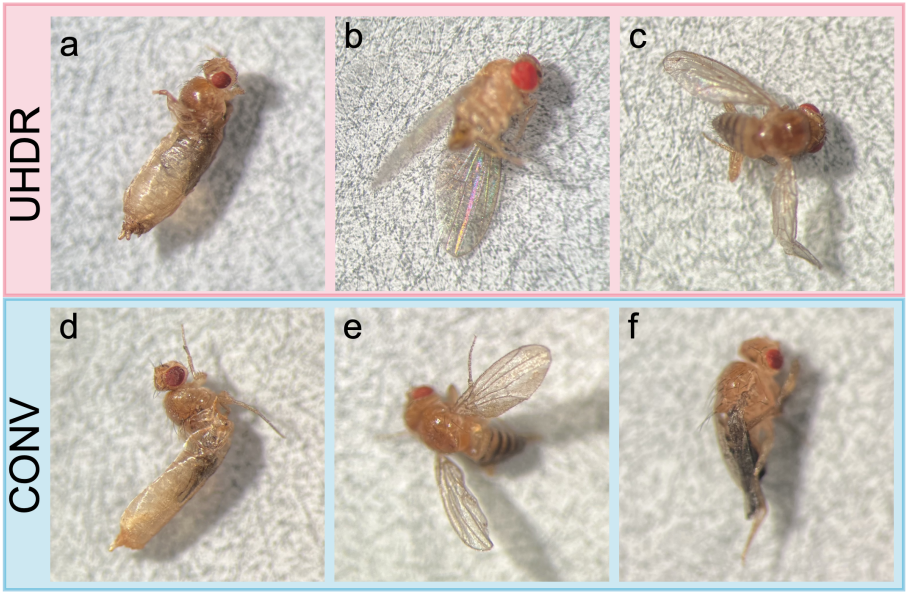

Figure 5.4: Emerged adult flies irradiated with UHDR and CONV x-rays at 24 Gy as larvae. Some flies from both dose rate groups were unable to fully eclose from pupae (a,d). Radiation damage also leads to wing abnormalities, including failure to close normally (b,e), and deformity (c, f).

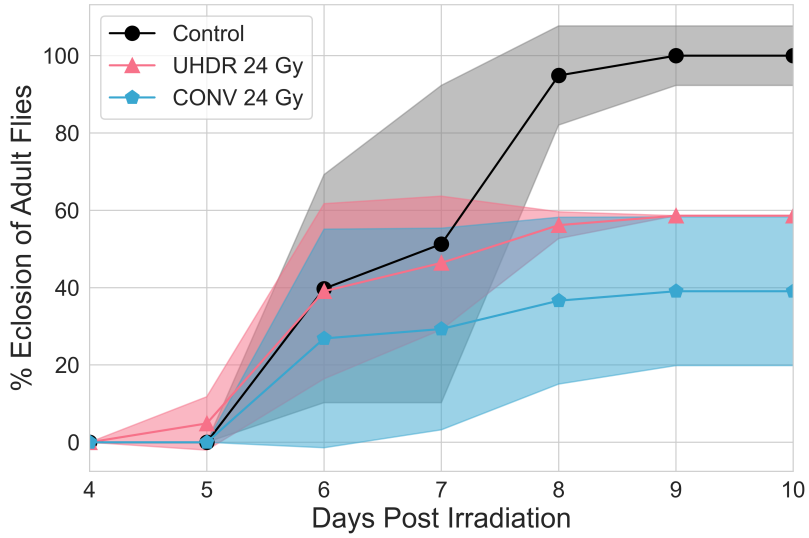

Figure 5.5: Time of emergence from pupal case of larvae irradiated with 24 Gy, normalized to the maximum eclosion of the control group. The shaded area indicates the standard deviation from three replicates.

CONV-Low at 22 Gy. The UHDR groups exhibited a median survival time greater than 22 days at 22 and 24 Gy, and 15 days at 26 Gy. The probability of survival was higher for

flies treated with UHDR at all time points post irradiation for both 22 and 24 Gy. The differences in log rank survival was significant for 22 Gy for both CONV-High and CONV-Low treatments ($p = 0.008$ and 0.009).

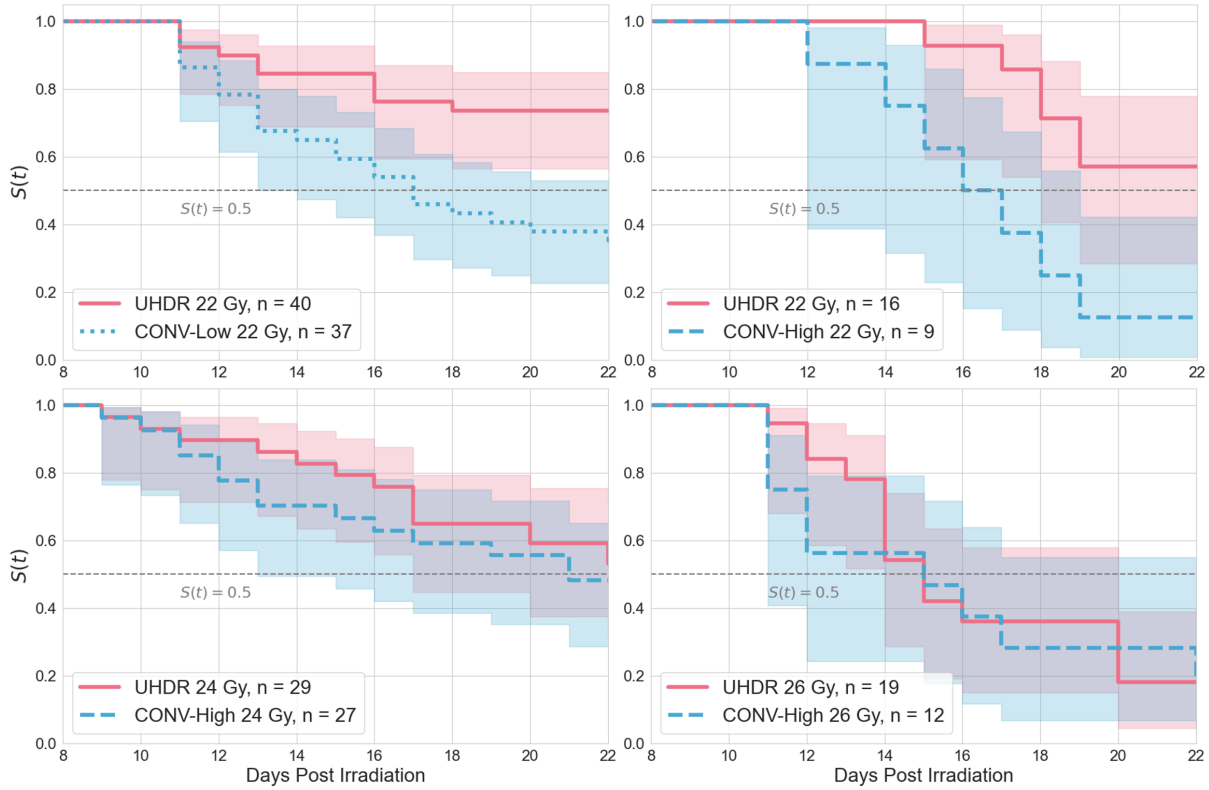

Figure 5.6: Kaplan-Meier survival estimator for emerged adults irradiated with 22, 24, and 26 Gy as larvae. The number of live adult flies included in the analysis is shown in the legend of each subplot. CONV-Low treatments are shown with a dotted line and CONV-High treatments are shown with a dashed line.

Table 5.2: Median survival times post irradiation for adult flies treated with 22, 24, and 26 Gy. *Statistical significance from log-rank test when p<0.01.

	UHDR	**CONV**	
Dose (Gy)	Median Survival (days)		p-value
22	>22	17	**0.009***
24	>22	21	0.286
26	15	15	0.735

5.5 Discussion

D. melanogaster larvae irradiated with UHDR x-rays exhibited normal tissue sparing compared to CONV treatments in two scenarios. Statistically significant differences were observed for increased eclosion rates of larvae treated with 24 Gy UHDR and extended lifespan for flies irradiated with 22 Gy UHDR when they were compared to the respective CONV irradiations. These effects could be considered acute and long-term effects of radiation damage which may have implications for determining dose limits in a radiotherapy context. Neither acute or long term sparing was observed for flies irradiated with doses <22 Gy or >26 Gy, indicating a possible threshold and limit for observing a FLASH effect given our study design. It is indeed expected that very low or very high doses would have similar responses regardless of dose rate. The magnitude of FLASH sparing has been shown to be dependent on dose, tissue type and the endpoint observed [215]. Previous studies have observed a threshold dose of ∼20 Gy for tissue sparing *ex vivo* and *in vitro*[155, 117]. Proton irradiations of zebrafish embryos have suggested a dose window for tissue sparing effects ∼10 - 50 Gy [118].

Interestingly, the two tissue sparing effects did not overlap at the same doses. The differences in eclosion rate at 22 Gy were not significant nor was the difference in lifespan for flies irradiated with UHDR and CONV at 24 Gy. The CONV treatments for 22 Gy were delivered with both CONV-Low and CONV-High regimens, both of which resulted in shorter median lifespans compared to the UHDR irradiated flies. This suggests that the difference in pulsed dose rates for CONV-Low and CONV-High (8.8 Gy/s compared to 44.2 Gy/s) is less important for triggering the longer time scale normal tissue sparing effects than the average dose rate over the duration of the treatment, which was 0.2 Gy/s for both. It should be noted that the median survival times calculated from the Kaplan-Meier estimator and reported in Table 5.2 suggest that flies irradiated with 24 Gy CONV survive longer than the 22 Gy CONV treatment. This is not indicative of a sparing effect from dose escalation and is in fact an artifact due to normalizing to the number of eclosed adult flies rather than the number of irradiated larvae. Note that fewer adults are included in the Kaplan-Meier analysis for 24 Gy than for 22 Gy shown in Figure 5.6.

While this work represents the first UHDR irradiation study of *D. melanogaster*, there are a number of studies on the dose response of *D. melanogaster* at different life stages. Insects are significantly more radioresistant than mammals, and *D. melanogaster* are no exception. However, there are great inconsistencies in the literature. One study found that the minimum dose to cause lethal damage to third instar larvae was 500 Gy, while the LD_{50} was 1429 Gy [216]. The LD_{50} reported varies widely depending on the definition of the endpoint used. For late third instar larvae, the LD_{50} is frequently cited as 4,000 R [188].

Under the definition used in that work, this dose results in greater than 95% emergence of adults from the pupal case followed by 50% mortality of adults at 48 hours post eclosion. This description is inconsistent with the results presented here in terms of both emergence and survival of adult flies. It is also inconsistent with other recent works investigating the dose response to 0.662 - 6 MeV x-rays and 225 MeV protons, which found that the doses required to reduce eclosion to 50% was between 40 and 50 Gy [217, 218]. Further, the use of low energy x-rays in this work raises the issue of relative biological effect (RBE). Low energy x-rays have been estimated to cause more biological damage per unit dose compared to standard megavoltage radiotherapy beams (RBE$>$ 1). The dose dependent RBE makes it difficult to directly compare the dose response of the flies in these experiments to other works. It is apparent that the focus on acute endpoints, including lack of mobility in larvae and 48 hour mortality of adult flies, and inconsistency in endpoint definition has created confusion about the radiosensitivy of *D. melanogaster*.

The largest difference in emergence of adult flies was observed at 24 Gy, where UHDR had 68% greater emergence than CONV. This suggests that it may be possible to increase the therapeutic window by using UHDR radiotherapy for some intermediate doses. The reduction in normal tissue toxicities detailed here (eclosion rate and lifespan) are the first prerequisite in demonstrating a FLASH effect induced by low energy x-rays. While the differential effect of UHDR and CONV dose rates on normal tissues is promising, iso-efficacy between UHDR and CONV on tumour tissues must be shown to establish a potential clinical benefit. The availability of *D. melanogaster* tumour models should be exploited for further investigation of a possible FLASH effect.

In addition to differences in survival and lifespan between UHDR and CONV, this work also revealed early signs that the effects of radiation on *D. melanogaster* fertility may be dose rate dependent. While the surviving adults irradiated with UHDR yielded progeny at higher doses (up to 24 Gy) than the corresponding groups irradiated with CONV (up to 22 Gy), this experiment was not designed to provide quantitative fecundity results. Future experiments should isolate irradiated male and female flies and cross them with unirradiated virgin flies.

5.6 Conclusions

D. melanogaster larvae were irradiated with conventional and ultrahigh dose-rate x-rays generated by a shutter controlled 120 kVp x-ray tube. Larvae irradiated with 24 Gy at 210 Gy/s demonstrated 68% higher rates of eclosion compared to larvae irradiated at 0.24 Gy/s. Additionally, flies irradiated with 22 Gy had higher probabilities of survival post irradiation

and longer median survival times, respectively, when irradiated with UHDR compared to CONV. Significant differences in eclosion or lifespan were only observed for flies irradiated with doses between 22 and 26 Gy, suggesting that there is a dose window to observe the FLASH effect in *D. melanogaster*. UHDR irradiation may decrease rates of radiation induced sterility compared to CONV. The similarity of response between CONV-Low and CONV-High treatments suggests that average dose rate may be more important that instantaneous dose rate in triggering normal tissue sparing effects.

Supplementary Information

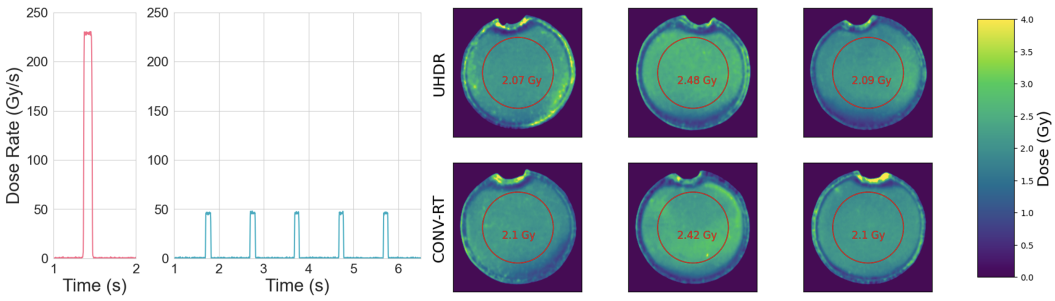

Figure 5.7: Calibrated scintillator measurements of 100 ms irradiations at 25 mA and 5 mA. Film measurements of 50 ms exposures show agreement between UHDR and CONV irradiation modes.

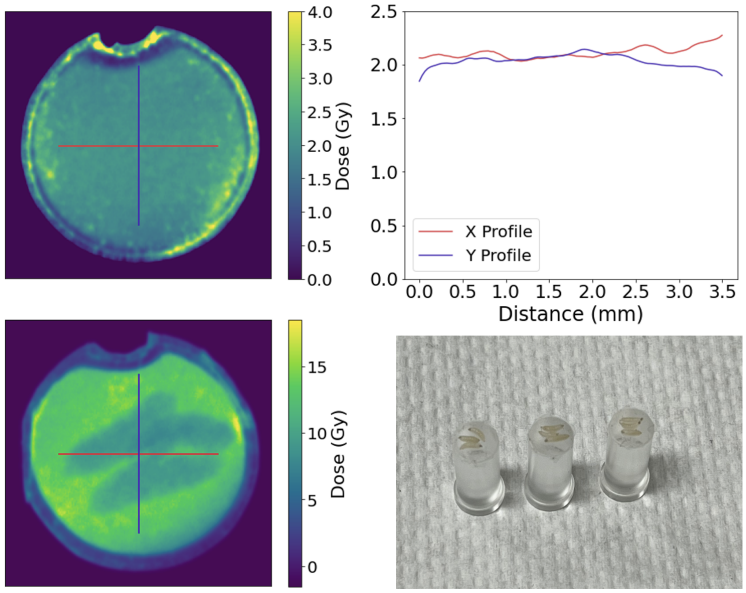

Figure 5.8: Films show a uniform 2D dose distribution is delivered to the surface of the immobilization cylinder and confirm the position of larvae during irradiations. *D. melanogaster* immobilized on acrylic cylinders for irradiation (a). Film placed underneath the larvae confirms larvae positioning during irradiation (b).

Chapter 6

Plastic scintillator dosimetry of ultrahigh dose-rate 200 MeV electrons at CLEAR

The following work was published in IEEE Sensors in 2024 and can be found at the following DOI: 10.1109/JSEN.2024.3353190.

6.1 Summary

Very high energy electron (VHEE) beams with energies greater than 100 MeV may be promising candidates for FLASH radiotherapy due to their favourable dose distributions and accessibility of ultrahigh dose-rates (UHDR). Combining VHEE with the normal tissue-sparing FLASH effect of UHDR radiotherapy could improve patient outcomes. The standard dosimeters used for conventional radiotherapy, including ionization chambers and film, have limited application to UHDR radiotherapy due to deficits in dose rate independence and temporal resolution. Plastic scintillator detectors (PSDs) are a potential alternative. PSDs connected to a Medscint Hyperscint RP-100 were used to measure the response to 200 MeV electrons produced by the CERN Linear Electron Accelerator for Research (CLEAR). The dose-response linearity and radiation hardness of PSDs under UHDR VHEE conditions was investigated, using dose rates up to 1.21×10^9 Gy/s. Two scintillators were investigated: a polystyrene-based BCF-12 and a proprietary polyvinyltoluene (PVT)-based material. The BCF-12 probe exhibited linear light output with dose per train from 4.9 to 125.2 Gy, and dose rates up to 1.16×10^9 Gy/s within a single pulse. The output of the PVT-based probe was linear from 3.9 to 59.5 Gy per train, and dose rates up to 9.92×10^8 Gy/s. While output linearity was retained ($R^2 > 0.998$) after delivering 26.2 and 13.8 kGy to the BCF-12 and PVT-based probe, respectively, the light output was reduced by $< 1.5\%$/kGy. The performance of PSDs in this work suggest they may be useful real-time dosimeters for applications in UHDR VHEE radiotherapy.

6.2 Introduction

Conventional external beam radiation therapy primarily relies on megavoltage x-rays produced by an electron linear accelerator to effectively kill cancerous tissues. Unfortunately, conventional therapies also cause normal tissue toxicities due to shallow dose gradients. Electron beams with energies greater than 100 MeV, very high energy electrons (VHEE), have the potential to improve conformality of radiotherapy treatments due to both their superior dose distributions and deeper penetration [219, 11, 220]. Deep-seated tumours can be targeted with VHEE beams while minimizing the collateral damage to healthy tissues with sharp dose gradients. In addition to the physical dose distribution limitations of conventional radiotherapy, there is a growing understanding that dose rate has a significant effect on the radiobiology of cancer treatment. By delivering radiation doses at ultra-high dose rates (UHDR) in sub second delivery times, it may be possible to give a sufficient dose to tumours while reducing normal tissue toxicities, by means of the so-called FLASH effect[119, 221, 13]. The beam parameters necessary to trigger the FLASH effect are not yet well understood and may depend on the treatment site and particle type, among other factors[222]. While the FLASH effect has been demonstrated with multiple different particle species, electrons may be the simplest to translate into the clinic first for logistics reasons: photon conversion targets suffer from heat-loading and radiation damage [223], while protons and heavy ion facilities are scarce and prohibitively expensive. The first patient to receive FLASH radiotherapy, was treated with electrons[32]. Combining VHEE with the normal tissue-sparing FLASH effect of UHDR radiotherapy could lead to improved outcomes for oncology patients[224].

UHDR VHEE beams present unique challenges in terms of dosimetry, necessitating new tools that provide accurate and real-time measurement. Radiochromic films are useful for their dose rate independence and high spatial resolution but lack temporal information[52]. Ionization chambers, which are current the gold standard for conventional radiation therapy dosimetry, suffer from ion recombination losses which make them ill-suited for UHDR beams[225, 67]. Scintillator detectors, which produce optical photons in response to ionizing radiation, may be an alternative which avoid the previously mentioned problems. Combining fast response times (and the ability for real-time readout), with sub-mm spatial resolution, and dose rate independence for a variety of radiation types and sources [226, 227, 17, 18, 22, 97, 228], radioluminescent detectors are excellent dosimeters for use across the spectrum of dose rates employed in preclinical studies and radiotherapy[229, 230, 231]. There are a wide range of scintillating materials including organic (polystyrene and polyvinyltoluene-based plastics), and inorganic scintillators. Inorganic scintillators can produce a higher yield of optical photons than plastics and are routinely used in imaging applications where maximizing

signal-to-noise is a primary concern[82]. In the context of UHDR beams, the lower signal of plastic scintillators is less relevant and confers the advantage of having similar radiographic properties to human tissue [15]. Scintillators and accompanying light guides can also emit other types of radioluminescence, including fluorescence and Cherenkov light. These other light sources may contaminate the scintillator signal but may be removed if their unique spectral signature is known [93, 105].

Plastic scintillator detectors (PSDs) have proven to be an effective relative dosimeter for many UHDR radiation sources but have never been tested in VHEE beams [16, 100, 85]. In this work, we explored the possibility of using PSDs coupled to an optical spectrum-based scintillation dosimetry platform to perform dosimetry of VHEE beams at the CERN Linear Electron Accelerator for Research (CLEAR). Currently, CLEAR is the only facility capable of producing UHDR VHEE beams up to 200 MeV. The X-band accelerator technology developed for the CLIC (Compact Linear Collider) study and tested at CTF3/CLEAR are also the basis for a prospective UHDR VHEE clinical accelerator [232].

While previous work has shown PSDs to be excellent dosimeters for UHDR protons and low energy x-rays, electron dosimetry with PSDs has only been validated at lower energies and conventional dose rates. Inorganic gadolinium-based scintillator detectors have been used to measure dose delivered by 4.5 MeV electrons produced by the Kinetron (CGR-MeV Co., Buc, France) at dose rates up to 3.5×10^6 Gy/s [226]. PSDs with and without inorganic dopants have been used to measure dose delivered by 250 MeV protons up to 92.5 Gy/s [227], synchrotron x-rays at greater than 4000 Gy/s [17], and 120 kVp x-rays up to 40 Gy/s [18, 22]. The same type of optical spectrum-based scintillator system used in this work was previously used to validate the response of a PSD to 16 MeV electrons at 100 Gy/s [97]. The aim of this work was to expand the application of PSDs to UHDR VHEE beams by investigating the light output linearity with dose and examining the radiation hardness of two different plastic scintillator compositions.

6.3 Materials & Methods

6.3.1 CLEAR Beamline

All measurements presented in this work were acquired using the laser-driven electron accelerator at CLEAR, which produces electron beams with mean energies between 60 and 220 MeV [51]. For the experiments described here a mean energy of 200 MeV with 1% full-width-half-maximum (FWHM) energy beam spread was targeted. The VHEE beams produced at CLEAR have a time structure composed of bunches (groups of electrons 10 ps in length), and trains (groups of bunches at a frequency of 1.5 – 3 GHz, duration from 10 ps to 150

ns). For this study 'train' is synonymous with 'pulse' as it is the shortest resolvable time structure by the PSD system under investigation. The beam parameters used are reported in Table 6.1. Gaussian beams of sizes with $1-\sigma$ greater than the dimension of the active scintillator volume were achieved using quadrupoles and a yttrium aluminum garnet (YAG) scatterer upstream of the vacuum window [34]. An integrating current transformer (ICT) placed immediately after the vacuum window of the beamline allowed for verification of the delivered charge per train. A simplified schematic of the time structure and beamline are shown in Figure 6.1, more detailed descriptions can be found elsewhere [50].

Table 6.1: Summary of beam parameters available at CLEAR.

Beam Energy	60 – 220 MeV
Number of Bunches	1 - 400
Charge per Train	∼20 pC – 85 nC
Bunch Frequency	1.5 – 3.0 GHz
Train Duration	∼10 ps – 150 ns
Repetition Frequency	0.83 Hz - 10 Hz

6.3.2 Plastic Scintillator Dosimetry System

Dose delivered by UHDR VHEE beams produced by the CLEAR beamline was measured with PSDs coupled to a Hyperscint RP-100 optical spectrum-based scintillation dosimetry platform (Medscint, Quebec City), hereafter referred to as a spectrometer, with a 30 meter PMMA optical fiber [96]. Two scintillator compositions were investigated: a standard polystyrene BCF-12 scintillator and a proprietary polyvinyltoluene-based scintillator material (both constructed according to the schematic shown in Figure 6.2). The active scintillator volumes were 0.5 mm diameter and 0.5 mm thick with a manufacturing tolerance of ±10%. The spectrometer was set to an acquisition speed of 5 Hz to allow for continuous real-time measurements (with an integration time of 0.2 seconds). A background was measured (with the same full spectral measurement parameters) for each PSD on each day of experiments. For all PSD measurements, background subtracted signals were normalized to a single PSD reading (one for each PSD probe). The normalized PSD signals are therefore in arbitrary units. No further post-processing (smoothing, filtering, etc.) was applied to the spectral PSD signals before data analysis.

Both scintillator probes and films were positioned in the CLEAR in-air test stand using the C-Robot [233] as shown in Figure 6.3. A 3D-printed holder allowed for the films or scintillators to be kept out of the beam in a lead-shielded staging area until the time of

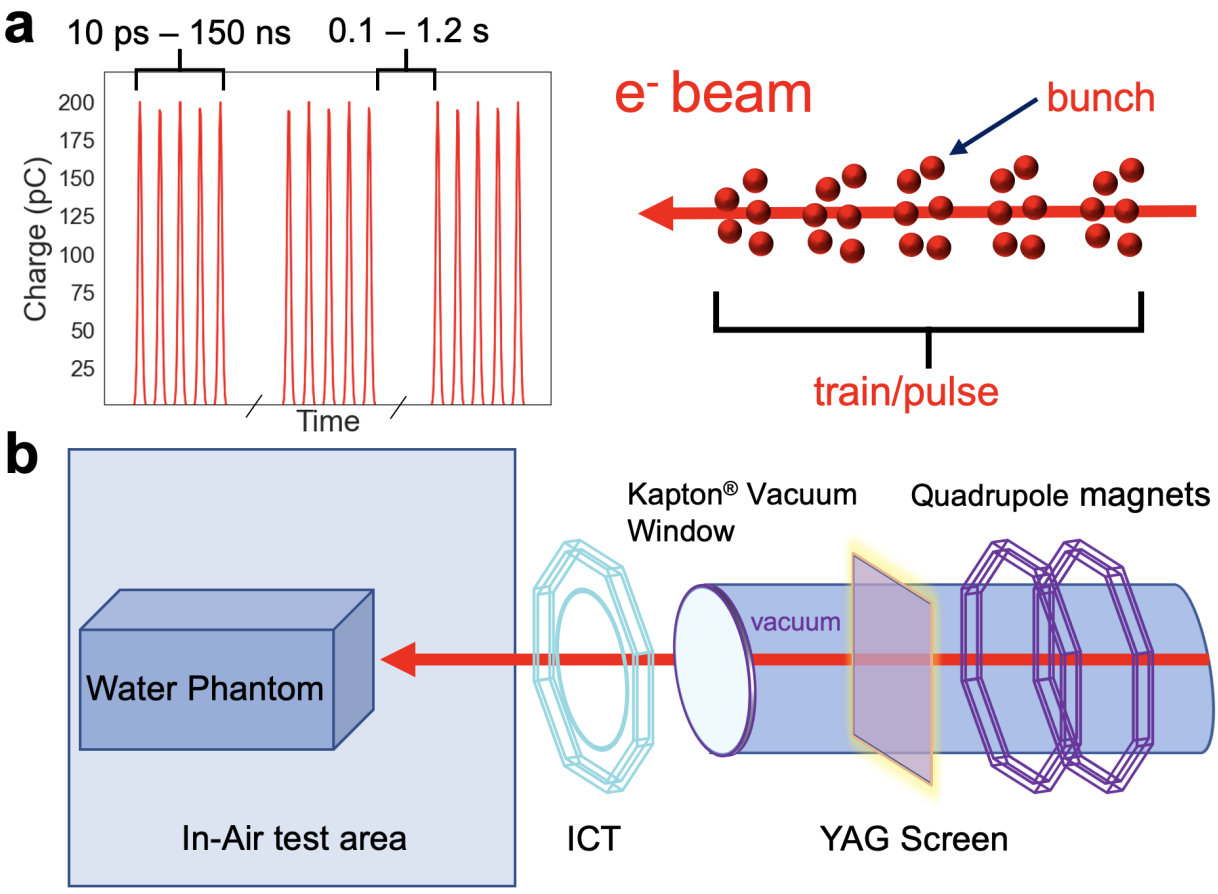

Figure 6.1: Time structure of the laser generated, and RF accelerated electron beam at CLEAR showing trains comprised of ∼200 pC bunches (a). Schematic of the final section of the CLEAR beamline and in-air test stand used for the PSD experiments.

measurement. The holder also featured an yttrium aluminum garnet (YAG) scintillating screen behind the PSD probe. Scintillation light emitted from the YAG screen was reflected upwards by a mirror (positioned behind the YAG screen 45 degrees off-axis to the beam) to a camera, enabling real-time visualization of the beam alignment with the PSD probes.

6.3.3 Film Dosimetry

To obtain dose-to-water calibrations for the scintillators, Gafchromic EBT3 and MDV3 film (Ashland, NJ) measurements were conducted under the same beam conditions as scintillator measurements. Dose-to-water film calibrations were obtained using a 5.5 MeV electron beam at 0.05 Gy/s produced by an eRT6 Oriatron. EBT3 film has previously been shown to be dose rate independent for electron beams up to 8×10^6 Gy/s [200] and energy independent up to 165 MeV[57]. Film measurements were used to calculate the doses delivered to the

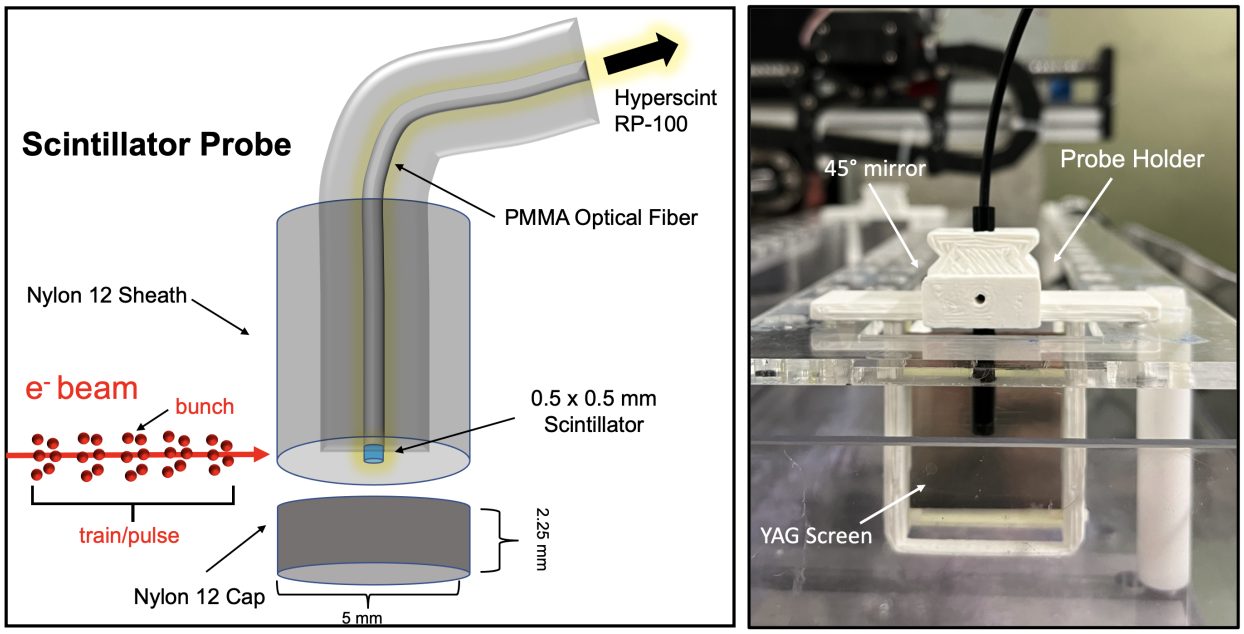

Figure 6.2: Schematic and photograph of PSD probe and 3D-printed holder. Scintillation light from the yttrium aluminum garnet (YAG) screen is reflected by the mirror upwards towards a camera. The structure of a single train is shown, composed of several bunches. The number and charge of bunches can be scaled to vary the charge (and therefore dose) per train.

scintillator probes (as absorbed dose-to-water, D_W) for both output linearity and radiation damage measurements. Film measurements were also used to convert ICT readings from charge per train to absorbed dose. The films were scanned 24 hours post irradiation using an Epson Perfection V800 Photo scanner (Epson, Long Beach, CA) at 300 DPI. Pixel values from the green channel were converted to dose-to-water and background corrected with unirradiated films. For determining dose to the scintillator probes from the film, a 10×10 convolutional (0.85×0.85 mm) kernel was used to smooth the dose map and the mean of the three highest pixel values was taken as the film dose. This kernel size was chosen to cover the active scintillator volume and to account for minor misalignment with the central axis of the beam. The beam sizes were determined by fitting Gaussian curves to the x and y profiles intersecting the maximum dose point.

6.3.4 Output Linearity

Output linearity measurements were conducted by scaling the dose per train between 4 and 160 Gy. To achieve this, the number of bunches and charges per bunch were adjusted to deliver charges per train up to ~70 nC, and dose rates up to 1.2×10^9 Gy/s, as detailed in Table 6.2. Dose rate was calculated by normalizing the delivered dose by the train length

(which varies depending on the total charge delivered and the number of bunches required). All doses were delivered in a single train and thus average dose rate (dose normalized by total delivery time) and instantaneous dose rate (dose per train normalized by train length) are equivalent for the purpose of this work. For characterizing PSDs as a VHEE dosimeter under conventional radiotherapy dose rates (i.e. 0.1 Gy/s over the duration of the treatment time) it may become necessary to distinguish average dose rate from instantaneous, train, or even bunch dose rate. Because varying the number of bunches and charge per bunch can alter the optics of the beam, the YAG screen was used to verify the positioning of the beam with respect to the central axis of the active scintillator volume for each measurement. Three single trains were delivered to the scintillator probes per dose point to allow calculation of a mean and standard deviation of the response. Scintillator signals were analyzed by integrating the background subtracted light output. To obtain dose-to-water calibrations for the PSDs, the delivered ICT readings (in nC) were first converted to dose according to

$$D_W = ICT \times k_f \tag{6.1}$$

where k_f is the dose/charge (Gy/nC) calculated using films. Values of k_f were determined for each day of experiments to control for varying beam sizes. Then, a linear fit was applied between the PSD output and D_W such that

$$PSD = D_W k_S \tag{6.2}$$

where k_S is the slope of the fit, a correction factor dependent on the PSD and the gain setting of the spectrometer. Signal-to noise ratio (SNR) was also calculated from the same data set according to:

$$SNR = \mu_s/\sigma_b \tag{6.3}$$

where μ_s is the integrated light output from the spectra, and σ_b is the standard deviation of the background spectral signal (wavelength range 0 to 10 in arbitrary units which does not contribute to the scintillation light). Additionally, the spectral output from each dose was examined to determine if radiation damage had caused any changes in optical properties. All data analysis was conducted in Python 3.10 using the SciPy scientific library [234].

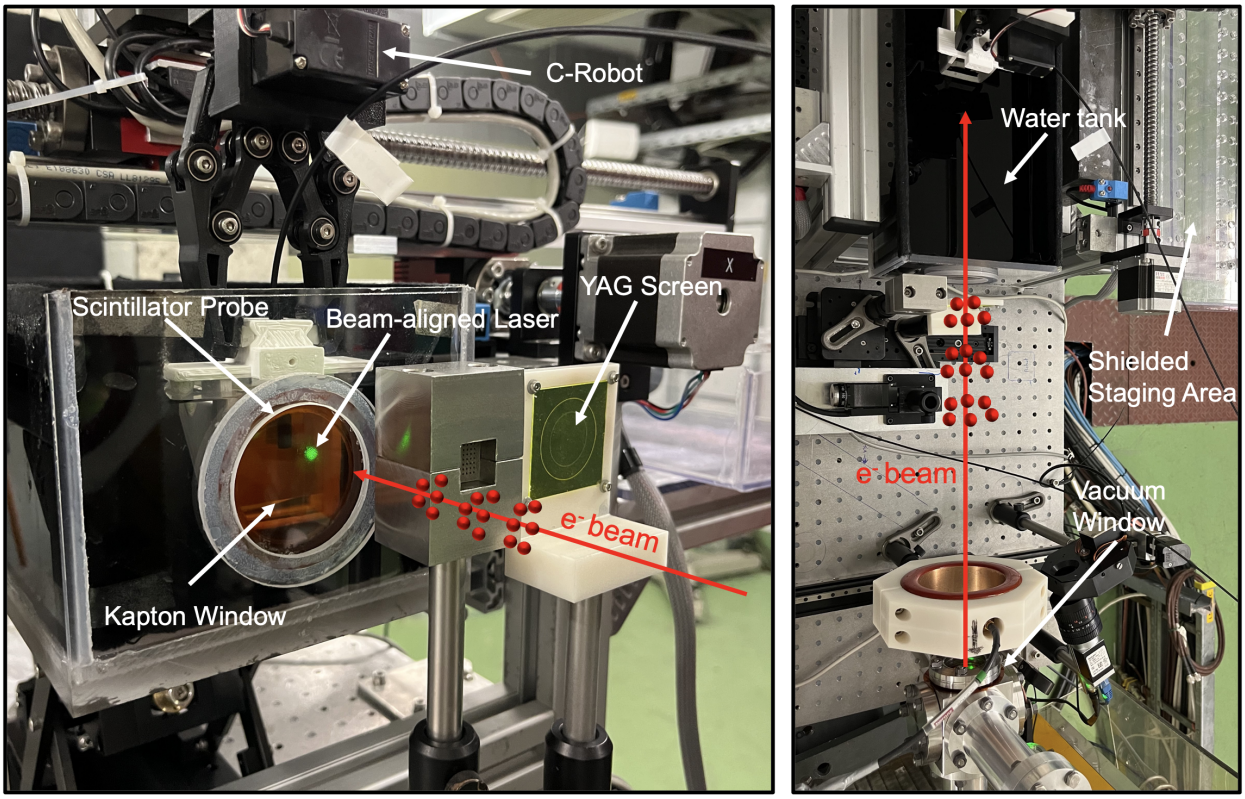

Figure 6.3: The PSD setup within the water tank relative to electron beam. The C-Robot moves samples (films or PSD probes) from the shielded area to a user-defined location in the beam path. The YAG screens allow for verification of the transverse beam size and position before delivering dose to samples.

Table 6.2: Targeted beam parameters used for output linearity measurements shown in Figure 6.5.*The factor used to calculate the target dose per train values shown (2.31 Gy/nC for BCF-12 measurements) was taken from the film shown in Figure 6.4b. For doses to the PVT+ probe, a separate factor was calculated from the film in Figure 6.4e. The reported dose rate is for the duration of the train. †When targeting 70 nC/train, a scattering YAG screen was placed upstream of the vacuum window, which may have increased the beam size. The mean energy also decreased to 185 MeV.

charge/train (nC)	dose/train (Gy)*	# of bunches	charge/bunch (nC)	bunch frequency (GHz)	train duration (ns)	dose rate (Gy/s)
2	4.6	12	0.167	1.5	8	5.78E+08
9	20.8	55	0.164	1.5	37	5.67E+08
30	69.3	180	0.167	3	60	1.16E+09
50	115.5	386	0.130	3	129	8.98E+08
55	127.1	400	0.138	3	133	9.53E+08
70†	161.7	400	0.175	3	133	1.21E+09

6.3.5 Radiation Damage

The PSDs used in this work had been exposed to negligible amounts of dose prior to experiments at CLEAR. Radiation hardness was assessed by recording the delivered charges (ICT readings) to each of the probes during all measurements. When positioning the beam on the PSDs, the charge received (and indirectly, dose) was recorded. The probes were also exposed to large cumulative doses of radiation, 26.2 and 13.8 kGy for the BCF-12 and PVT-based probes, respectively, in ∼3 kGy increments. Limited beam time availability prevented delivering the same total doses to both probes. For these irradiations the beam was operated at a train repetition frequency of 0.83 Hz, with 9-10 nC per train, until reaching a total delivered charge of 1250 nC. The output reduction over the course of these irradiations was assessed by comparing the mean signal from 9 nC trains before and after each ∼3 kGy dose. The mean reading from five trains was averaged to account for normal fluctuation in the beam output. Output linearity measurements (three single trains with 2 to 30 nC/train) were conducted before and after these damaging doses to monitor changes in the performance of the probes. By normalizing to the slope of the initial output linearity measurement (as in Figure 6.7), the decrease in output as a function of radiation damage was observed. Time between measurements when the PSD probes were not being irradiated (during beam diagnostics tests or film measurements) allowed for testing the recovery of the scintillators. Limited beam time made it impractical to conduct a systematic study of scintillator recovery at CLEAR.

6.4 Results

Figure 6.4 shows the response of both PSD probes and films to 200 MeV electrons at CLEAR. Figure 6.4b and e show that dose per train decreases from 2.31 to 1.97 Gy/nC when beam size increases from 3.7×3.8mm to 4.0×4.4mm ($1-\sigma$). These dose/charge factors were used for calculation of dose-to-water absorbed by the BCF-12 and PVT-based probes, respectively, shown in Figures 6.5 and 6.7.

6.4.1 Output linearity

Output linearity with charge per train for both scintillators is shown in Figure 6.5a and c. The targeted dose rates are shown in Table 6.2, which range from $5.67-12.1\times10^{8}$ Gy/s. The BCF-12 probe exhibited linear light output with dose per train from 4.9 to 125.2 Gy (2.1 to 54.2 nC). At higher doses per train the probe failed to respond linearly, yielding a lower light output than at lower doses per train. The PVT-based probe saturated at lower doses than the BCF-12, showing linearity from 3.9 to 59.5 Gy (2 to 30.2 nC). The scintillator spectra from linearity measurements are reported in Figure 6.5b and d. The lowest and highest

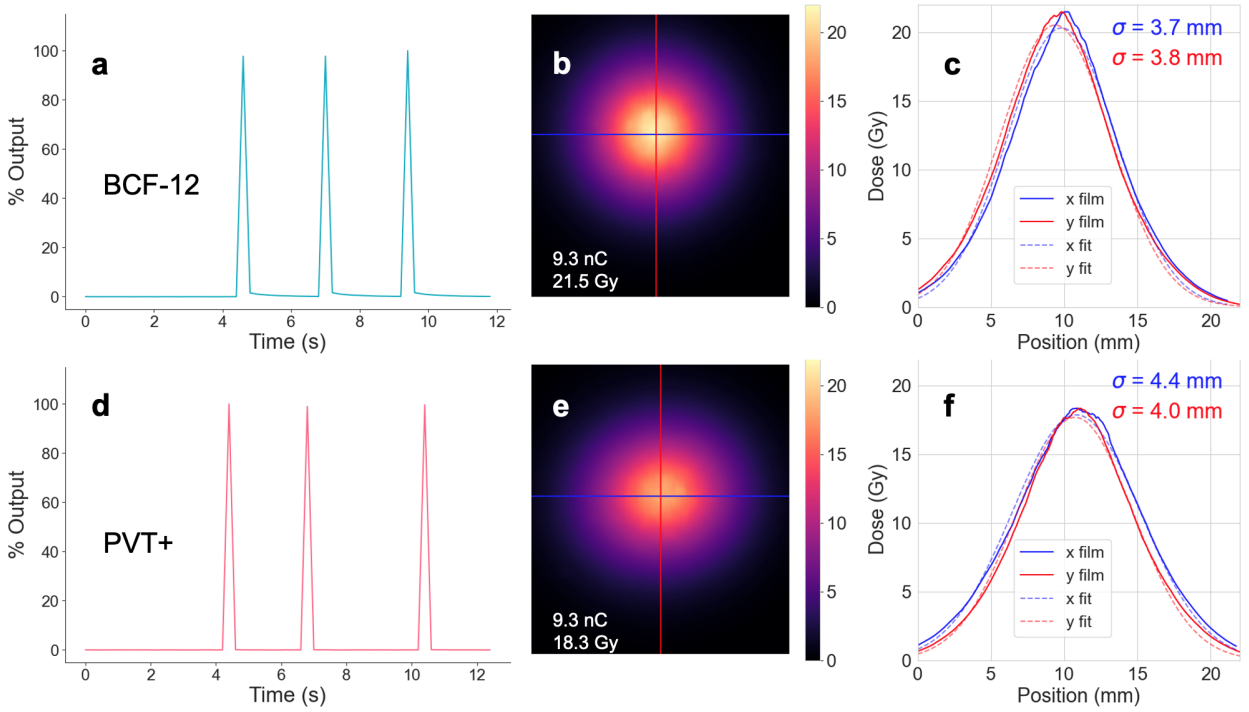

Figure 6.4: Film and PSD measurements of dose delivered by 200 MeV electrons under the same beam conditions for BCF-12 (a-c), and the PVT-based PSD (d-f). Integrated light output from three trains is shown for both PSD compositions (a,d). PSD signals are normalized to maximum frame for each measurement for display only. The larger beam in e corresponds to a lower dose per charge compared to the beam shown in b.

charge in the linear regime, as well as the saturating charges are shown to highlight any spectral changes that may have occurred due to transient radiation damage. The normalized spectra from both scintillator compositions remains nearly constant. No significant shift of the peak wavelength was observed. In addition to showing output linearity with dose per train, both PSD probes exhibited excellent output reproducibility. The mean of the standard deviations for all measurements shown in Figure 6.5 was 2.39% for BCF-12 and 2.36% for the PVT-based probe.

The SNR values for both PSDs are reported in Table 6.3. SNR increased with charge per train except in the case of 68.2 nC delivered to BCF-12 in which case the output was also reduced compared to lower charges per train.

6.4.2 Radiation Damage

The PSD response to irradiations at a repetition rate of 0.83 Hz is shown in Figure 6.6. After receiving 2.89 and 2.45 kGy, the output of the PSDs decreased by 3.47% and 6.04% for the BCF-12 and PVT-based probes, respectively. Output linearity was retained for both probes

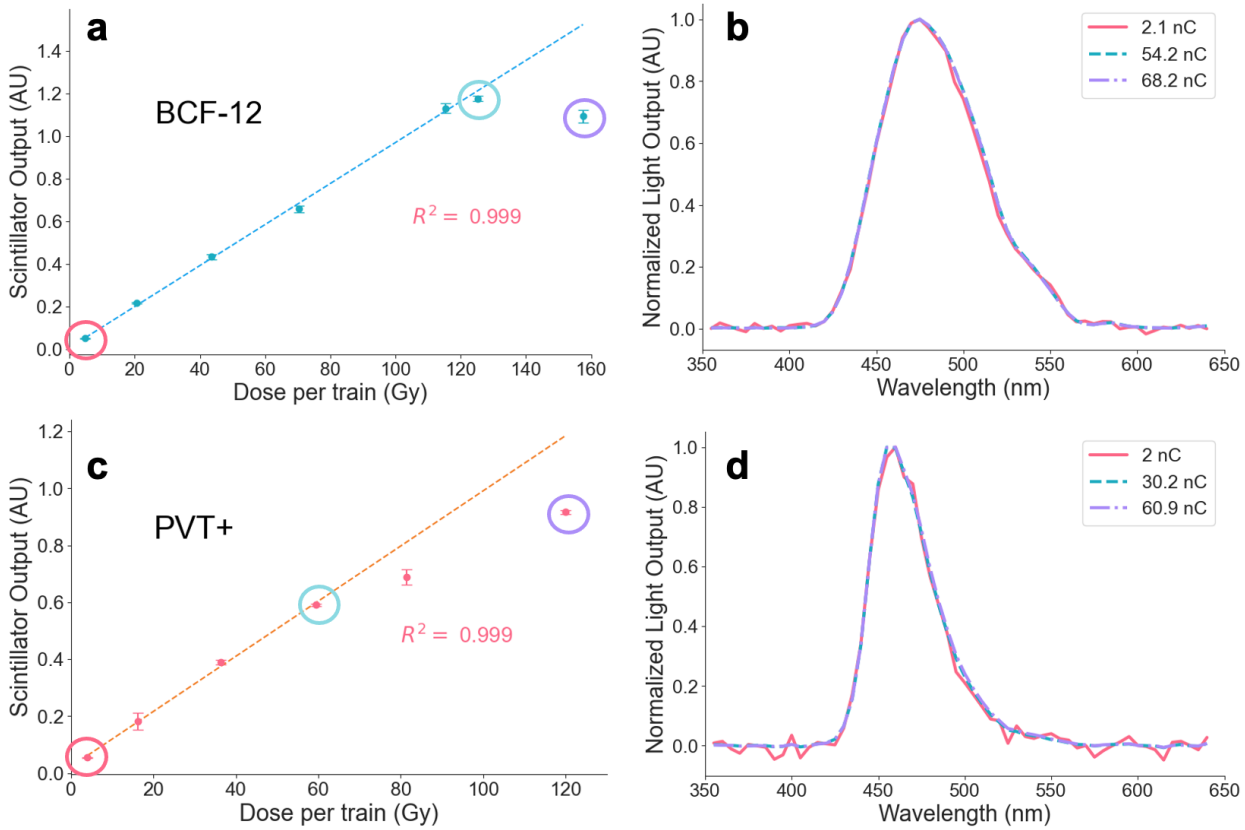

Figure 6.5: Output linearity as a function of dose-to-water and corresponding spectra for BCF-12 (a,b) and PVT-based (c,d) PSDs. The circled output values in a and c represent the response to the lowest charge, highest linear response, and the saturating signal. The spectra are normalized to the peak intensity for each measurement.

Table 6.3: SNR for both scintillator compositions calculated from the output linearity data shown in Figure 6.5 for both scintillator compositions.

BCF-12		**PVT+**	
charge (nC)	**SNR**	**charge (nC)**	**SNR**
2.1	1583.4	2	400.9
8.9	4478.3	8.2	1210.6
18.9	8772.7	18.4	2079.8
30.5	18570.8	30.2	3854.3
50	56621.0	41.3	4524.6
54.2	26650.5	60.9	4624.3
68.2	24209.2	-	-

($R^2 > 0.99$) after delivering total accumulated doses of 26.2 and 13.8 kGy to the BCF-12 and PVT-based probes. However, the light output (the slope of the fit from equation 6.2) was

reduced in both cases. For example, the slope of the output linearity for BCF-12 decreased by 10% from 0.015 to 0.0135 when the total received dose increased from 4.6 to 10.1 kGy as shown in Figure 6.7. The output of the BCF-12 scintillator decreased by 1.21%/kGy while the PVT-based PSD output decreased by 1.51%/kGy. Between the third and fourth BCF-12 linearity measurements (corresponding to ∼18 kGy total delivered dose), the PSD was allowed 15 minutes to recover. The BCF-12 recovered to 99.6% of the linearity slope at 10.1 kGy. Between the final two BCF-12 output linearity measurements, ∼8 kGy was delivered (9 nC at 0.83 Hz) followed by 17 hours without any irradiation. No recovery was observed in the output of the PSD after this rest interval.

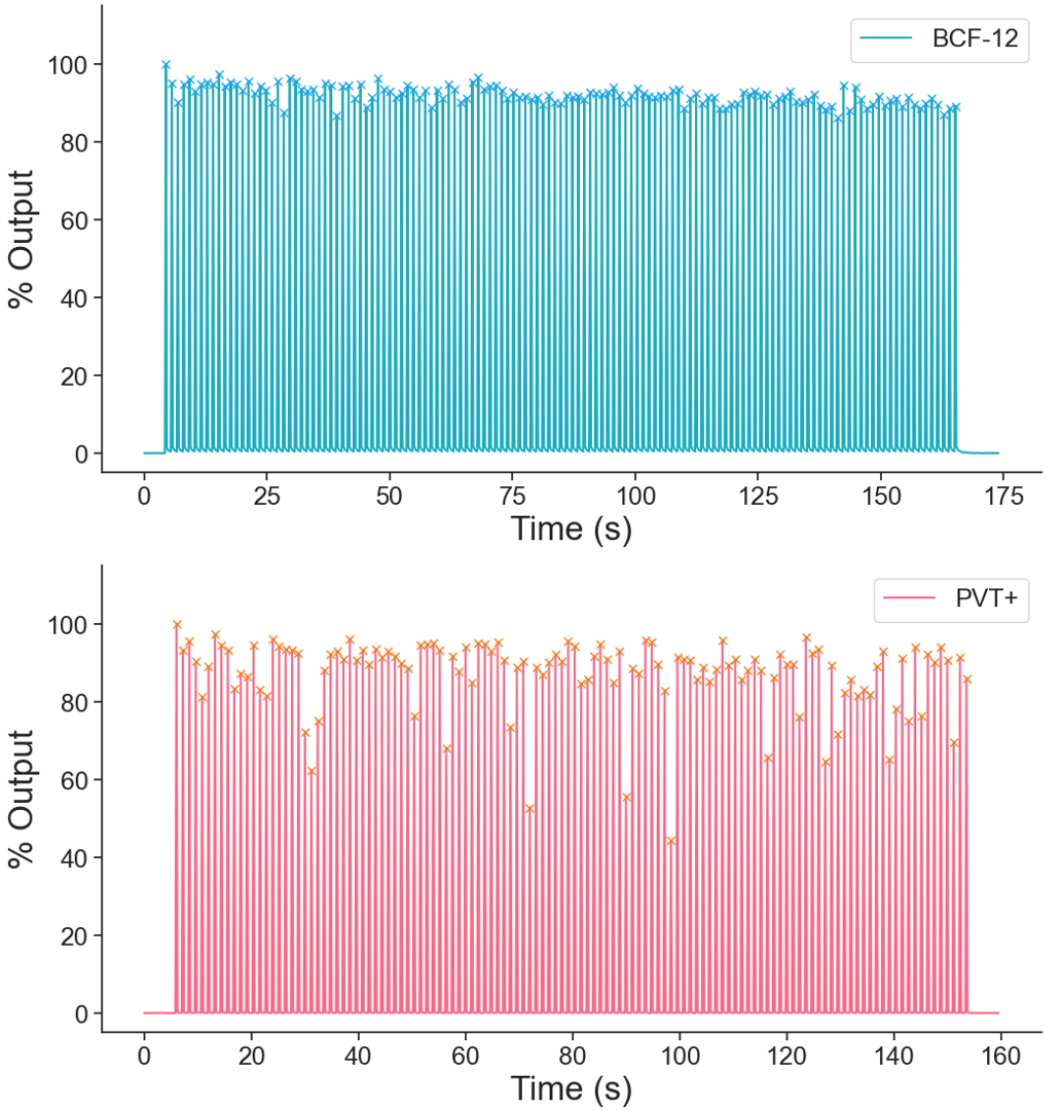

Figure 6.6: The irradiations delivered in ∼3 kGy doses to BCF-12 and PVT-based probes to assess radiation damage. Scintillator response decreased by 3.47% and 6.04% over the duration of the irradiations shown for the BCF-12 and PVT-based probes, respectively.

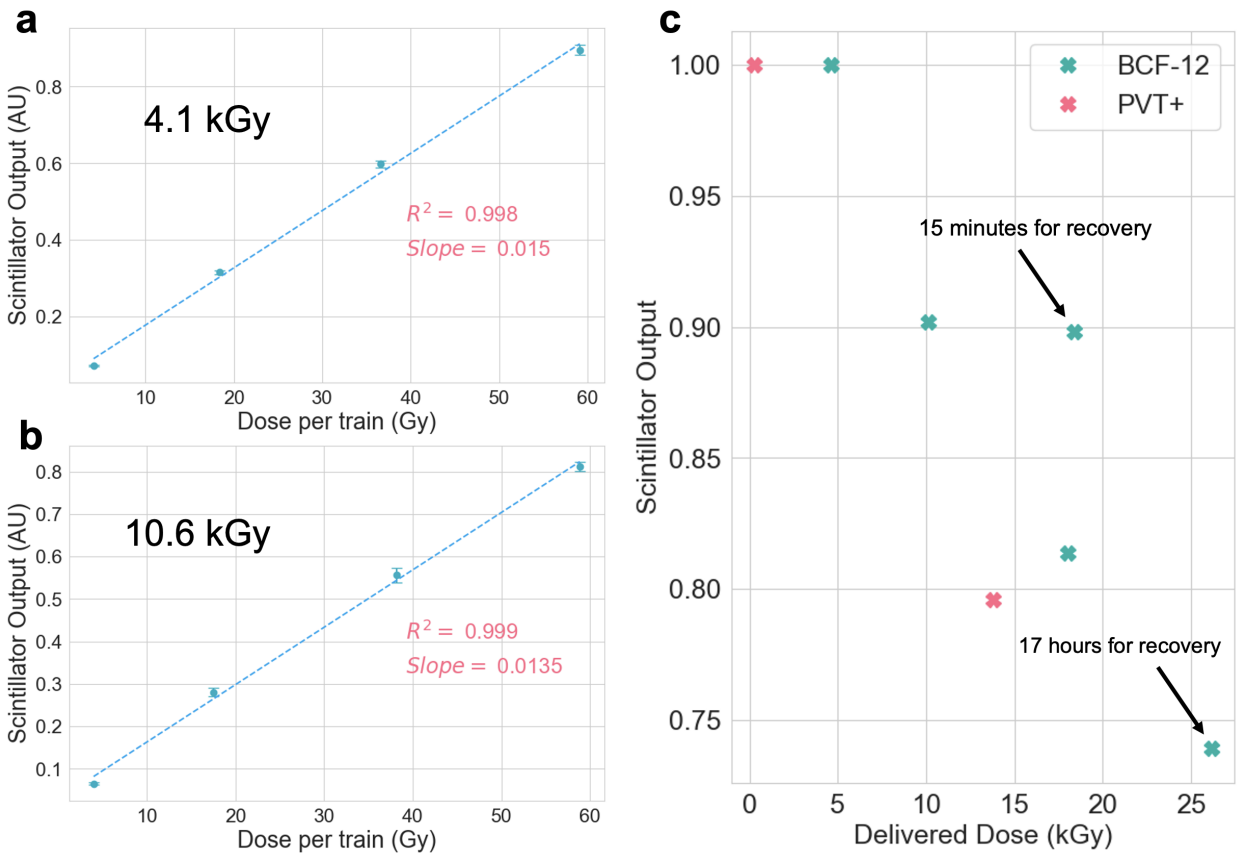

Figure 6.7: The output linearity measurements for BCF-12 are shown with 5.5 kGy delivered between (a,b). The slope of the output linearity measurements was used to determine the reduction in output as a function of total accumulated dose (c).

6.5 Discussion

One of the most important attributes of a dosimeter is the ability to respond linearly with dose irrespective of dose rate within ranges relevant to clinical use. For FLASH radiotherapy, it can be expected that single fraction treatments and dose escalation will require dosimeters capable of measuring higher doses than those used for conventional radiotherapy. To date, FLASH radiotherapy has been delivered to patients under two prescriptive regimens: 8 Gy with 250 MeV protons in the FAST-01 trial [134] and 15 Gy with 5.6 MeV electrons [32], both in a single fraction. Some proposed VHEE plans have included prescription doses of 36.2 Gy to the planning treatment volume (PTV)[11]. Both PSD probes investigated in this work demonstrated high degrees of output linearity (>0.998) with dose at UHDR, which would make them suitable dosimeters for verifying delivery of large doses in a single fraction. It should be noted that the investigation presented here only included dose rates which can be considered UHDR. Other work has found that inorganic scintillators exhibit linearity at both

conventional and UHDR with 9 MeV electron beams, but required independent calibrations for each dose rate regime [235]. Although both PSDs showed excellent linearity with large doses delivered in a single train, accumulated doses on the order of kGy caused reduction in scintillator light output. The output of both probes decreased by ∼1.2-1.5%/kGy, which means routine recalibration would be required to enable accurate dosimetry for radiotherapy.

When the PSDs failed to respond linearly with dose per train, review of the scintillator spectra before and after saturation helped to eliminate the spectrometer as the source of signal saturation as seen in Figure 6.5 (we would expect to see a flattened spectrum if the spectrometer was saturating). The source of the saturation cannot be definitively isolated as either accumulated dose or dose rate because the dose rate was not constant with dose per train (as reported in Table 6.2). The lack of shift in the spectra during output linearity measurements (∼400 Gy per output linearity set) may indicate that the probes could be recalibrated after being damaged by simply scaling the slope of the calibration curve. Further experiments are needed to determine if any damage-induced wavelength shifts occur in the active scintillator volume or the irradiated stem over time.

Cherenkov light produced within the scintillator volume, and the PMMA optical fiber can significantly contribute to the integrated light signal [236]. For the experiments presented here, stem-from-subtraction measurements were acquired with the beam on the optical fiber, and off-axis, to minimize scintillation light signal. After reviewing the spectra from these measurements, it was determined that applying corrections was unnecessary. Additionally, the small transverse beam sizes as well as the perpendicular orientation of the probe and fiber with respect to the beam helped to mitigate the contribution of Cherenkov light. Measurements with a clear optical fiber (without active scintillator material) in addition to BCF-12 and PVT+ scintillators in a single probe allowed for an estimation of the Cherenkov contribution to the total light signal. The average contribution was 13.7% for BCF-12 and 17.2% for PVT+. While this is non-negligible, it did not alter the linearity of the total integrated signal. Future experiments using this combined probe design will enable a more thorough investigation of the impact of Cherenkov light and may allow for spectral subtraction of the Cherenkov signal from every PSD measurement.

An unexpected signal was observed from the BCF-12 probe in the frames immediately following the scintillation response as shown in Figure 6.8. With frame durations of 0.2 seconds, there should not be any scintillation light remaining in subsequent frames. The light output from the next frame shows that the spectrum is shifted towards higher wavelengths. This phenomenon is notably absent from the PVT+ data. The spectral shift and time delay of this signal may indicate that the PMMA cladding (which is unique to the BCF-12 probe design) is an additional source of radioluminescence. The source and conditions necessary

to produce this secondary signal should be investigated in future work.

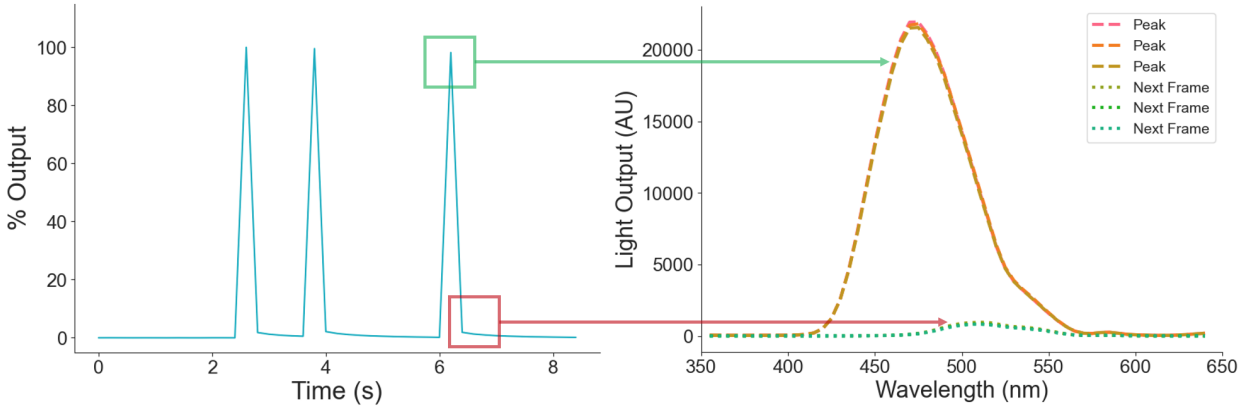

Figure 6.8: Spectral output from BCF-12 in response to 54.2 nC delivered in 3 separate trains for output linearity measurements. The frames following each peak signal show a shift to higher wavelengths.

An advantage of PSDs is that their high spatial resolution allows for measurement of steep dose gradients[16]. While the spatial resolution of the PSDs used in this work was limited by their 0.5 mm dimensions, the measured SNR values far exceeded the recommendation of the Rose criterion (see Table 6.3). This suggests that smaller scintillators with higher spatial resolution could be used without producing excessively noisy signals. Future testing of spatial resolution and output linearity of smaller scintillator detectors may help to identify a more appropriate detector design.

6.5.1 Radiation Damage

The two PSD compositions used in this work showed excellent radiation hardness, with output decreasing by less than 1.5%/kGy when irradiated with 200 MeV electrons at UHDR. This compares favorably with other investigations of PSDs under lower energies and dose rates which showed reduction in scintillator output as high as 16%/kGy [203, 237]. In addition, the BCF-12 probe was shown to recover from radiation damage in one case, when left unirradiated for 15 minutes between measurements. However, after 17 hours of recovery time the final output linearity test did not result in any significant recovery of light output. This demonstrates that UHDR VHEE damage up to 18 kGy may be at least temporarily recoverable but could become permanent at higher doses. Further investigation of the irradiated probes would be necessary to quantify the potential for PSD recovery as a function of time and lifetime accumulated dose. Previous work has shown pure polystyrene PSDs to recover from 50% reduction in output after 10 kGy doses to less than 10% output loss after more than 500 hours [203].

6.5.2 Limitations

This work has explored the possibility of using PSDs and the Hyperscint RP-100 spectrometer as a combined system for dosimetry of UHDR VHEE beams. Two limitations of the Hyperscint RP-100 were encountered in this work: the saturation of the photodetector array at high gain settings, and the maximum frame rate resulting in insufficient temporal resolution. The dose calibration obtained for each PSD is dependent on the gain setting of the system. An investigation of the relationship between gain and scintillator output may allow for gain adjustments to be made without recalibration and could increase the linear range in terms of doses and dose rates for a given PSD. The temporal resolution in this work was limited by the maximum frame rate of 5 Hz which the Hyperscint RP-100 can stream continuous measurements, 5 Hz. Higher frame rates (up to 400 Hz) are possible, but do not allow for real-time visualization, and thus immediate verification of beam delivery. Other preclinical scintillator systems have achieved higher acquisition speeds on the order of nanoseconds, however these do not capture the full spectral information [111]. Recent work has emphasized that the FLASH effect has a nuanced relationship with the time structure of irradiation. It may not simply depend on a threshold average or instantaneous dose rate but could also be influenced by the micro structure of the beam, i.e. the bunch frequency and inter-train spacing [117]. While the spectrometer used here could resolve individual trains in real time, having sub-train temporal resolution would be useful for both beam diagnostics and radiobiological FLASH studies. CLEAR is an experimental beamline and has increased uncertainty in dose delivery compared to the commercially available linear accelerators used in clinics. Examples of aberrant signals and their possible causes are shown in Figure 6.9.

PSD experimental uncertainties are a combination of beam operation uncertainties and film dose calibration uncertainties. As previously mentioned, the absorbed dose reported in this work was determined using EBT3 films calibrated with 5.5 MeV electrons, which can be expected to add an uncertainty of ∼5% for use with 200 MeV electrons [57]. Further, the response of PSDs is expected to be independent of energy over this range as the variance in collisional mass stopping power ratio for water to polystyrene is under 0.5% as shown in Figure 6.10.

As shown in the beam profiles in Figure 6.4, CLEAR produces small Gaussian fields which can easily be misaligned with the active scintillator volumes used in this study. The beam was frequently re-positioned visually using the shadow of the PSD probes on the YAG screen to mitigate beam positioning as a source of error. Future work with a flattening filter in the beam path could help to further reduce uncertainty. It is also possible that operating parameters, such as the repetition rate, impact the stability of the beam. For example, when trains were delivered at 10 Hz (as shown in Figure 6.6) there was greater

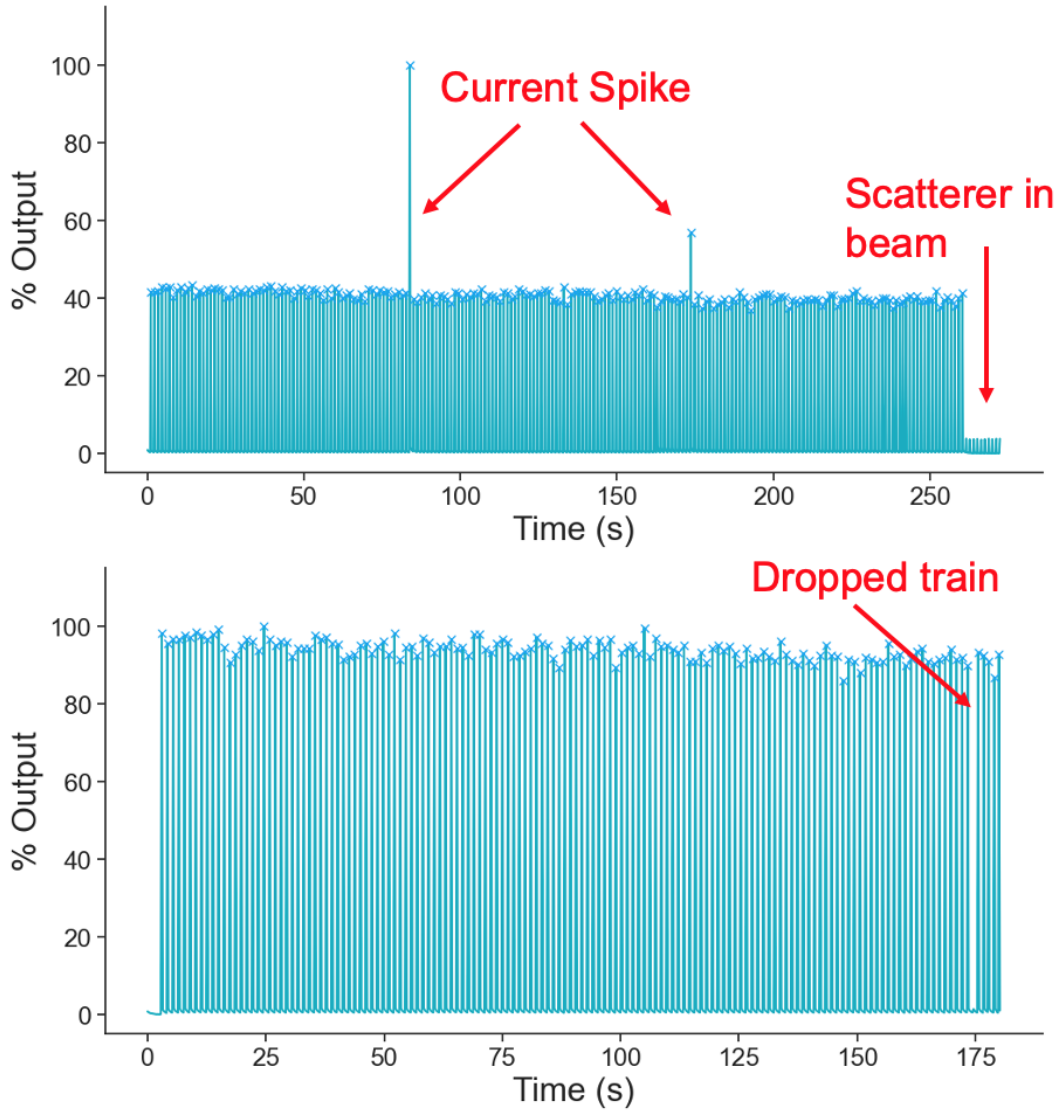

Figure 6.9: Examples of PSD signals which can be explained by malfunctions in the CLEAR beamline. The most likely cause of these fluctuations in dose rate are due to laser breakdowns causing trains with either very high or very low charge. This is not uncommon towards the end of the operation year where the laser may lose synchronization and the photocathode is at less than optimal condition.

variation in the measured output per train than the ∼2.4% associated with the output linearity measurements which were delivered without a set repetition frequency.

6.6 Conclusions

Electron radiation may be the modality best positioned to facilitate the clinical translation of FLASH radiotherapy. By combining the radiobiological benefits of UHDR radiotherapy

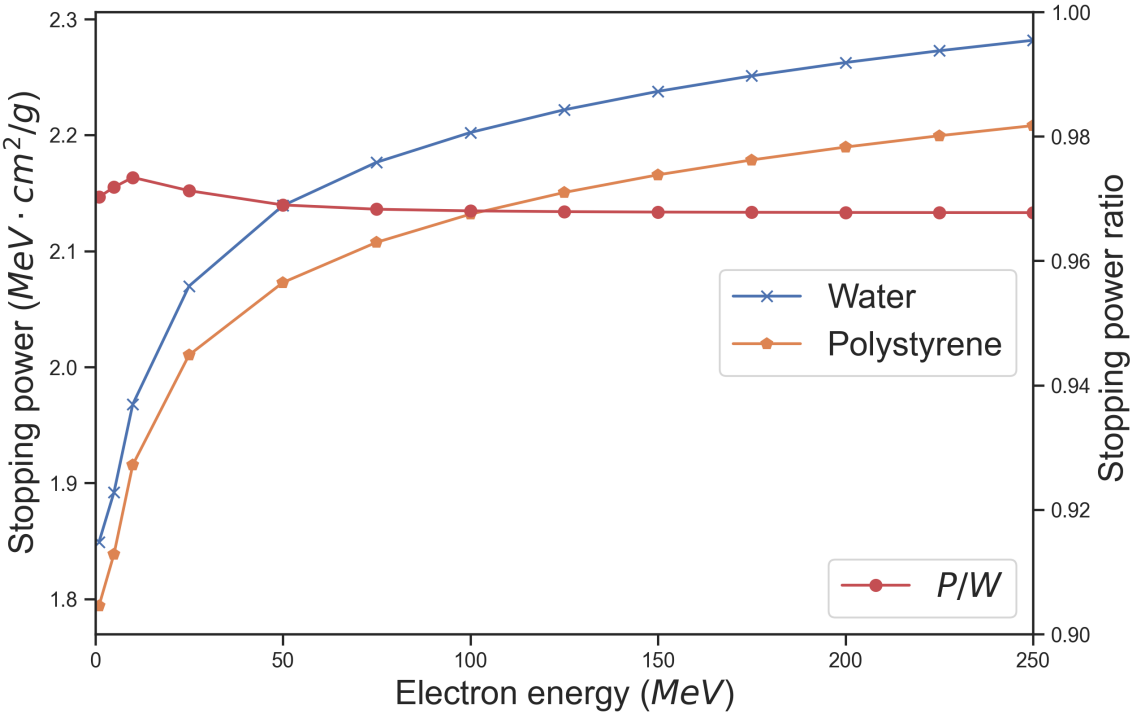

Figure 6.10: Collisional mass stopping power for water and polystyrene over the range of electron energies produced at CLEAR. The stopping power ratio for water to polystyrene varies by less than 0.5% from 1 to 250 MeV.

with the advantageous physical dose distribution of very high energy electron beams, cancer treatment could cause less collateral damage to healthy tissues and become more effective. To move towards clinical translation, it is essential to develop accurate dosimeters exhibiting dose rate independence and sufficient radiation hardness. To this end, plastic scintillator detectors were tested with the 200 MeV beam with dose rates up to 1.21×10^9 Gy/s at CLEAR. We have demonstrated that polystyrene and polyvinyltoluene-based PSDs respond linearly with dose per train up to 59.5 and 125.2 Gy, respectively. These doses exceed what we would expect to be given in a single therapeutic dose, which suggests that PSDs could accurately verify dose delivery during VHEE FLASH radiotherapy treatments. In addition, we found that while the output of PSDs is reduced by radiation damage, PSDs retain output linearity after receiving high accumulated doses of radiation, allowing them to be recalibrated for further use.

6.7 Supplementary Materials

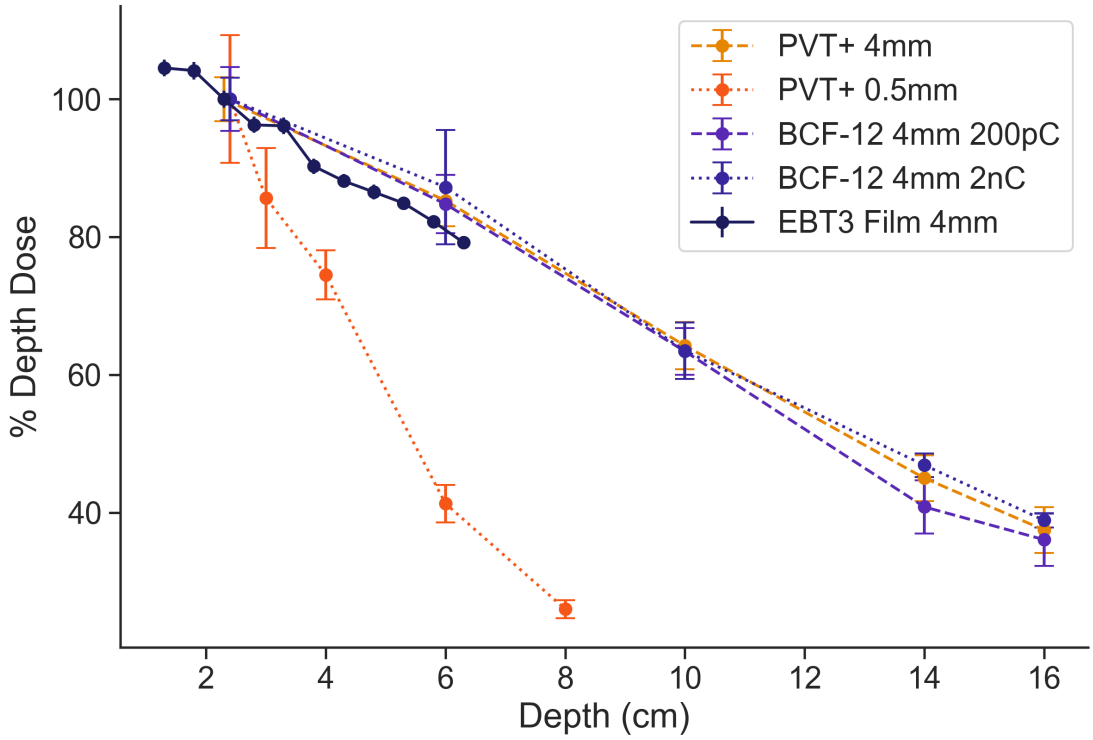

Figure 6.11: Percent depth dose (PDD) measured with both PSDs compared with film measurements. Transverse beam sizes of 4mm $1-\sigma$ were used except for one set of PVT+ measurements acquired with a 0.5mm $1-\sigma$ pencil beam. BCF-12 data was measured by delivering 2 nC in a single train or in ten 200 pC trains, all other data was delivered as a single 2 nC train. The C-Robot was used to acquire step-and-shoot PDD measurements at different longitudinal positions in the water tank.

Chapter 7

First *in vivo* determination of the relative biological effectiveness of very high energy electrons using *Drosophila melanogaster* irradiated at conventional and ultrahigh dose-rates

The following work is being prepared for manuscript submission to Scientific Reports.

7.1 Summary

Very high energy electrons (VHEE) may be able to facilitate FLASH radiotherapy of deep-seated tumours due to their physical dose distribution. To investigate the radiobiological effects of VHEE at conventional and ultrahigh dose-rates (UHDR), *Drosophila melanogaster* larvae were irradiated with 200 MeV VHEEs and 9-20 MeV energy electrons. White-eyed *D. melanogaster* (w^{1118}) larvae were irradiated to doses between 15 and 45 Gy with 200 MeV electrons using the CLEAR beamline at both UHDR ($\sim 3 \times 10^8$ Gy/s) and conventional dose-rates (CDR, 0.2 Gy/s). Larvae were also irradiated with 9-20 MeV electrons produced by a Varian TrueBeam at dose-rates of 0.2 and 130 Gy/s. Flies were monitored through development, including qPCR analysis and eclosion of adults post irradiation. Percent eclosion was calculated by normalizing to the number of pupae and the eclosion rate for unirradiated controls. The dose yielding 50% eclosion, ED_{50}, was used to determine the relative biological effectiveness (RBE) of VHEE compared to CDR 9-20 MeV electrons. Flies irradiated with UHDR VHEE eclosed at higher rates than those treated with CDR VHEE resulting in ED_{50} values of 37.4 and 35.1 Gy, respectively. Irradiations with clinically used electron beams at CDR yielded very similar dose response curves, with ED_{50} values of of 35.3 Gy for 9 MeV, and 34.6 Gy for 20 MeV. This first *in vivo* confirmation that the RBE of VHEE is near unity may be useful in predicting the efficacy of VHEE beams for cancer treatment.

Introduction

External beam radiation therapy using megavoltage x-rays is an effective and widespread treatment for many cancers. These beams are produced by electron linear accelerators with energies up to 20 MeV using transmission targets to create bremsstrahlung x-rays. Electron beams produced by the same linear accelerators are also used for cancer treatment directly, but are limited to treatments of shallow lesions due to their physical dose distributions. Recently, interest has grown in using electrons with energies greater than 100 MeV, so-called very high energy electrons (VHEE), to target deep-seated tumours [219, 11, 238, 239]. VHEE beams have been shown to penetrate deeper into tissue than conventional x-ray or electron beams, providing dose distributions more similar to heavy-ion beams while being less susceptible to range uncertainties caused by inhomogeneities in tissue density [35]. Accelerators capable of producing VHEE beams could do so at ultrahigh dose-rates (UHDR) [240, 51, 23], which have the potential of sparing damage to normal tissues surrounding a tumour while effectively controlling cancer growth, known as the FLASH effect [13, 139]. UHDR radiotherapy is characterized by a time structure in which the treatment dose is delivered ∼1000 times faster than conventional dose-rate radiotherapy (CDR-RT).

The scarcity of VHEE capable beam lines has relegated nearly all studies of their application in radiotherapy to the simulation space [11, 241]. The CERN linear electron accelerator for research (CLEAR) is the first 200 MeV electron beam line to facilitate user experiments focused on dosimetry and radiobiology. Dosimetry studies with film [51], ionization chambers [225], and scintillators [23] have characterized the operating parameters of the beam in the in-air test stand. To advance the clinical translation of VHEE radiotherapy at UHDR or CDR dose rates the radiobiological effects of such beams should be characterized. The first such studies included simulations of linear energy transfer (LET) and dose-mean lineal energy [242] as well as DNA plasmid irradiations at CLEAR [37]. Survival of lung and prostate cancer cells irradiated with 154 MeV electrons using the ARES linac at DESY have also been investigated [243]. The goal of these studies was to use a range of proxy metrics for biological damage in order to determine the relative biological effectiveness (RBE) of VHEE beams. The results of these studies suggest that the radiobiological mechanisms of VHEE are similar to x-ray and proton irradiations and that the RBE of VHEE beams is close to unity.

The next step towards translation of VHEE beams into oncology practice should be to use high throughput whole-organism radiobiological models to experimentally determine the RBE compared to the lower electron energies commonly used in the clinic. *Drosophila melanogaster* have advantages over more frequently used radiobiological models for both

practical and biological reasons. From the early history of radiobiology [173, 174, 175] to more recent studies investigating the complexities of dose rate [179, 180], *D. melanogaster* have provided a statistically powerful model of how ionizing radiation affects a whole organism. The short life cycle (∼10 days from egg to adult fly) allows for quick determination of dose response and limited follow up time. The genome of *D. melanogaster* is well characterized and includes many homologs to human genes, including those responsible for DNA damage repair pathways [188]. In this work we examine the survival and overall physiological responses of *D. melanogaster* larvae irradiated with ∼10 to 50 Gy with the 200 MeV beam at CLEAR and 9 - 20 MeV electrons produced by a clinical linear accelerator. Additionally we evaluate the effects of these beams at both UHDR and CDR. This first study of an *in vivo* model is an important step towards clinical translation of VHEE beams.

Results

To explore the radiobiological effects of VHEE, *D. melanogaster* larvae were irradiated to doses of 15 to 45 Gy with 200 MeV electrons at CLEAR and 9-20 MeV electrons produced by a conventional radiotherapy linac. Post irradiation the larvae were tracked through development to adulthood as described in Figure 7.1. Eclosion of adult flies was used to assess the possibility of normal tissue sparing at ultrahigh dose-rates as well as the RBE of VHEE beams. For UHDR irradiations the average dose rate (normalized by total treatment time) were 130 Gy/s, and 3×10^8 Gy/s for 10 MeV and 200 MeV, respectively. CDR treatments at both 9-20 MeV and 200 MeV were delivered at 0.2 Gy/s.

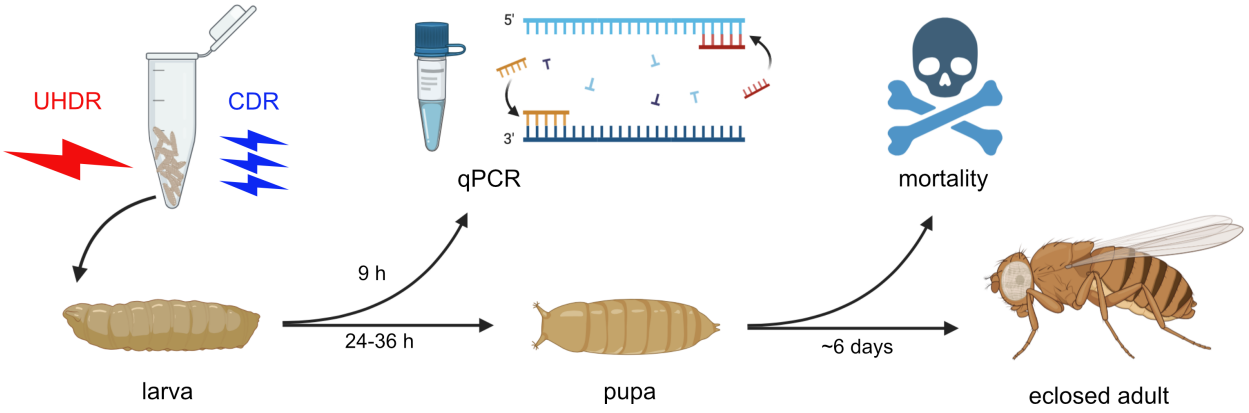

Figure 7.1: Experimental design for the *D. melanogaster* irradiations with VHEE and 9-20 MeV electrons. Larvae were irradiated with UHDR or CDR at each dose and electron energy, before being tracked through development to adulthood. Larvae irradiated with 200 MeV at CLEAR were also frozen at 9 h post irradiation for qPCR analysis.

7.1.1 Dosimetry

Films placed on either side of *D. melanogaster* larvae during VHEE irradiations are shown in Figure 7.2, which allowed for retrospective determination of the delivered doses and beam sizes. The average beam size was 5.9 mm × 6.2 mm ($x \times y$, 1-σ). The three closest delivered doses determined from film were treated as replicates. Analysis was conducted using the three to five closest doses. Using three neighboring doses was found to minimize the standard deviation of eclosion and mean dose delivered for each dose group.

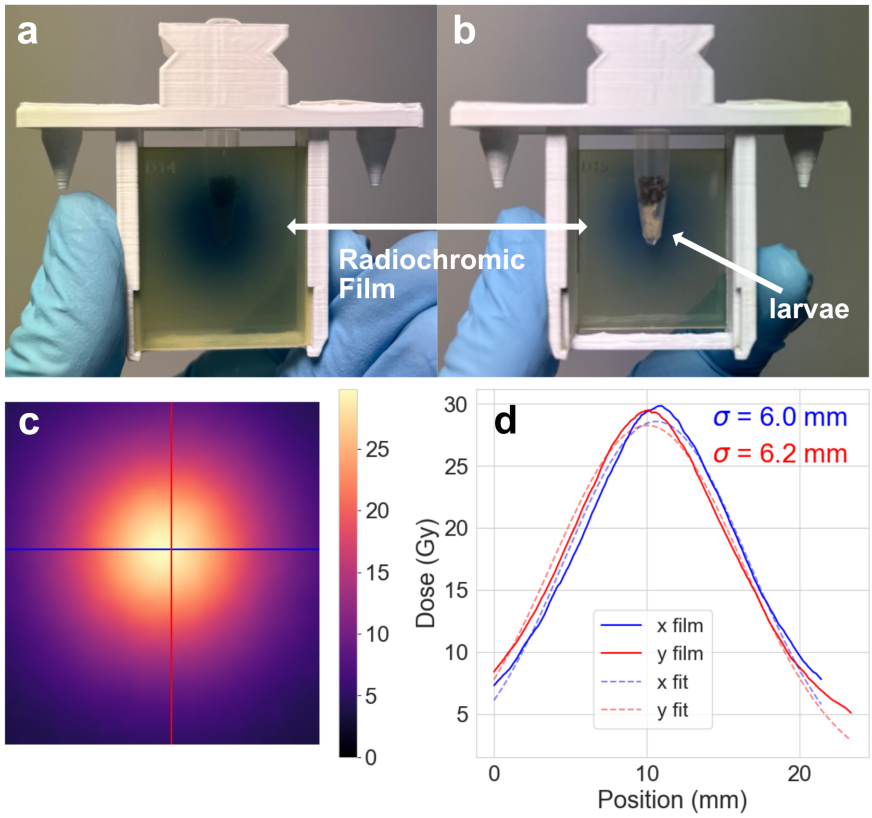

Figure 7.2: Radiochromic films placed upstream (a) and downstream (b) of irradiated larvae immobilized within a 0.5 ml eppordorf tube held in a 3D-printed jig. An example dose map (c) and corresponding gaussian profiles of the 200 MeV beam (d).

7.1.2 Larvae development

Post irradiation, larvae developed into pupae and then emerged as adult flies several days later. The rate of survival to adulthood decreased with dose as shown in Figure 7.3. No significant differences between response curves generated from UHDR and CDR were observed with either 200 MeV (Figure 7.3a) or 9-20 MeV electrons (Figure 7.3b). Individual dose groups were directly compared only for 9 MeV CDR and 10 MeV UHDR irradiations

because identical doses were delivered for all replicates and experiments were conducted on the same day. Mean eclosion rates presented in Figure 7.3 are summarized in Table 7.1. The eclosion rate for flies irradiated to 20 Gy with 10 MeV UHDR was 18% higher than flies irradiated with 9 MeV CDR ($p < 0.05$).

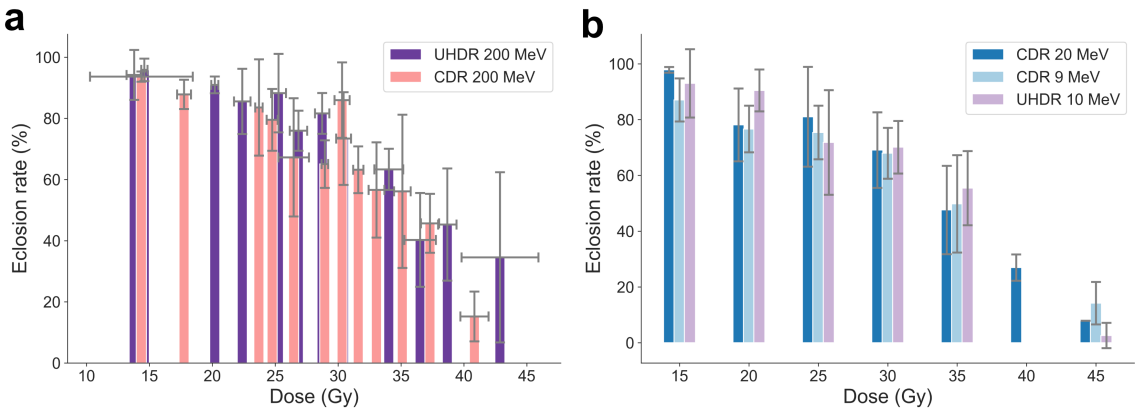

Figure 7.3: Eclosion (emergence as viable adult flies) irradiated with UHDR and CDR using VHEE (a) and 9-20 MeV electrons (b). Error bars show the standard deviation of three replicates (n ∼120 for each dose).

Table 7.1: Mean eclosion rates and dose modifying factors for flies irradiated with 10 MeV UHDR and 9 MeV CDR electrons.

Dose (Gy)	10 MeV UHDR	9 MeV CDR	UHDR/CDR	p-value
15	0.93	0.87	1.07	0.25
20	0.90	0.77	1.18	**0.039***
25	0.72	0.75	0.95	0.670
30	0.70	0.68	1.03	0.391
35	0.55	0.50	1.11	0.254
45	0.03	0.14	0.18	0.968

The ED_{50} was calculated from the polynomial fit for each dose response shown in Figure 7.4 and is reported in Table 7.2. The highest observed ED_{50} was 37.4 Gy for UHDR 200 MeV and the lowest was 34.6 Gy for CDR 20 MeV. These values were used to determine dose modifying factors for UHDR relative to CDR of 1.07 for VHEE and 1.01 for 9-20 MeV electrons. The average ED_{50} from 9/20 MeV electrons and CDR VHEE were also used to calculate a RBE value of ∼1 (0.97 - 1.01 within 1-σ).

D. melanogaster larvae that survived to adulthood exhibited symptoms of radiation damage which were not quantified in this study. These included failure to completely emerge from the pupal case (which were not counted in the eclosion rate calculation). Other defor-

Table 7.2: Calculated ED_{50} for each beam energy and dose-rate. The R^2 from the polynomial fit shown in Figure 7.4 is also reported.

Source	Mode	Energy	ED50 (Gy)	R^2
CLEAR	CDR	200 MeV	35.1 ± 0.7	0.93
CLEAR	UHDR	200 MeV	37.4 ± 0.7	0.87
TrueBeam	CDR	20 MeV	34.6 ± 1.0	0.98
TrueBeam	CDR	9 MeV	35.3 ± 0.8	0.99
TrueBeam	UHDR	10 MeV	35.2 ± 1.0	0.98

mities included wings that failed to completely open or close. The fecundity of adult flies was monitored by checking food vials for progeny. No offspring were found in vials containing flies irradiated with 40 Gy and higher at either 10 MeV UHDR or CDR with 9/20 MeV electrons. Offspring were found in vials of flies irradiated up to 35 Gy. Adult flies were not kept from the VHEE irradiations.

Discussion

D. melanogaster larvae irradiated with UHDR electrons at both conventional and very high energies exhibited similar dose response compared to CDR treatments. Additionally there were not significant differences in dose response between irradiations with 200 MeV and 9-20 MeV electrons. From the measured dose responses, and specifically the corresponding ED_{50} values, we can conclude that the RBE of 200 MeV electrons is very close to unity. This study is the first *in vivo* whole-organism investigation of the radiobiological effects of VHEE beams and should be used alongside results from simulation and *in vitro* studies to predict the clinical effectiveness of VHEE beams in human patients.

RBE is typically described as increasing with linear energy transfer (LET) [244], and on this basis it has been speculated that the RBE of VHEE beams might be between that of conventional photon/electron treatments and protons. The first simulation studies of VHEE beams to assess the macrodosimetric properties, namely LET, suggested that the RBE of VHEE would be significantly increased compared to 20 MeV electrons [242]. However, Delorme *et al.* also simulated microdosimetric properties, including dose-mean lineal energy, which predicted no difference in RBE of VHEE compared to low energy electron beams. Similarly, a DNA plasmid study conducted with the CLEAR beamline found no difference in rates of double strand breaks under VHEE conditions at both UHDR and CDR [37]. Lung and prostate cancer cells were irradiated *in vitro* with 154 MeV electrons at dose rates of 1.8 Gy/s with the ARES linear accelerator [243]. Wanstall *et al.* estimated the RBE on cancerous tissues to be between 0.93 and 0.99 compared to 300 kVp x-rays. The whole-

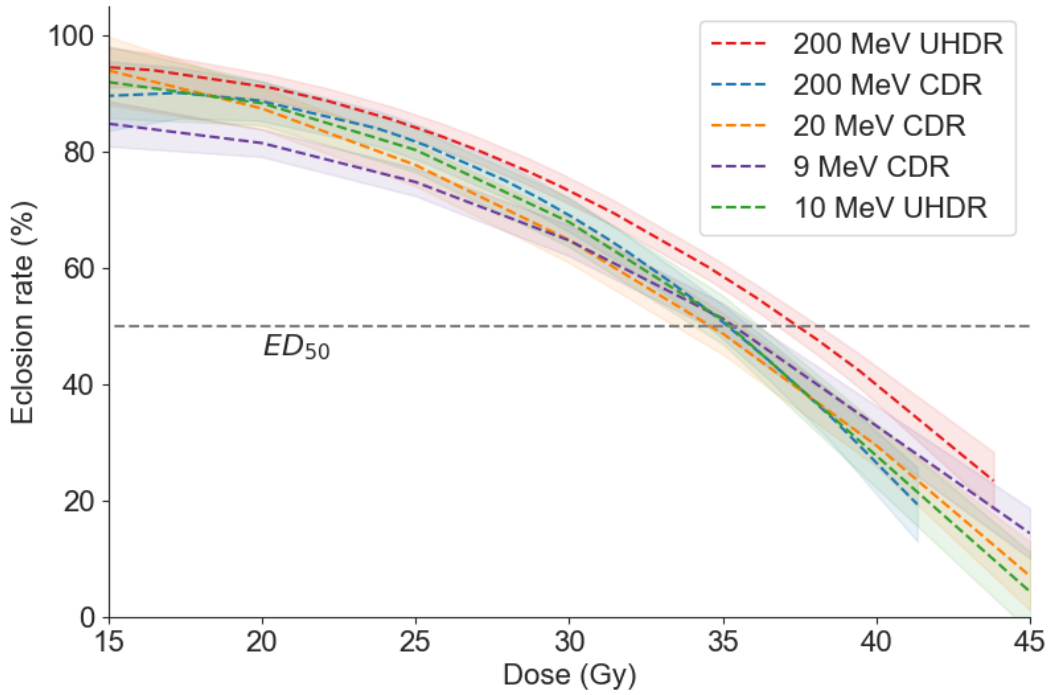

Figure 7.4: Eclosion rate as a function of dose for each energy and dose-rate was modeled with a polynomial fit in order to estimate the ED_{50}. The shaded region around the fit represents $\pm 1\sigma$ and was used to calculate the uncertainty in ED_{50} and RBE.

organism *D. melanogaster* dose response presented here is in agreement with these published results.

The ED_{50} values determined in this work are lower than other recent works investigating the dose response to 0.662 - 6 MeV x-rays and 225 MeV protons, which found that the doses required to reduce eclosion to 50% was between 40 and 50 Gy [217, 218]. It is important to note that the ED_{50} in those publications was calculated for Oregon-R flies. Nakajima *et al.* also showed that w^{1118} flies were more radio-sensitive than Oregon-R and exhibited greater variability in eclosion rate for a given dose. Assessing the dose response of Oregon-R flies to VHEE beams may allow for determination of an RBE value with higher precision. The dose response curves presented in Figures 7.3 and 7.4 differ from the sigmoidal response observed for Oregon-R flies irradiated with kilovoltage x-rays. This is likely due to both the increased RBE of low energy x-rays (which is also dose dependent), as well as the increased radiosensitivy of w^{1118} compared to Oregon-R.

The principal limitation of studying radiobiological effects of VHEE is the extreme scarcity of VHEE sources. Currently, the only operational source of 200 MeV electrons (at UHDR or CDR) is the laser-driven accelerator at CLEAR. While CLEAR is capable of producing beams with adequately uniform dose distributions and energy spread, repeatability is

a significant concern. Film dosimetry yielded different doses for UHDR and CDR doses when targeting the same charge per pulse. Further, frequent breakdowns of the photocathode-laser can result in unintended delivery of dose (either too low or too high).

Average dose rates >40 Gy/s have become synonymous with the FLASH effect [245], however the role of the peak instantaneous dose rate and the overall time structure of the treatment delivery is not well understood [150]. In addition to the differences in electron energy explored in this work, the beams studied also had significantly different time structures, as described in Table 7.3. The instantaneous dose rates of the 200 MeV beam were $\sim 4\times10^{11}$ Gy/s for both CDR and UHDR treatments (the same bunch charge was used). It should also be noted that the term UHDR is used to describe both the VHEE CLEAR beamline and the converted 20 MeV linac when operating with very different time structures. While both beams achieve average dose rates that far exceed what could be considered 'conventional', they should not be conflated as having the same properties. It is quite possible that average does rates on the order of 10^2 Gy/s and 10^9 Gy/s have very different biological effects.

The experiments presented in this work were solely focused on the radiobiological effects of electron irradiation on normal tissues. The potential benefits of FLASH radiotherapy can only be demonstrated when cancerous tissues are targeted, and the treatment results in tumour control while preferentially sparing healthy tissues. Future experiments with *D. melanogaster* could attempt to trigger this effect by irradiating tumour bearing larvae or adult flies with varying dose rates. Models for a number of human cancers have been developed for both larvae and adult *D. melanogaster* which can be used to develop new therapies [190].

Methods

7.1.3 Flies and irradiation conditions

White-eyed *D. melanogaster* (w^{1118}) were used in this study. Mid-L3 to wandering L3 larvae were placed within 0.5 ml eppendorf tubes and irradiated with either 200 MeV electrons or 9-20 MeV electrons and tracked for physiological responses as described in Figure 7.1. The irradiations were performed in a water tank for VHEE and in acrylic and Solid Water® phantoms (Sun Nuclear, Melbourne, FL) for the 9-20 MeV beams. Control groups were immobilized in tubes behind lead shielding at CLEAR and outside the linac vault for 9-20 MeV irradiations for the duration of the experiments. The positioning of larvae with respect to the 200 and 9-20 MeV beams is shown in Figure 7.5. Post irradiation, larvae were transferred to fresh food vials. The incubator was kept at 25° C.

7.1.4 Irradiation sources and dosimetry

CDR and UHDR VHEE irradiations were conducted at CLEAR using the 200 MeV beamline. Larvae were irradiated with a symmetrical 6 mm 1-σ gaussian beam positioned in a water tank in the in-air test stand. Details on the CLEAR beamline and in-air test stand capabilities are described elsewhere [47, 23]. CDR treatments were delivered at a pulse repetition rate of 0.833 Hz, with each pulse comprised of a single bunch of electrons. The UHDR treatments were delivered in a single pulse, and different doses were achieved by scaling the number of bunches per pulse. The bunch frequency for all irradiations was 1.5 GHz.

Conventional and UHDR irradiations with 9-20 MeV electrons were performed with TrueBeam (Varian Medical Systems, Palo Alto, CA) medical linear accelerators. The UHDR irradiation conditions were achieved by operating the linac in photon mode without a conversion target in the beam path [246, 228]. The targeted dose delivery and time structures of the beams are summarized in Table 7.3.

Table 7.3: Dose delivery time structures for both CDR and UHDR modes used at CLEAR and with the TrueBeam linac.

Source	Mode	Energy	Dose range	Dose per pulse	Pulse length	Irradiation time
CLEAR	CDR	200 MeV	15 - 45 Gy	~0.4 Gy	~10 ps	~4 min
CLEAR	UHDR	200 MeV	15 - 45 Gy	15 - 45 Gy	<150 ns	<150 ns
TrueBeam	CDR	9/20 MeV	15 - 45 Gy	0.16 Gy	~4 μs	2.5 - 7.5 min
TrueBeam	UHDR	10 MeV	15 - 45 Gy	0.35 Gy	~4 μs	~100 - 350 ms

Dosimetry was performed with ionization chambers and radiochromic films to confirm the delivery of consistent doses at both UHDR and CDR dose rates. Films used for 200 MeV irradiations at CLEAR were calibrated against an ionization chamber in a clinical 5.5 MeV electron beam. Laser cut and labeled MDV3 and EBT-XD Gafchromic films (Ashland, Bridgewater, NJ) were placed on both sides of the larvae during irradiations as shown in Figure 7.2. Films were scanned 24 hours post irradiation with a flatbed scanner (Expression 10000 XL, Epson, Long Beach, CA). Pixel values were converted to dose using a red channel calibration curve which was obtained using a clinical 5.5 MeV linear accelerator [200]. To verify the position of the flies with respect to the beam, additional irradiations were performed with lead placed in the eppendorf tubes in place of larvae. The position of the lead on the films was used to draw the regions-of-interest (ROIs) for evaluation of the dose to larvae. The mean value of the pixels contained in the ROI was reported as the delivered dose.

Dosimetry for the 10 MeV UHDR irradiations was performed with a CC01 ionization chamber (IBA, Freiburg, Germany). The CC01 ionization chamber was calibrated under

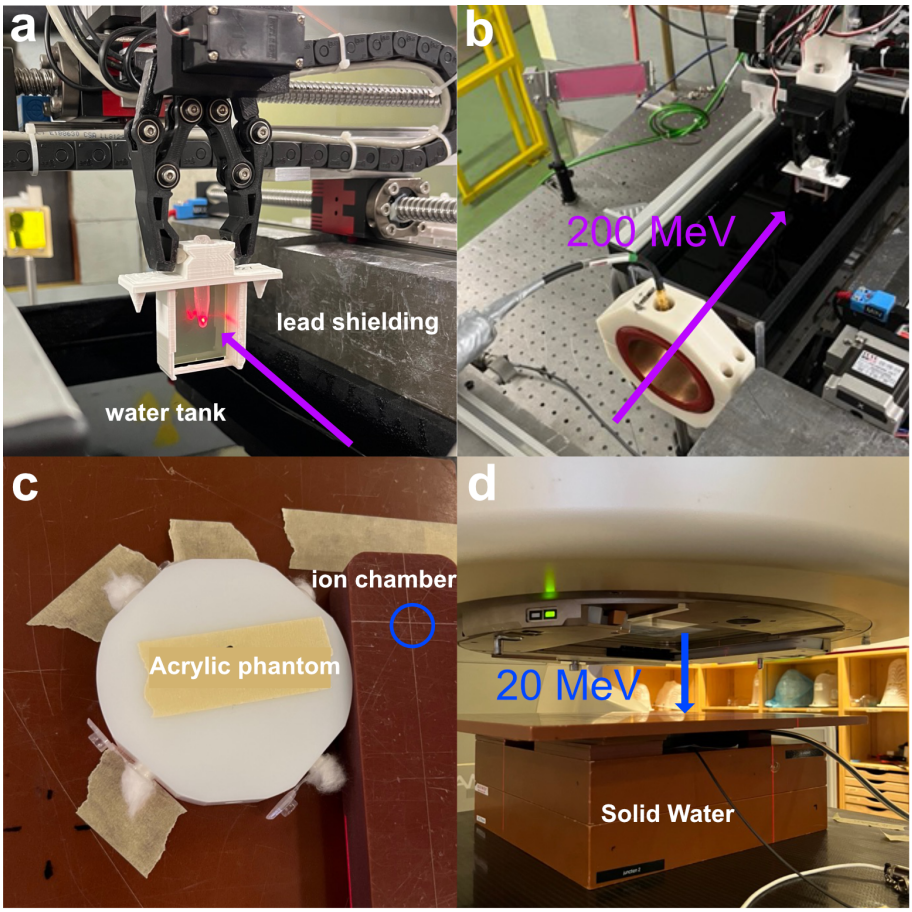

Figure 7.5: Irradiation setup with 200 MeV electrons at CLEAR (a,b) and 9-20 MeV electrons produced by a TrueBeam (c,d). A 3D-printed holder for positioning larvae filled eppendorf tubes is aligned with a laser indicating the center of the CLEAR beam line (a). The holders are centered on the beam using the C-Robot (b). An acrylic jig for immobilizing larvae during 9-20 MeV electron irradiations (c) placed within blocks of solid water (d).

standard reference dose conditions using a 9 MeV electron beam operating at 600 MU/min (0.1 Gy/s average dose rate), with a 10x10 cm^2 electron cone, at 100 cm source-to-surface-distance and depth of 2 cm in a Solid Water® phantom. This beam had previously been calibrated using the AAPM TG-51 protocol [61] to deliver 1 cGy/MU at the reference conditions and was monitored daily as part of the institutional quality assurance program to maintain consistency within ±2%. The CC01 chamber was cross-calibrated with a calorimeter under UHDR conditions. Comparisons between the CC01 chamber and passive dosimeters, including optically stimulated luminescent dosimeters (OSLDs) and radiochromic film, agreed within 5%. For the UHDR fly irradiations, the ionization chamber was placed within the field and off-axis correction factors were used to determine the dose delivered to the larvae.

The doses for the 9 and 20 MeV CDR irradiations were determined using the monitor chamber in the linac treatment head. The larvae were placed in Solid Water® phantoms at the reference depth for both energies which allowed for delivering 1 cGy/MU.

7.1.5 Survival analysis

Flies were scored for eclosion (complete emergence of adults from pupae) starting at 5-7 days post irradiation. Fractional eclosion for each vial was calculated as:

$$\%\,\text{eclosion} = \frac{n_{\text{adults}}}{n_{\text{pupae}}} \times 100\% \tag{7.1}$$

where n_{adults} was the maximum number of adult flies emerged post irradiation and n_{pupae} was the number of pupae counted in the vial several days post irradiation. Normalizing to the number of pupae allowed for variation in the number of irradiated larvae per vial and excluded any larvae killed while transferring between vials. The mean and standard deviation of eclosion for four replicates for 9-20 MeV irradiations and three nearest doses for 200 MeV irradiations was reported. The mean eclosion rates were also normalized to the control groups on each day. Data from experimental days with average eclosion rate from control groups less than 95% were excluded from analysis.

Eclosion rate as a function of dose was modeled using a second-order polynomial. From the polynomial fit, the dose to 50% eclosion (ED_{50}) was calculated. The ED_{50} values were then compared to assess possible tissue sparing effects of UHDR treatments as well as the RBE of 200 MeV electrons compared to 9-20 MeV electrons routinely used for radiotherapy. The RBE was defined as

$$RBE = \frac{ED_{50,CE}}{ED_{50,VHEE}} \tag{7.2}$$

where $ED_{50,VHEE}$, and $ED_{50,CE}$ were the doses required to reach 50% eclosion with the 200 MeV and 9-20 MeV conventional energy (CE) beams, respectively. Flies irradiated with 9-20 MeV electrons were kept to monitor fertility. After flipping adults into new vials twice weekly, the previous vials were kept in order to check for offspring production.

7.1.6 Statistical analysis

All statistical analyses were performed with Python 3.10. Mann-Whitney U tests and Student's t-tests were performed to assess differences in eclosion between irradiation groups. Results were regarded as significant for eclosion at $p < 0.05$.

Chapter 8

Conclusions and Future Work

In this thesis, four investigations have been presented which contribute to the field of UHDR-RT. The first goal of this work was to test the ability of PSDs to accurately measure novel UHDR radiation sources including a shutter operated kilovoltage x-ray tube and the VHEE beamline at CLEAR. The second objective of this work was to discern the radiobiological effects of the same radiation sources using a low-cost, and high-throughput model. To this end, *Drosophila melanogaster* were irradiated at CDR and UHDR with both sources, and were observed for several physiological endpoints.

8.1 Plastic scintillator dosimetry

It was demonstrated that PSDs doped with varying concentrations of lead can accurately measure dose from UHDR x-ray sources. Each of the tested detectors showed excellent linearity with dose rate from 1.1 to 40.1 Gy/s, and with exposure time from 1 to 100 ms. It was also shown that lead-doped PSDs were more tissue equivalent dosimeters than pure polystyrene-based PSDs for kilovoltage x-rays. This may be a valuable insight for selecting PSD compositions for kilovoltage radiotherapy applications.

PSDs were also shown to be useful dosimeters for the 200 MeV VHEE beam at the CLEAR facility. In this application, PSDs demonstrated linear response with dose up to 125.2 Gy delivered in a single train at a dose rate of 1.21×10^9 Gy/s. The output of PSDs decreased after being damaged with several kGy. However, after resting the probes, they experienced varying degrees of output recovery. The permanence of the radiation damage and the dose dependent time scales necessary for recovery requires further investigation. For applications in both CDR and UHDR-RT, it is important to characterize the loss of output and subsequent recovery of PSDs. This may allow for PSDs with traceable calibrations to be employed in clinical use.

8.2 Fruit fly radiobiology

The experiments described in this thesis demonstrate that *Drosophila* are a useful model organism to study the radiobiological effects of both dose rate and electron beam energy. Irradiation of *Drosophila* larvae with low-energy UHDR x-rays showed reduced toxicity compared to conventional dose-rate irradiation, as evidenced by improved larval development at 24 Gy and increased median survival at 22 Gy. These normal tissue sparing effects were observed at dose rates of ∼200 Gy/s delivered in a single sub-second pulse, demonstrating the potential of low-energy UHDR x-rays for clinical FLASH radiotherapy. Shutter controlled x-ray sources could potentially be used for UDHR treatment of skin cancers and other shallow lesions, with reduced risk to surrounding tissue.

Drosophila experiments with the CLEAR beamline enabled the first experimental estimation of the RBE of VHEE beams using an *in vivo* model. Consistent with macrodosimetric studies and DNA plasmid experiments at CLEAR, the RBE for VHEE at CDR was determined to be between 0.97 and 1.01. This work represents the first *in vivo* study of VHEE beams with a whole-organism model which developed to adulthood.

While there were not significant differences in the overall eclosion curves between flies irradiated with CDR and UHDR at VHEE, there were signs of differential response. At doses between 22 and 33 Gy flies eclosed at higher rates from the UHDR group while also showing higher expression of p53 and apoptosis effectors. These results indicate that further experiments with *Drosophila* could provide a mechanistic insight into the FLASH effect. The next set of experiments should involve qPCR testing at multiple time points to better understand the role of several apoptosis-related genes and proteins in the physiological response to UHDR-RT. Future experiments can also be improved by utilizing a flattening filter to deliver more uniform dose distributions to the flies within a single vial.

The findings of this thesis suggest that normal tissue sparing is possible with two very different UHDR radiation sources, which each have unique advantages over conventional megavoltage radiotherapy. However, no investigation of the efficacy of UHDR-RT on tumour tissues was undertaken with these beams as part of this thesis work, and conclusions towards the FLASH effect must be cautioned. The results presented here merit additional study using *Drosophila* tumour models, and further probing of gene expression. UHDR experiments with *Drosophila* are less expensive than using murine models and allow for investigations at high-energy physics facilities like CERN which are often otherwise restricted from radiobiological research.

Bibliography

[1] *Health Promotion and Chronic Disease Prevention in Canada*, 41(11):399–399, November 2021.

[2] Rajamanickam Baskar, Kuo Ann Lee, Richard Yeo, and Kheng-Wei Yeoh. Cancer and radiation therapy: Current advances and future directions. *International Journal of Medical Sciences*, 9(3):193–199, 2012.

[3] Hyun Do Huh and Seonghoon Kim. History of radiation therapy technology. *Progress in Medical Physics*, 31(3):124–134, September 2020.

[4] Henri Becquerel and Pierre Curie. Action physiologique des rayons du radium. *Compt. Rend. Acad. Sci*, 132:1289–1291, 1901.

[5] Yunfei Jiao, Fangyu Cao, and Hu Liu. Radiation-induced cell death and its mechanisms. *Health Physics*, 123(5):376–386, September 2022.

[6] Karl Otto. Volumetric modulated arc therapy: Imrt in a single gantry arc. *Medical Physics*, 35(1):310–317, December 2007.

[7] Refurbished Varian TrueBeam Linear Accelerator — ROS — oncologysystems.com. https://www.oncologysystems.com/inventory/medical-equipment-for-sale/used-linear-accelerators/varian-truebeam-linear-accelerator-3. [Accessed 28-04-2024].

[8] Damodar Pokhrel, Lana Sanford, Bhaswanth Dhanireddy, Janelle Molloy, Marcus Randall, and Ronald C. McGarry. Flattening filter free vmat for a stereotactic, single-dose of 30 gy to lung lesion in a 15-min treatment slot. *Journal of Applied Clinical Medical Physics*, 21(4):6–12, February 2020.

[9] Kavita K. Mishra and Inder K. Daftari. Proton therapy for the management of uveal melanoma and other ocular tumors. *Chinese Clinical Oncology*, 5(4):50–50, August 2016.

[10] Heike Thomas and Beate Timmermann. Paediatric proton therapy. *The British Journal of Radiology*, 93(1107), September 2019.

[11] Magdalena Bazalova-Carter, Bradley Qu, Bianey Palma, Björn Hårdemark, Elin Hynning, Christopher Jensen, Peter G. Maxim, and Billy W. Loo. Treatment planning for radiotherapy with very high-energy electron beams and comparison of VHEE and VMAT plans. *Medical Physics*, 42(5):2615–2625, 2015.

[12] Vincent Favaudon, Laura Caplier, Virginie Monceau, Frédéric Pouzoulet, Mano Sayarath, Charles Fouillade, Marie-France Poupon, Isabel Brito, Philippe Hupé, Jean Bourhis, Janet Hall, Jean-Jacques Fontaine, and Marie-Catherine Vozenin. Ultrahigh dose-rate FLASH irradiation increases the differential response between normal and tumor tissue in mice. *Science Translational Medicine*, 6(245):245ra93–245ra93, 2014.

[13] Marie Catherine Vozenin, Pauline De Fornel, Kristoffer Petersson, Vincent Favaudon, Maud Jaccard, Jean François Germond, Benoit Petit, Marco Burki, Gisele Ferrand, David Patin, Hanan Bouchaab, Mahmut Ozsahin, François Bochud, Claude Bailat, Patrick Devauchelle, and Jean Bourhis. The Advantage of FLASH Radiotherapy Confirmed in Mini-pig and Cat-cancer Patients. *Clinical Cancer Research*, 25(1):35–42, 2019.

[14] T. E. Schmid, G. Dollinger, A. Hauptner, V. Hable, C. Greubel, S. Auer, A. A. Friedl, M. Molls, and B. Röper. No evidence for a different rbe between pulsed and continuous 20 mev protons. *Radiation Research*, 172(5):567–574, November 2009.

[15] A. S. Beddar, T. R. Mackie, and F. H. Attix. Water-equivalent plastic scintillation detectors for high-energy beam dosimetry: I. Physical characteristics and theoretical considerations. *Physics in Medicine and Biology*, 37(10):1883–1900, 1992.

[16] A S Beddar, T R Mackie, and F H Attix. Water-equivalent plastic scintillation detectors for high-energy beam dosimetry: II. Properties and measurements. *Physics in Medicine and Biology*, 37(10):1901–1913, oct 1992.

[17] James Archer, Enbang Li, Jeremy Davis, Matthew Cameron, Anatoly Rosenfeld, and Michael Lerch. High spatial resolution scintillator dosimetry of synchrotron microbeams. *Scientific Reports*, 9(1):1–7, 2019.

[18] Daniel D. Cecchi, François Therriault-Proulx, Simon Lambert-Girard, Alexander Hart, Andrew Macdonald, Mike Pfleger, Mark Lenckowski, and Magdalena Bazalova-Carter.

Characterization of an x-ray tube-based ultrahigh dose-rate system for in vitro irradiations. *Medical Physics*, 48(11):7399–7409, 2021.

[19] Anthony E. Mascia, Emily C. Daugherty, Yongbin Zhang, Eunsin Lee, Zhiyan Xiao, Mathieu Sertorio, Jennifer Woo, Lori R. Backus, Julie M. McDonald, Claire McCann, Kenneth Russell, Lisa Levine, Ricky A. Sharma, Dee Khuntia, Jeffrey D. Bradley, Charles B. Simone, John P. Perentesis, and John C. Breneman. Proton FLASH Radiotherapy for the Treatment of Symptomatic Bone Metastases: The FAST-01 Nonrandomized Trial. *JAMA Oncology*, 9(1):62–69, 2023.

[20] EC Daugherty, Y Zhang, Z Xiao, AE Mascia, M Sertorio, J Woo, C McCann, KJ Russell, RA Sharma, D Khuntia, JD Bradley, CB Simone, JC Breneman, and JP Perentesis. Flash radiotherapy for the treatment of symptomatic bone metastases in the thorax (fast-02): protocol for a prospective study of a novel radiotherapy approach. *Radiation Oncology*, 19(1), March 2024.

[21] Rémy Kinj, Olivier Gaide, Wendy Jeanneret-Sozzi, Urania Dafni, Stéphanie Viguet-Carrin, Enea Sagittario, Magdalini Kypriotou, Julie Chenal, Frederic Duclos, Marine Hebeisen, Teresa Falco, Reiner Geyer, Patrik Gonçalves Jorge, Raphaël Moeckli, and Jean Bourhis. Randomized phase ii selection trial of flash and conventional radiotherapy for patients with localized cutaneous squamous cell carcinoma or basal cell carcinoma: A study protocol. *Clinical and Translational Radiation Oncology*, 45:100743, March 2024.

[22] Alexander Hart, Daniel Cecchi, Cloé Giguère, Frédérique Larose, and François Therriault-proulx. Lead-doped scintillator dosimeters for detection of ultrahigh dose-rate x-rays. 2022.

[23] Alexander Hart, Cloé Giguère, Joseph Bateman, Pierre Korysko, Wilfrid Farabolini, Vilde Rieker, Nolan Esplen, Roberto Corsini, Manjit Dosanjh, Luc Beaulieu, and Magdalena Bazalova-Carter. Plastic scintillator dosimetry of ultrahigh dose-rate 200 mev electrons at clear. *IEEE Sensors Journal*, pages 1–1, 2024.

[24] Lise Meitner. Uber die entstehung der?-strahl-spektren radioaktiver substanzen. *Zeitschrift fur Physik*, 9(1):131–144, December 1922.

[25] J A O'Donoghue and T E Wheldon. Targeted radiotherapy using auger electron emitters. *Physics in Medicine and Biology*, 41(10):1973–1992, October 1996.

[26] F.H. Attix. *Introduction to Radiological Physics and Radiation Dosimetry*. A Wiley-Interscience publication. Wiley, 1986.

[27] H.E. Johns and J.R. Cunningham. *The Physics of Radiology*. Charles C. Thomas Publisher, Limited, 1984.

[28] *Proceedings of the Royal Society of London. Series A, Containing Papers of a Mathematical and Physical Character*, 146(856):83–112, August 1934.

[29] H Nikjoo and D T Goodhead. Track structure analysis illustrating the prominent role of low-energy electrons in radiobiological effects of low-let radiations. *Physics in Medicine and Biology*, 36(2):229–238, February 1991.

[30] Martin Berger, J Coursey, and M Zucker. ESTAR, PSTAR, and ASTAR: Computer Programs for Calculating Stopping-Power and Range Tables for Electrons, Protons, and Helium Ions (version 1.21), 1999.

[31] Émily Cloutier, Luc Beaulieu, and Louis Archambault. Direct in-water radiation dose measurements using cherenkov emission corrected signals from polarization imaging for a clinical radiotherapy application. *Scientific Reports*, 12(1), June 2022.

[32] Jean Bourhis, Wendy Jeanneret Sozzi, Patrik Gonçalves Jorge, Olivier Gaide, Claude Bailat, Fréderic Duclos, David Patin, Mahmut Ozsahin, François Bochud, Jean François Germond, Raphaël Moeckli, and Marie Catherine Vozenin. Treatment of a first patient with FLASH-radiotherapy. *Radiotherapy and Oncology*, 139:18–22, 2019.

[33] Pierre Montay-Gruel, Kristoffer Petersson, Maud Jaccard, Gaël Boivin, Jean François Germond, Benoit Petit, Raphaël Doenlen, Vincent Favaudon, François Bochud, Claude Bailat, Jean Bourhis, and Marie Catherine Vozenin. Irradiation in a flash: Unique sparing of memory in mice after whole brain irradiation with dose rates above 100 Gy/s. *Radiotherapy and Oncology*, 124(3):365–369, 2017.

[34] Karolina Kokurewicz, Enrico Brunetti, Alessandro Curcio, Davide Gamba, Luca Garolfi, Antonio Gilardi, Eugenio Senes, Kyrre Ness Sjobak, Wilfrid Farabolini, Roberto Corsini, and Dino Anthony Jaroszynski. An experimental study of focused very high energy electron beams for radiotherapy. *Communications Physics*, 4(1), 2021.

[35] Agnese Lagzda, Deepa Angal-Kalinin, James Jones, Adam Aitkenhead, Karen J Kirkby, Ranald MacKay, Marcel Van Herk, Wilfrid Farabolini, Sumaira Zeeshan, and

Roger M Jones. Influence of heterogeneous media on Very High Energy Electron (VHEE) dose penetration and a Monte Carlo-based comparison with existing radiotherapy modalities. *Nuclear Instruments and Methods in Physics Research Section B: Beam Interactions with Materials and Atoms*, 482:70–81, 2020.

[36] Kyle Kim, Michele M. Kim, Giorgos Skoufos, Eric S. Diffenderfer, Seyyedeh Azar Oliaei Motlagh, Michail Kokkorakis, Ilektra Koliaki, George Morcos, Khayrullo Shoniyozov, Joanna Griffin, Artemis G. Hatzigeorgiou, James M. Metz, Alexander Lin, Steven J. Feigenberg, Keith A. Cengel, Bonnie Ky, Constantinos Koumenis, and Ioannis I. Verginadis. Flash proton radiation therapy mitigates inflammatory and fibrotic pathways and preserves cardiac function in a preclinical mouse model of radiation-induced heart disease. *International Journal of Radiation Oncology*Biology*Physics*, 119(4):1234–1247, July 2024.

[37] K L Small, N T Henthorn, D Angal-Kalinin, A L Chadwick, E Santina, A Aitkenhead, K J Kirkby, R J Smith, M Surman, J Jones, W Farabolini, R Corsini, D Gamba, A Gilardi, M J Merchant, and R M Jones. Evaluating very high energy electron RBE from nanodosimetric pBR322 plasmid DNA damage. *Scientific Reports*, 11(1):3341, 2021.

[38] Pierre Montay-Gruel, Munjal M. Acharya, Patrik Gonçalves Jorge, Benoît Petit, Ioannis G. Petridis, Philippe Fuchs, Ron Leavitt, Kristoffer Petersson, Maude Gondre, Jonathan Ollivier, Raphael Moeckli, François Bochud, Claude Bailat, Jean Bourhis, Jean François Germond, Charles L. Limoli, and Marie Catherine Vozenin. Hypofractionated FLASH-RT as an effective treatment against glioblastoma that reduces neurocognitive side effects in mice. *Clinical Cancer Research*, 27(3):775–784, 2021.

[39] Jerrold T. Bushberg, J. Anthony Seibert, Edwin M. Leidholdt, John M. Boone, and Edward J. Goldschmidt. *The Essential Physics of Medical Imaging*, volume 30. 2003.

[40] Magdalena Bazalova-Carter and Nolan Esplen. On the capabilities of conventional x-ray tubes to deliver ultra-high (FLASH) dose rates. *Medical Physics*, 46(12):5690–5695, 2019.

[41] Mohammad Rezaee, Iulian Iordachita, and John W Wong. Ultrahigh dose-rate (FLASH) x-ray irradiator for pre-clinical laboratory research. *Physics in Medicine Biology*, 66(9):95006, apr 2021.

[42] Devin Miles, Daniel Sforza, John Wong, and Mohammad Rezaee. Dosimetric characterization of a rotating anode x-ray tube for FLASH radiotherapy research. *Medical Physics*, 51(2):1474–1483, 2024.

[43] C. J. Karzmark and N. C. Pering. Electron linear accelerators for radiation therapy: History, principles and contemporary developments. *Physics in Medicine and Biology*, 18(3):321–354, 1973.

[44] S.V. Kutsaev, R. Agustsson, A. Arodzero, R. Berry, A. Bezhanov, S. Boucher, O. Chimalpopoca, A. Diego, L. Faillace, D. Gavryushkin, M. Harrison, J.J. Hartzell, J. McNevin, M. Ruelas, A. Yu Smirnov, A. Verma, and K. Woods. Compact x-band electron linac for radiotherapy and security applications. *Radiation Physics and Chemistry*, 185:109494, August 2021.

[45] Liuyuan Zhou, Hao Zha, Jiaru Shi, Jiaqi Qiu, Chuanjing Wang, Xiancai Lin, Focheng Liu, Jian Gao, and Huaibi Chen. Development of a high-gradient x-band rf gun with replaceable field emission cathodes for rf breakdown studies. *Nuclear Instruments and Methods in Physics Research Section A: Accelerators, Spectrometers, Detectors and Associated Equipment*, 1027:166206, March 2022.

[46] Maria Grazia Ronga, Marco Cavallone, Annalisa Patriarca, Amelia Maia Leite, Pierre Loap, Vincent Favaudon, Gilles Créhange, and Ludovic De Marzi. Back to the future: Very high-energy electrons (vhees) and their potential application in radiation therapy. *Cancers*, 13(19):1–19, 2021.

[47] D. Gamba, R. Corsini, S. Curt, S. Doebert, W. Farabolini, G. Mcmonagle, P. K. Skowronski, F. Tecker, S. Zeeshan, E. Adli, C. A. Lindstrøm, A. Ross, and L. M. Wroe. The CLEAR user facility at CERN. *Nuclear Instruments and Methods in Physics Research, Section A: Accelerators, Spectrometers, Detectors and Associated Equipment*, 909(December 2017):480–483, 2018.

[48] Eva Sicking and Rickard Ström. From precision physics to the energy frontier with the compact linear collider. *Nature Physics*, 16(4):386–392, April 2020.

[49] Walter Wuensch, Nuria Catalán Lasheras, Alberto Degiovanni, Steffen Döbert, Wilfrid Farabolini, Jan Kovermann, Gerard McMonagle, Stephane Rey, Igor Syratchev, Joseph Tagg, Luca Timeo, and Benjamin Woolley. Experience operating an x-band high-power test stand at cern. *Proceedings of the 5th Int. Particle Accelerator Conf.*, IPAC2014:Germany, 2014.

[50] K N Sjobak, E Adli, C A Lindstrom, M Bergamaschi, S Burger, R Corsini, A Curcio, S Curt, S Doebert, W Farabolini, D Gamba, L Garolfi, A Gilardi, I Gorgisyan, E Granados, H Guerin, R Kieffer, M Krupa, T Lefevre, S Mazzoni, G McMonagle, H Panuganti, S Pitman, V Rude, A Schlogelhofer, P K Skowronski, M Wendt, A Zemanek, Switzerland J Nadenau, Forschungszentrum Jülich, Germany A Lyapin, and Jai at Royal Holloway. Status of the Clear Electron Beam User Facility At Cern. *Int. Particle Accelerator Conf.*, (July):983–986, 2019.

[51] Daniela Poppinga, Rafael Kranzer, Wilfrid Farabolini, Antonio Gilardi, Roberto Corsini, Vanessa Wyrwoll, Hui Khee Looe, Björn Delfs, Lukas Gabrisch, and Björn Poppe. VHEE beam dosimetry at CERN Linear Electron Accelerator for Research under ultra-high dose rate conditions. *Biomedical Physics and Engineering Express*, 7(1), 2020.

[52] V F Rieker, W Farabolini, R Corsini, J J Bateman, P Korysko, L A Dyks, and United Kingdom. VHEE HIGH DOSE RATE DOSIMETRY STUDIES IN CLEAR. *Proceedings of IPAC2022*, pages 3026–3029.

[53] D. Angal-Kalinin, A. Bainbridge, A. D. Brynes, R. K. Buckley, S. R. Buckley, G. C. Burt, R. J. Cash, H. M. Castaneda Cortes, D. Christie, J. A. Clarke, R. Clarke, L. S. Cowie, P. A. Corlett, G. Cox, K. D. Dumbell, D. J. Dunning, B. D. Fell, K. Gleave, P. Goudket, A. R. Goulden, S. A. Griffiths, M. D. Hancock, A. Hannah, T. Hartnett, P. W. Heath, J. R. Henderson, C. Hill, P. Hindley, C. Hodgkinson, P. Hornickel, F. Jackson, J. K. Jones, T. J. Jones, N. Joshi, M. King, S. H. Kinder, N. J. Knowles, H. Kockelbergh, K. Marinov, S. L. Mathisen, J. W. McKenzie, K. J. Middleman, B. L. Militsyn, A. Moss, B. D. Muratori, T. C. Q. Noakes, W. Okell, A. Oates, T. H. Pacey, V. V. Paramanov, M. D. Roper, Y. Saveliev, D. J. Scott, B. J. A. Shepherd, R. J. Smith, W. Smith, E. W. Snedden, N. R. Thompson, C. Tollervey, R. Valizadeh, A. Vick, D. A. Walsh, T. Weston, A. E. Wheelhouse, P. H. Williams, J. T. G. Wilson, and A. Wolski. Design, specifications, and first beam measurements of the compact linear accelerator for research and applications front end. *Phys. Rev. Accel. Beams*, 23:044801, Apr 2020.

[54] Frank Stephan, Matthias Gross, Anna Grebinyk, Zakaria Aboulbanine, Zohrab Amirkhanyan, Volker Budach, Vincent Henrique Ehrhardt, Angeles Faus-Golfe, Marcus Frohme, Jean-Francois Germond, James David Good, Florian Grüner, David Kaul, Mikhail Krasilnikov, Ron Leavitt, Wim Leemans, Xiangkun Li, Gregor Loisch, Frieder Müller, Georg Müller, Frank Obier, Anne Oppelt, Sebastian Philipp, Houjun Qian, Ju-

dith Reindl, Felix Riemer, Martin Sack, Michael Schmitz, Tobias Schnautz, Andreas Schüller, Theresa Staufer, Christian Stegmann, Gohar Tsakanova, Marie-Catherine Vozenin, Hans Weise, Steven Worm, and Daniel Zips. FLASHlab@PITZ: New RD platform with unique capabilities for electron FLASH and VHEE radiation therapy and radiation biology under preparation at PITZ. *Physica Medica*, 104:174–187, 2022.

[55] Oct 2023.

[56] L. Faillace, D. Alesini, G. Bisogni, F. Bosco, M. Carillo, P. Cirrone, G. Cuttone, D. De Arcangelis, A. De Gregorio, F. Di Martino, V. Favaudon, L. Ficcadenti, D. Francescone, G. Franciosini, A. Gallo, S. Heinrich, M. Migliorati, A. Mostacci, L. Palumbo, V. Patera, A. Patriarca, J. Pensavalle, F. Perondi, R. Remetti, A. Sarti, B. Spataro, G. Torrisi, A. Vannozzi, and L. Giuliano. Perspectives in linear accelerator for FLASH VHEE: Study of a compact C-band system. *Physica Medica*, 104(November):149–159, 2022.

[57] A. Subiel, V. Moskvin, G. H. Welsh, S. Cipiccia, D. Reboredo, P. Evans, M. Partridge, C. DesRosiers, M. P. Anania, A. Cianchi, A. Mostacci, E. Chiadroni, D. Di Giovenale, F. Villa, R. Pompili, M. Ferrario, M. Belleveglia, G. Di Pirro, G. Gatti, C. Vaccarezza, B. Seitz, R. C. Isaac, E. Brunetti, S. M. Wiggins, B. Ersfeld, M. R. Islam, M. S. Mendonca, A. Sorensen, M. Boyd, and D. A. Jaroszynski. Dosimetry of very high energy electrons (VHEE) for radiotherapy applications: Using radiochromic film measurements and Monte Carlo simulations. *Physics in Medicine and Biology*, 59(19):5811–5829, 2014.

[58] Felix Horst. Calorimetry as a tool to improve the dosimetric accuracy in novel radiotherapy modalities. *Physics and Imaging in Radiation Oncology*, 28:100516, October 2023.

[59] L J Schreiner. Review of fricke gel dosimeters. *Journal of Physics: Conference Series*, 3:9–21, January 2004.

[60] D. J. La Russa and D. W. O. Rogers. Accuracy of spencer-attix cavity theory and calculations of fluence correction factors for the air kerma formalism. *Medical Physics*, 36(9Part1):4173–4183, August 2009.

[61] Peter R. Almond, Peter J. Biggs, B. M. Coursey, W. F. Hanson, M. Saiful Huq, Ravinder Nath, and D. W. O. Rogers. Aapm's tg-51 protocol for clinical reference dosimetry of high-energy photon and electron beams. *Medical Physics*, 26(9):1847–1870, September 1999.

[62] C.-M. Ma, C. W. Coffey, L. A. DeWerd, C. Liu, R. Nath, S. M. Seltzer, and J. P. Seuntjens. Aapm protocol for 40–300 kv x-ray beam dosimetry in radiotherapy and radiobiology. *Medical Physics*, 28(6):868–893, June 2001.

[63] Danielle Fraser, William Parker, and Jan Seuntjens. Characterization of cylindrical ionization chambers for patient specific imrt qa. *Journal of Applied Clinical Medical Physics*, 10(4):241–251, September 2009.

[64] C.N. De Souza, L.V.E. Caldas, C.H. Sibata, A.K. Ho, and K.H. Shin. Two new parallel-plate ionization chambers for electron beam dosimetry. *Radiation Measurements*, 26(1):65–74, January 1996.

[65] N F Silva, M Xavier, V Vivolo, and L V E Caldas. Characterization of a free air ionization chamber for low energy x-rays. *Journal of Physics: Conference Series*, 733:012090, July 2016.

[66] Elise Konradsson, Crister Ceberg, Michael Lempart, Börje Blad, Sven Bäck, Tommy Knöös, and Kristoffer Petersson. Correction for ion recombination in a built-in monitor chamber of a clinical linear accelerator at ultra-high dose rates. *Radiation Research*, 194(6), June 2020.

[67] Kristoffer Petersson, Maud Jaccard, Jean François Germond, Thierry Buchillier, François Bochud, Jean Bourhis, Marie Catherine Vozenin, and Claude Bailat. High dose-per-pulse electron beam dosimetry -A model to correct for the ion recombination in the advanced markus ionization chamber. *Medical Physics*, 44(3):1157–1167, 2017.

[68] Martin J Butson, Tsang Cheung, and Peter K.N. Yu. Weak energy dependence of ebt gafchromic film dose response in the 50kvp–10mvp x-ray range. *Applied Radiation and Isotopes*, 64(1):60–62, January 2006.

[69] Slobodan Devic, Nada Tomic, and David Lewis. Reference radiochromic film dosimetry: Review of technical aspects. *Physica Medica*, 32(4):541–556, April 2016.

[70] Antony L Palmer and David Nash. Radiochromic film dosimetry in radiotherapy: a survey of current practice in the united kingdom. *British Journal of Radiology*, 97(1155):646–651, January 2024.

[71] David Lewis, Andre Micke, Xiang Yu, and Maria F. Chan. An efficient protocol for radiochromic film dosimetry combining calibration and measurement in a single scan. *Medical Physics*, 39(10):6339–6350, September 2012.

[72] Michelle E. Howard, Michael G. Herman, and Michael P. Grams. Methodology for radiochromic film analysis using filmqa pro and imagej. *PLOS ONE*, 15(5):e0233562, May 2020.

[73] Pierluigi Casolaro. Radiochromic films for the two-dimensional dose distribution assessment. *Applied Sciences*, 11(5):2132, February 2021.

[74] Hideharu Miura, Shuichi Ozawa, Fumika Hosono, Naoki Sumida, Toshiya Okazue, Kiyoshi Yamada, and Yasushi Nagata. Gafchromic EBT-XD film: Dosimetry characterization in high-dose, volumetric-modulated arc therapy. *Journal of Applied Clinical Medical Physics*, 17(6):312–322, 2016.

[75] Pierluigi Casolaro, Luigi Campajola, Giovanni Breglio, Salvatore Buontempo, Marco Consales, Andrea Cusano, Antonello Cutolo, Francesco Di Capua, Francesco Fienga, and Patrizio Vaiano. Real-time dosimetry with radiochromic films. *Scientific Reports*, 9(1), March 2019.

[76] Martin A Ebert, Ali H Asad, and Salim A Siddiqui. Suitability of radiochromic films for dosimetry of low energy x-rays. *Journal of Applied Clinical Medical Physics*, 10(4):232–240, September 2009.

[77] Daphnée Villoing, Charbel Koumeir, Arthur Bongrand, Arnaud Guertin, Ferid Haddad, Vincent Métivier, Freddy Poirier, Vincent Potiron, Noël Servagent, Stéphane Supiot, Grégory Delpon, and Sophie Chiavassa. Technical note: Proton beam dosimetry at ultra-high dose rates (flash): Evaluation of gafchromic™ (ebt3, ebt-xd) and orthochromic (oc-1) film performances. *Medical Physics*, 49(4):2732–2745, March 2022.

[78] J B Birks. Scintillations from Organic Crystals: Specific Fluorescence and Relative Response to Different Radiations. *Proceedings of the Physical Society. Section A*, 64(10):874–877, 1951.

[79] Muhammad Ramish Ashraf, Mahbubur Rahman, Rongxiao Zhang, Benjamin B. Williams, David J. Gladstone, Brian W. Pogue, and Petr Bruza. Dosimetry for FLASH Radiotherapy: A Review of Tools and the Role of Radioluminescence and Cherenkov Emission. *Frontiers in Physics*, 8(August):1–20, 2020.

[80] Joseph J Bateman, Emma Buchanan, Roberto Corsini, Wilfrid Farabolini, Pierre Korysko, Robert Garbrecht Larsen, Alexander Malyzhenkov, Iñaki Ortega Ruiz, Vilde Rieker, Alexander Gerbershagen, and Manjit Dosanjh. Development of a novel fibre

optic beam profile and dose monitor for very high energy electron radiotherapy at ultrahigh dose rates. *Physics in Medicine amp; Biology*, 69(8):085006, April 2024.

[81] William Crookes. CERTAIN PROPERTIES OF THE EMANATIONS OF RADIUM: The Chemical News, 1903.

[82] Carel W.E. Van Eijk. Inorganic scintillators in medical imaging detectors. *Nuclear Instruments and Methods in Physics Research, Section A: Accelerators, Spectrometers, Detectors and Associated Equipment*, 509(1-3):17–25, 2003.

[83] A. Nassalski, M. Kapusta, T. Batsch, D. Wolski, D. Möckel, W. Enghardt, and M. Moszyński. Comparative study of scintillators for PET/CT detectors. *IEEE Transactions on Nuclear Science*, 54(1):3–10, 2007.

[84] C. Lindsay, M. Bazalova-Carter, A. Wang, D. Shedlock, M. Wu, M. Newson, L. Xing, W. Ansbacher, R. Fahrig, and J. Star-Lack. Investigation of combined kv/mv cbct imaging with a high-dqe mv detector. *Medical Physics*, 46(2):563–575, December 2018.

[85] Luc Beaulieu and Sam Beddar. Review of plastic and liquid scintillation dosimetry for photon, electron, and proton therapy. *Physics in Medicine and Biology*, 61(20):R305–R343, 2016.

[86] T.J. Gooding and H.G. Pugh. The response of plastic scintillators to high-energy particles. *Nuclear Instruments and Methods*, 7(2):189–192, May 1960.

[87] Masanori Koshimizu. Recent progress of organic scintillators. *Japanese Journal of Applied Physics*, 62(1):010503, November 2022.

[88] Takeo MURAI, Tadashi NAKAMURA, and Akira YAMAMOTO. A new method of integral dose measurement with a plastic scintillator phantom. *Journal of Radiation Research*, 5(1):23–34, 1964.

[89] Harold Perera, Jeffrey F. Williamson, Suzanne P. Monthofer, Walter R. Binns, Joseph Klarmann, Gary L. Fuller, and John W. Wong. Rapid two-dimensional dose measurement in brachytherapy using plastic scintillator sheet: linearity, signal-to-noise ratio, and energy response characteristics. *International Journal of Radiation Oncology*Biology*Physics*, 23(5):1059–1069, January 1992.

[90] Mathieu Guillot, Luc Beaulieu, Louis Archambault, Sam Beddar, and Luc Gingras. A new water-equivalent 2d plastic scintillation detectors array for the dosimetry of megavoltage energy photon beams in radiation therapy. *Medical Physics*, 38(12):6763–6774, November 2011.

[91] S. Ilie, H. Schönbacher, and M. Tavlet. Radiation-damage measurements on pvt-based plastic scintillators. *Nuclear Physics B - Proceedings Supplements*, 32:384–391, May 1993.

[92] Margaret Bowen, Stan Majewski, David Pettey, James Walker, Randolph Wojcik, and Carl Zorn. A new radiation-hard plastic scintillator. *Nuclear Instruments and Methods in Physics Research Section A: Accelerators, Spectrometers, Detectors and Associated Equipment*, 276(1–2):391–393, March 1989.

[93] Louis Archambault, A Sam Beddar, and René Roy. Measurement accuracy and Cerenkov removal for high performance , high spatial resolution scintillation dosimetry. pages 128–135, 2006.

[94] Jonathan Boivin, Sam Beddar, Maxime Guillemette, and Luc Beaulieu. Systematic evaluation of photodetector performance for plastic scintillation dosimetry. *Medical Physics*, 42(11):6211–6220, October 2015.

[95] Sree Bash Chandra Debnath, Carole Fauquet, Agnes Tallet, Anthony Goncalves, Sébastien Lavandier, Franck Jandard, Didier Tonneau, and Julien Darreon. High spatial resolution inorganic scintillator detector for high-energy X-ray beam at small field irradiation. *Medical Physics*, 47(3):1364–1371, 2020.

[96] Emilie Jean, Francois Therriault-Proulx, and Luc Beaulieu. Comparative optic and dosimetric characterization of the HYPERSCINT scintillation dosimetry research platform for multipoint applications. *Physics in Medicine and Biology*, 66(8), 2021.

[97] Yannick Poirier, Junliang Xu, Sina Mossahebi, François Therriault-Proulx, and Amit Sawant. Technical note: Characterization and practical applications of a novel plastic scintillator for online dosimetry for an ultrahigh dose rate (FLASH). *Medical Physics*, 49(7):4682–4692, 2022.

[98] J B BIRKS. CHAPTER 3 - THE SCINTILLATION PROCESS IN ORGANIC MATERIALS—I. In J B BIRKS, editor, *The Theory and Practice of Scintillation Counting*, International Series of Monographs in Electronics and Instrumentation, pages 39–67. Pergamon, 1964.

[99] Ph Rebourgeard, F Rondeaux, J.P Baton, G Besnard, H Blumenfeld, M Bourdinaud, J Calvet, J.-C Cavan, R Chipaux, A Giganon, J Heitzmann, C Jeanney, P Micolon,

M Neveu, T Pedrol, D Pierrepont, and J.-C Thévenin. Fabrication and measurements of plastic scintillating fibers. *Nuclear Instruments and Methods in Physics Research Section A: Accelerators, Spectrometers, Detectors and Associated Equipment*, 427(3):543–567, May 1999.

[100] Louis Archambault, Jean Arsenault, Luc Gingras, A Sam Beddar, and René Roy. Plastic scintillation dosimetry : Optimal selection of scintillating fibers and scintillators. pages 2271–2278, 2005.

[101] Louis Archambault, Jerimy C Polf, Luc Beaulieu, and Sam Beddar. Characterizing the response of miniature scintillation detectors when irradiated with proton beams. *Physics in Medicine and Biology*, 53(7):1865–1876, March 2008.

[102] J F Williamson, J F Dempsey, A S Kirov, J I Monroe, W R Binns, and H Hedtjärn. Plastic scintillator response to low-energy photons. *Physics in Medicine and Biology*, 44(4):857–871, January 1999.

[103] L L W Wang, L A Perles, L Archambault, N Sahoo, D Mirkovic, and S Beddar. Determination of the quenching correction factors for plastic scintillation detectors in therapeutic high-energy proton beams. *Physics in Medicine and Biology*, 57(23):7767–7781, November 2012.

[104] S F de Boer, A S Beddar, and J A Rawlinson. Optical filtering and spectral measurements of radiation-induced light in plastic scintillation dosimetry. *Physics in Medicine and Biology*, 38(7):945–958, July 1993.

[105] A-M. Frelin, J-M. Fontbonne, G. Ban, J. Colin, M. Labalme, A. Batalla, A. Isambert, A. Vela, and T. Leroux. Spectral discrimination of Čerenkov radiation in scintillating dosimeters. *Medical Physics*, 32(9):3000–3006, August 2005.

[106] J.M. Fontbonne, G. Iltis, G. Ban, A. Battala, J.C. Vernhes, J. Tillier, N. Bellaize, C. Le Brun, B. Tamain, K. Mercier, and J.C. Motin. Scintillating fiber dosimeter for radiation therapy accelerator. *IEEE Transactions on Nuclear Science*, 49(5):2223–2227, October 2002.

[107] François Therriault-Proulx, Luc Beaulieu, Louis Archambault, and Sam Beddar. On the nature of the light produced within PMMA optical light guides in scintillation fiber-optic dosimetry. *Physics in Medicine and Biology*, 58(7):2073–2084, 2013.

[108] Louis Archambault, A. Sam Beddar, Luc Gingras, Fréderic Lacroix, René Roy, and Luc Beaulieu. Water-equivalent dosimeter array for small-field external beam radiotherapy. *Medical Physics*, 34(5):1583–1592, April 2007.

[109] Sam Beddar, T.R. Mackie, and F.H. Attix. Cerenkov light generated in optical fibres and other light pipes irradiated by electron beams. *Physics in Medicine & Biology*, 37:925 – 935, 1992.

[110] R Nowotny. Radioluminescence of some optical fibres. *Physics in Medicine and Biology*, 52(4):N67–N73, January 2007.

[111] Francesco Romano, Claude Bailat, Patrik Gonçalves Jorge, Michael Lloyd Franz Lerch, and Arash Darafsheh. Ultra-high dose rate dosimetry: Challenges and opportunities for FLASH radiation therapy. *Medical Physics*, 49(7):4912–4932, 2022.

[112] Vincent Favaudon, Rudi Labarbe, and Charles L. Limoli. Model studies of the role of oxygen in the flash effect. *Medical Physics*, 49(3):2068–2081, August 2021.

[113] Gabriel Adrian, Elise Konradsson, Michael Lempart, Sven Bäck, Crister Ceberg, and Kristoffer Petersson. The FLASH effect depends on oxygen concentration. *The British Journal of Radiology*, 93(1106):20190702, feb 2020.

[114] Jian Yue Jin, Anxin Gu, Weili Wang, Nancy L. Oleinick, Mitchell Machtay, and Feng Ming (Spring) Kong. Ultra-high dose rate effect on circulating immune cells: A potential mechanism for FLASH effect? *Radiotherapy and Oncology*, 149:55–62, 2020.

[115] Antje Galts and Abdelkhalek Hammi. Flash radiotherapy sparing effect on the circulating lymphocytes in pencil beam scanning proton therapy: impact of hypofractionation and dose rate. *Physics in Medicine amp; Biology*, 69(2):025006, January 2024.

[116] Alan Perstin, Yannick Poirier, Amit Sawant, and Mauro Tambasco. Quantifying the dna-damaging effects of flash irradiation with plasmid dna. *International Journal of Radiation Oncology*Biology*Physics*, 113(2):437–447, June 2022.

[117] Christian R. Cooper, Donald Jones, George Dd Jones, and Kristoffer Petersson. FLASH irradiation induces lower levels of DNA damage ex vivo, an effect modulated by oxygen tension, dose, and dose rate. *British Journal of Radiology*, 95(1133), 2022.

[118] Felix Horst, Elisabeth Bodenstein, Michael Brand, Stefan Hans, Leonhard Karsch, Elisabeth Lessmann, Steffen Löck, Michael Schürer, Jörg Pawelke, and Elke Beyreuther.

Dose and dose rate dependence of the tissue sparing effect at ultra-high dose rate studied for proton and electron beams using the zebrafish embryo model. *Radiotherapy and Oncology*, 194(February), 2024.

[119] Michele M. Kim, Arash Darafsheh, Jan Schuemann, Ivana Dokic, Olle Lundh, Tianyu Zhao, Jose Ramos-Mendez, Lei Dong, and Kristoffer Petersson. Development of Ultra-High Dose-Rate (FLASH) Particle Therapy. *IEEE Transactions on Radiation and Plasma Medical Sciences*, 6(3):252–262, mar 2022.

[120] Charles L Limoli and Marie-Catherine Vozenin. Reinventing Radiobiology in the Light of FLASH Radiotherapy. *Annual Review of Cancer Biology*, 7(Volume 7, 2023):1–21, 2023.

[121] D L Dewey and J W Boag. Modification of the oxygen effect when bacteria are given large pulses of radiation. *Nature (London)*, 183(4673):1450–1451, 1959.

[122] SHIRLEY HORNSEY and TIKVAH ALPER. Unexpected dose-rate effect in the killing of mice by radiation. *Nature*, 210(5032):212–213, April 1966.

[123] Shirley Hornsey and D.K. Bewley. Hypoxia in mouse intestine induced by electron irradiation at high dose-rates. *International Journal of Radiation Biology and Related Studies in Physics, Chemistry and Medicine*, 19(5):479–483, January 1971.

[124] S.B. Field and D.K. Bewley. Effects of dose-rate on the radiation response of rat skin. *International Journal of Radiation Biology and Related Studies in Physics, Chemistry and Medicine*, 26(3):259–267, January 1974.

[125] C. D. TOWN. Effect of high dose rates on survival of mammalian cells. *Nature*, 215(5103):847–848, August 1967.

[126] Roger J. Berry, Eric J. Hall, David W. Forster, Thomas H. Storr, and Michael J. Goodman. Survival of mammalian cells exposed to x rays at ultra-high dose-rates. *The British Journal of Radiology*, 42(494):102–107, February 1969.

[127] Erratum for the Research Article: "Ultrahigh dose-rate FLASH irradiation increases the differential response between normal and tumor tissue in mice" by V. Favaudon, L. Caplier, V. Monceau, F. Pouzoulet, M. Sayarath, C. Fouillade, M.-F. Poupon, I. Brito, P. Hupé, J. Bourhis, J. Hall, J.-J. Fontaine, M.-C. Vozenin. *Science Translational Medicine*, 11(523):eaba4525, 2019.

[128] Pierre Montay-gruel, Audrey Bouchet, Maud Jaccard, David Patin, Raphael Serduc, Warren Aim, Kristoffer Petersson, Benoit Petit, Claude Bailat, Jean Bourhis, Elke Bräuer-krisch, and Marie-catherine Vozenin. X-rays can trigger the FLASH effect : Ultra-high dose-rate synchrotron light source prevents normal brain injury after whole brain irradiation in mice. *Radiotherapy and Oncology*, 129(3):582–588, 2018.

[129] Carla Rohrer Bley, Friederike Wolf, Patrik Gonçalves Jorge, Veljko Grilj, Ioannis Petridis, Benoit Petit, Till T. Böhlen, Raphael Moeckli, Charles Limoli, Jean Bourhis, Valeria Meier, and Marie-Catherine Vozenin. Dose- and volume-limiting late toxicity of flash radiotherapy in cats with squamous cell carcinoma of the nasal planum and in mini pigs. *Clinical Cancer Research*, 28(17):3814–3823, April 2022.

[130] Jonathan Farr, Veljko Grilj, Victor Malka, Srinivasan Sudharsan, and Marco Schippers. Ultra-high dose rate radiation production and delivery systems intended for flash. *Medical Physics*, 49(7):4875–4911, May 2022.

[131] Jean Bourhis, Pierre Montay-Gruel, Patrik Gonçalves Jorge, Claude Bailat, Benoît Petit, Jonathan Ollivier, Wendy Jeanneret-Sozzi, Mahmut Ozsahin, François Bochud, Raphaël Moeckli, Jean François Germond, and Marie Catherine Vozenin. Clinical translation of FLASH radiotherapy: Why and how? *Radiotherapy and Oncology*, 139(xxxx):11–17, 2019.

[132] Johanna Ramroth, David J. Cutter, Sarah C. Darby, Geoff S. Higgins, Paul McGale, Mike Partridge, and Carolyn W. Taylor. Dose and fractionation in radiation therapy of curative intent for non-small cell lung cancer: Meta-analysis of randomized trials. *International Journal of Radiation Oncology*Biology*Physics*, 96(4):736–747, November 2016.

[133] Brita Singers Sørensen, Eleni Kanouta, Christina Ankjærgaard, Line Kristensen, Jacob G. Johansen, Mateusz Krzysztof Sitarz, Claus E. Andersen, Cai Grau, and Per Poulsen. Proton flash: Impact of dose rate and split dose on acute skin toxicity in a murine model. *International Journal of Radiation Oncology*Biology*Physics*, 120(1):265–275, September 2024.

[134] Emily C Daugherty, Anthony Mascia, Yong Zhang, Eunsin Lee, Zhiyan Xiao, Mathieu Sertorio, Jennifer Woo, Claire McCann, Kenneth Russell, Lisa Levine, Ricky Sharma, Deepak Khuntia, Jeffrey Bradley, Charles B Simone II, John Perentesis, and John Breneman. FLASH Radiotherapy for the Treatment of Symptomatic Bone Metas-

tases (FAST-01): Protocol for the First Prospective Feasibility Study. *JMIR Research Protocols*, 12:e41812, 2023.

[135] Yuan Gao, Ruirui Liu, Chih-Wei Chang, Serdar Charyyev, Jun Zhou, Jeffrey D. Bradley, Tian Liu, and Xiaofeng Yang. A potential revolution in cancer treatment: A topical review of flash radiotherapy. *Journal of Applied Clinical Medical Physics*, 23(10), September 2022.

[136] O. Zlobinskaya, C. Siebenwirth, C. Greubel, V. Hable, R. Hertenberger, N. Humble, S. Reinhardt, D. Michalski, B. Röper, G. Multhoff, G. Dollinger, J. J. Wilkens, and T. E. Schmid. The effects of ultra-high dose rate proton irradiation on growth delay in the treatment of human tumor xenografts in nude mice. *Radiation Research*, 181(2):177–183, February 2014.

[137] N. Rama, T. Saha, S. Shukla, C. Goda, D. Milewski, A.E. Mascia, R.E. Vatner, D. Sengupta, A. Katsis, E. Abel, S. Girdhani, M. Miyazaki, A. Rodriguez, A. Ku, R. Dua, R. Parry, and T.V. Kalin. Improved tumor control through t-cell infiltration modulated by ultra-high dose rate proton flash using a clinical pencil beam scanning proton system. *International Journal of Radiation Oncology*Biology*Physics*, 105(1):S164–S165, September 2019.

[138] Eric S. Diffenderfer, Ioannis I. Verginadis, Michele M. Kim, Khayrullo Shoniyozov, Anastasia Velalopoulou, Denisa Goia, Mary Putt, Sarah Hagan, Stephen Avery, Kevin Teo, Wei Zou, Alexander Lin, Samuel Swisher-McClure, Cameron Koch, Ann R. Kennedy, Andy Minn, Amit Maity, Theresa M. Busch, Lei Dong, Costas Koumenis, James Metz, and Keith A. Cengel. Design, implementation, and in vivo validation of a novel proton flash radiation therapy system. *International Journal of Radiation Oncology*Biology*Physics*, 106(2):440–448, February 2020.

[139] Karen Levy, Suchitra Natarajan, Jinghui Wang, Stephanie Chow, Joshua T. Eggold, Phoebe E. Loo, Rakesh Manjappa, Stavros Melemenidis, Frederick M. Lartey, Emil Schüler, Lawrie Skinner, Marjan Rafat, Ryan Ko, Anna Kim, Duaa H. Al-Rawi, Rie von Eyben, Oliver Dorigo, Kerriann M. Casey, Edward E. Graves, Karl Bush, Amy S. Yu, Albert C. Koong, Peter G. Maxim, Billy W. Loo, and Erinn B. Rankin. Abdominal flash irradiation reduces radiation-induced gastrointestinal toxicity for the treatment of ovarian cancer in mice. *Scientific Reports*, 10(1), December 2020.

[140] Shannon Cunningham, Shelby McCauley, Kanimozhi Vairamani, Joseph Speth, Swati Girdhani, Eric Abel, Ricky A. Sharma, John P. Perentesis, Susanne I. Wells, Anthony

Mascia, and Mathieu Sertorio. Flash proton pencil beam scanning irradiation minimizes radiation-induced leg contracture and skin toxicity in mice. *Cancers*, 13(5):1012, March 2021.

[141] Sara Chabi, Thi Hong Van To, Ron Leavitt, Sandrine Poglio, Patrik Gonçalves Jorge, Maud Jaccard, Kristoffer Petersson, Benoit Petit, Paul-Henri Roméo, Françoise Pflumio, Marie-Catherine Vozenin, and Benjamin Uzan. Ultra-high-dose-rate flash and conventional-dose-rate irradiation differentially affect human acute lymphoblastic leukemia and normal hematopoiesis. *International Journal of Radiation Oncology*Biology*Physics*, 109(3):819–829, March 2021.

[142] Billy W. Loo, Emil Schuler, Frederick M. Lartey, Marjan Rafat, Gregory J. King, Stefania Trovati, Albert C. Koong, and Peter G. Maxim. (p003) delivery of ultra-rapid flash radiation therapy and demonstration of normal tissue sparing after abdominal irradiation of mice. *International Journal of Radiation Oncology*Biology*Physics*, 98(2):E16, June 2017.

[143] Danielle A. Simmons, Frederick M. Lartey, Emil Schüler, Marjan Rafat, Gregory King, Anna Kim, Ryan Ko, Sarah Semaan, Selena Gonzalez, Melissa Jenkins, Pooja Pradhan, Zion Shih, Jinghui Wang, Rie von Eyben, Edward E. Graves, Peter G. Maxim, Frank M. Longo, and Billy W. Loo. Reduced cognitive deficits after flash irradiation of whole mouse brain are associated with less hippocampal dendritic spine loss and neuroinflammation. *Radiotherapy and Oncology*, 139:4–10, October 2019.

[144] E. Abel, S. Girdhani, I. Jackson, J. Eley, A. Katsis, A. Marshall, A. Rodriguez, S. Senapati, S.M. Bentzen, Z. Vujaskovic, R. Dua, and R. Parry. Characterization of radiation-induced lung fibrosis and mode of cell death using single and multi-pulsed proton flash irradiation. *International Journal of Radiation Oncology*Biology*Physics*, 105(1):E652–E653, September 2019.

[145] Bhanu Prasad Venkatesulu, Amrish Sharma, Julianne M. Pollard-Larkin, Ramaswamy Sadagopan, Jessica Symons, Shinya Neri, Pankaj K. Singh, Ramesh Tailor, Steven H. Lin, and Sunil Krishnan. Ultra high dose rate (35gy/sec) radiation does not spare the normal tissue in cardiac and splenic models of lymphopenia and gastrointestinal syndrome. *Scientific Reports*, 9(1), November 2019.

[146] Qixian Zhang, Ethan Cascio, Chengming Li, Qingyuan Yang, Leo E. Gerweck, Peigen Huang, Bernard Gottschalk, Jacob Flanz, and Jan Schuemann. Flash investigations

using protons: Design of delivery system, preclinical setup and confirmation of flash effect with protons in animal systems. *Radiation Research*, 194(6), August 2020.

[147] Yasaman Alaghband, Samantha N. Cheeks, Barrett D. Allen, Pierre Montay-Gruel, Ngoc-Lien Doan, Benoit Petit, Patrik Goncalves Jorge, Erich Giedzinski, Munjal M. Acharya, Marie-Catherine Vozenin, and Charles L. Limoli. Neuroprotection of radiosensitive juvenile mice by ultra-high dose rate flash irradiation. *Cancers*, 12(6):1671, June 2020.

[148] Charles Fouillade, Sandra Curras-Alonso, Lorena Giuranno, Eddy Quelennec, Sophie Heinrich, Sarah Bonnet-Boissinot, Arnaud Beddok, Sophie Leboucher, Hamza Umut Karakurt, Mylène Bohec, Sylvain Baulande, Marc Vooijs, Pierre Verrelle, Marie Dutreix, Arturo Londoño-Vallejo, and Vincent Favaudon. Flash irradiation spares lung progenitor cells and limits the incidence of radio-induced senescence. *Clinical Cancer Research*, 26(6):1497–1506, March 2020.

[149] Anastasia Velalopoulou, Ilias V. Karagounis, Gwendolyn M. Cramer, Michele M. Kim, Giorgos Skoufos, Denisa Goia, Sarah Hagan, Ioannis I. Verginadis, Khayrullo Shoniyozov, June Chiango, Michelle Cerullo, Kelley Varner, Lutian Yao, Ling Qin, Artemis G. Hatzigeorgiou, Andy J. Minn, Mary Putt, Matthew Lanza, Charles-Antoine Assenmacher, Enrico Radaelli, Jennifer Huck, Eric Diffenderfer, Lei Dong, James Metz, Constantinos Koumenis, Keith A. Cengel, Amit Maity, and Theresa M. Busch. Flash proton radiotherapy spares normal epithelial and mesenchymal tissues while preserving sarcoma response. *Cancer Research*, 81(18):4808–4821, July 2021.

[150] Jia-ling Ruan, Carl Lee, Shari Wouters, Iain D C Tullis, Mieke Verslegers, Mohamed Mysara, Chee Kin Then, Sean C Smart, Mark A Hill, Ruth J Muschel, Amato J Giaccia, Borivoj Vojnovic, Anne E Kiltie, and Kristoffer Petersson. Irradiation at Ultra-High (FLASH) Dose Rates Reduces Acute Normal Tissue Toxicity in the Mouse Gastrointestinal System. *International Journal of Radiation Oncology, Biology, Physics*, 111(5):1250–1261, 2021.

[151] Lloyd M. L. Smyth, Jacqueline F. Donoghue, Jessica A. Ventura, Jayde Livingstone, Tracy Bailey, Liam R. J. Day, Jeffrey C. Crosbie, and Peter A. W. Rogers. Comparative toxicity of synchrotron and conventional radiation therapy based on total and partial body irradiation in a murine model. *Scientific Reports*, 8(1), August 2018.

[152] Pierre Montay-Gruel, Munjal M. Acharya, Kristoffer Petersson, Leila Alikhani, Chakradhar Yakkala, Barrett D. Allen, Jonathan Ollivier, Benoit Petit, Pa-

trik Gonçalves Jorge, Amber R. Syage, Thuan A. Nguyen, Al Anoud D. Baddour, Celine Lu, Paramvir Singh, Raphael Moeckli, François Bochud, Jean-François Germond, Pascal Froidevaux, Claude Bailat, Jean Bourhis, Marie-Catherine Vozenin, and Charles L. Limoli. Long-term neurocognitive benefits of flash radiotherapy driven by reduced reactive oxygen species. *Proceedings of the National Academy of Sciences*, 116(22):10943–10951, May 2019.

[153] Elke Beyreuther, Michael Brand, Stefan Hans, Katalin Hideghéty, Leonhard Karsch, Elisabeth Leßmann, Michael Schürer, Emília Rita Szabó, and Jörg Pawelke. Feasibility of proton flash effect tested by zebrafish embryo irradiation. *Radiotherapy and Oncology*, 139:46–50, October 2019.

[154] Jörg Pawelke, Michael Brand, Stefan Hans, Katalin Hideghéty, Leonhard Karsch, Elisabeth Lessmann, Steffen Löck, Michael Schürer, Emília Rita Szabó, and Elke Beyreuther. Electron dose rate and oxygen depletion protect zebrafish embryos from radiation damage. *Radiotherapy and Oncology*, 158:7–12, May 2021.

[155] Manuela Buonanno, Veljko Grilj, and David J. Brenner. Biological effects in normal cells exposed to flash dose rate protons. *Radiotherapy and Oncology*, 139:51–55, October 2019.

[156] Mathieu Gaudreault, Adam Yeo, Tomas Kron, Gerard G. Hanna, Shankar Siva, and Nicholas Hardcastle. Treatment time optimization in single fraction stereotactic ablative radiation therapy: A 10-year institutional experience. *Advances in Radiation Oncology*, 7(5):100829, September 2022.

[157] M. C. Vozenin, J. H. Hendry, and C. L. Limoli. Biological Benefits of Ultra-high Dose Rate FLASH Radiotherapy: Sleeping Beauty Awoken. *Clinical Oncology*, 31(7):407–415, 2019.

[158] D. L. Dewey. An oxygen-dependent x-ray dose-rate effect in serratia marcescens. *Radiation Research*, 38(3):467–474, 1969.

[159] C. Clifton Ling, Howard B. Michaels, Edward R. Epp, and Eleanor C. Peterson. Oxygen diffusion into mammalian cells following ultrahigh dose rate irradiation and lifetime estimates of oxygen-sensitive species. *Radiation Research*, 76(3):522–532, 1978.

[160] Eric J Hall and James D Cox. Chapter 1 - Physical and Biologic Basis of Radiation Therapy. In James D Cox and K Kian Ang, editors, *Radiation Oncology (Ninth Edition)*, pages 3–49. Mosby, Philadelphia, ninth edition edition, 2010.

[161] Guillem Pratx and Daniel S Kapp. A computational model of radiolytic oxygen depletion during flash irradiation and its effect on the oxygen enhancement ratio. *Physics in Medicine amp; Biology*, 64(18):185005, September 2019.

[162] Hans Liew, Stewart Mein, Ivana Dokic, Thomas Haberer, Jürgen Debus, Amir Abdollahi, and Andrea Mairani. Deciphering time-dependent dna damage complexity, repair, and oxygen tension: A mechanistic model for flash-dose-rate radiation therapy. *International Journal of Radiation Oncology*Biology*Physics*, 110(2):574–586, June 2021.

[163] Kristoffer Petersson, Gabriel Adrian, Karl Butterworth, and Stephen J. McMahon. A quantitative analysis of the role of oxygen tension in flash radiation therapy. *International Journal of Radiation Oncology*Biology*Physics*, 107(3):539–547, July 2020.

[164] Daria Boscolo, Emanuele Scifoni, Marco Durante, Michael Krämer, and Martina C. Fuss. May oxygen depletion explain the flash effect? a chemical track structure analysis. *Radiotherapy and Oncology*, 162:68–75, September 2021.

[165] Rudi Labarbe, Lucian Hotoiu, Julie Barbier, and Vincent Favaudon. A physicochemical model of reaction kinetics supports peroxyl radical recombination as the main determinant of the flash effect. *Radiotherapy and Oncology*, 153:303–310, December 2020.

[166] Patrick M O'Grady and Rob DeSalle. Phylogeny of the genus drosophila. *Genetics*, 209(1):1–25, January 2018.

[167] Farzana Khan Perveen. *Introduction to Drosophila*. InTech, February 2018.

[168] Mateusz Mołoń, Jan Dampc, Monika Kula-Maximenko, Jacek Zebrowski, Agnieszka Mołoń, Ralph Dobler, Roma Durak, and Andrzej Skoczowski. Effects of temperature on lifespan of drosophila melanogaster from different genetic backgrounds: Links between metabolic rate and longevity. *Insects*, 11(8):470, July 2020.

[169] Jorge V. Beira and Renato Paro. The legacy of drosophila imaginal discs. *Chromosoma*, 125(4):573–592, May 2016.

[170] Nicholas E Baker. Mechanisms of cell competition emerging from drosophila studies. *Current Opinion in Cell Biology*, 48:40–46, October 2017.

[171] Daxiang Yang. Carnivory in the larvae of drosophila melanogaster and other drosophila species. *Scientific Reports*, 8(1), October 2018.

[172] David I Thwaites and John B Tuohy. Back to the future: the history and development of the clinical linear accelerator. *Physics in Medicine and Biology*, 51(13):R343–R362, June 2006.

[173] H. J. Muller. The Production of Mutations by X-Rays. *Proceedings of the National Academy of Sciences*, 14(9):714–726, 1928.

[174] AXEL R OLSON and GILBERT N LEWIS. Natural Reactivity and the Origin of Species. *Nature*, 121(3052):673–674, 1928.

[175] Frank Blair Hanson and Florence Heys. A Possible Relation Between Natural (Earth) Radiation and Gene Mutations. *Science*, 71(1828):43–44, 1930.

[176] Edward J. Calabrese. On the origins of the linear no-threshold (LNT) dogma by means of untruths, artful dodges and blind faith. *Environmental Research*, 142:432–442, 2015.

[177] A. A. Moskalev, E. N. Plyusnina, and M. V. Shaposhnikov. Radiation hormesis and radioadaptive response in Drosophila melanogaster flies with different genetic backgrounds: The role of cellular stress-resistance mechanisms. *Biogerontology*, 12(3):253–263, 2011.

[178] A Porrazzo, F Cipressa, A De Gregorio, C De Pittà, G Sales, G Esposito, M A Tabocchini, G Cenci, and L Ciapponi. Low dose rate $\hat{\mathrm{I}}^{3}$-irradiation protects fruit fly chromosomes from double strand breaks and telomere fusions by reducing the esi-RNA biogenesis factor Loquacious. pages 1–12, 2022.

[179] Cha Soon Kim, Ki Moon Seong, Byung Sub Lee, In Kyung Lee, Kwang Hee Yang, Ji Young Kim, and Seon Young Nam. Chronic low-dose γ-irradiation of Drosophila melanogaster larvae induces gene expression changes and enhances locomotive behavior. *Journal of Radiation Research*, 56(3):475–484, 2015.

[180] Takao Koana, Takashi Takahashi, and Hidenobu Tsujimura. Reduction of spontaneous somatic mutation frequency by a low-dose x irradiation of drosophila larvae and possible involvement of DNA single-strand damage repair. *Radiation Research*, 177(3):265–271, 2012.

[181] Trudy F. C. Mackay, Stephen Richards, Eric A. Stone, Antonio Barbadilla, Julien F. Ayroles, Dianhui Zhu, Sònia Casillas, Yi Han, Michael M. Magwire, Julie M. Cridland, Mark F. Richardson, Robert R. H. Anholt, Maite Barrón, Crystal Bess, Kerstin Petra Blankenburg, Mary Anna Carbone, David Castellano, Lesley Chaboub, Laura Duncan,

Zeke Harris, Mehwish Javaid, Joy Christina Jayaseelan, Shalini N. Jhangiani, Katherine W. Jordan, Fremiet Lara, Faye Lawrence, Sandra L. Lee, Pablo Librado, Raquel S. Linheiro, Richard F. Lyman, Aaron J. Mackey, Mala Munidasa, Donna Marie Muzny, Lynne Nazareth, Irene Newsham, Lora Perales, Ling-Ling Pu, Carson Qu, Miquel Ràmia, Jeffrey G. Reid, Stephanie M. Rollmann, Julio Rozas, Nehad Saada, Lavanya Turlapati, Kim C. Worley, Yuan-Qing Wu, Akihiko Yamamoto, Yiming Zhu, Casey M. Bergman, Kevin R. Thornton, David Mittelman, and Richard A. Gibbs. The drosophila melanogaster genetic reference panel. *Nature*, 482(7384):173–178, February 2012.

[182] Udai Bhan Pandey and Charles D. Nichols. Human disease models indrosophila melanogasterand the role of the fly in therapeutic drug discovery. *Pharmacological Reviews*, 63(2):411–436, March 2011.

[183] F. Froldi, M. Ziosi, G. Tomba, F. Parisi, F. Garoia, A. Pession, and D. Grifoni. Drosophila lethal giant larvae neoplastic mutant as a genetic tool for cancer modeling. *Current Genomics*, 9(3):147–154, May 2008.

[184] Daniel F. Woods and Peter J. Bryant. The discs-large tumor suppressor gene of drosophila encodes a guanylate kinase homolog localized at septate junctions. *Cell*, 66(3):451–464, August 1991.

[185] Izarne Medina, Manuel Calleja, and Ginés Morata. Tumorigenesis and cell competition in drosophila in the absence of polyhomeotic function. *Proceedings of the National Academy of Sciences*, 118(45), October 2021.

[186] Yun Fan and Andreas Bergmann. Apoptosis-induced compensatory proliferation. the cell is dead. long live the cell! *Trends in Cell Biology*, 18(10):467–473, October 2008.

[187] John L. Haynie and Peter J. Bryant. The effects of x-rays on the proliferation dynamics of cells in the imaginal wing disc of drosophila melanogaster. *Wilhelm Roux's Archives of Developmental Biology*, 183(2):85–100, 1977.

[188] Anita Wichmann, Burnley Jaklevic, and Tin Tin Su. Ionizing radiation induces caspase-dependent but Chk2- and p53-independent cell death in Drosophila melanogaster. *Proceedings of the National Academy of Sciences of the United States of America*, 103(26):9952–9957, 2006.

[189] W. H. Mae, T. A. Stone, I. Jerman, J. Bolton, H. Bolton, B. C. Goodwin, P. T. Saunders, and F. Robertson. Brief exposures to weak static magnetic field during early

embryogenesis cause cuticular pattern abnormalities in Drosophila larvae. *Physics in Medicine and Biology*, 37(5):1171–1179, 1992.

[190] Cayetano Gonzalez. Drosophila melanogaster: A model and a tool to investigate malignancy and identify new therapeutics. *Nature Reviews Cancer*, 13(3):172–183, 2013.

[191] Carole Poon, Anthony Brumby, and Helena Richardson. Src cooperates with oncogenic ras in tumourigenesis via the jnk and pi3k pathways in drosophila epithelial tissue. *International Journal of Molecular Sciences*, 19(6):1585, May 2018.

[192] Chamoné Munnik, Malungi P. Xaba, Sibusiso T. Malindisa, Bonnie L. Russell, and Selisha A. Sooklal. Drosophila melanogaster: A platform for anticancer drug discovery and personalized therapies. *Frontiers in Genetics*, 13, August 2022.

[193] Zhasmine Mirzoyan, Manuela Sollazzo, Mariateresa Allocca, Alice Maria Valenza, Daniela Grifoni, and Paola Bellosta. Drosophila melanogaster: A model organism to study cancer. *Frontiers in Genetics*, 10, March 2019.

[194] Nolan Esplen, Marc S. Mendonca, and Magdalena Bazalova-Carter. Physics and biology of ultrahigh dose-rate (FLASH) radiotherapy: A topical review. *Physics in Medicine and Biology*, 65(23), 2020.

[195] Jonathan R. Hughes and Jason L. Parsons. Flash radiotherapy: Current knowledge and future insights using proton-beam therapy. *International Journal of Molecular Sciences*, 21(18):1–14, 2020.

[196] Pierre Montay-Gruel, Stéphanie Corde, Jean A Laissue, and Magdalena Bazalova-Carter. Flash radiotherapy with photon beams. *Medical Physics*, 49(3):2055–2067, November 2021.

[197] P. Fournier, J. C. Crosbie, I. Cornelius, P. Berkvens, M. Donzelli, A. H. Clavel, A. B. Rosenfeld, M. Petasecca, M. L.F. Lerch, and E. Bräuer-Krisch. Absorbed dose-to-water protocol applied to synchrotron-generated x-rays at very high dose rates. *Physics in Medicine and Biology*, 61(14):N349–N361, 2016.

[198] Małgorzata Liszka, Liliana Stolarczyk, Magdalena Kłodowska, Anna Kozera, Dawid Krzempek, Natalia Mojzeszek, Anna Pdracka, Michael Patrick Russell Waligórski, and Paweł Olko. Ion recombination and polarity correction factors for a plane-parallel ionization chamber in a proton scanning beam. *Medical Physics*, 45(1):391–401, 2018.

[199] Annalisa Patriarca, Charles Fouillade, Michel Auger, Frédéric Martin, Frédéric Pouzoulet, Catherine Nauraye, Sophie Heinrich, Vincent Favaudon, Samuel Meyroneinc, Rémi Dendale, Alejandro Mazal, Philip Poortmans, Pierre Verrelle, and Ludovic De Marzi. Experimental Set-up for FLASH Proton Irradiation of Small Animals Using a Clinical System. *International Journal of Radiation Oncology Biology Physics*, 102(3):619–626, 2018.

[200] Maud Jaccard, Kristoffer Petersson, Thierry Buchillier, Jean François Germond, Maria Teresa Durán, Marie Catherine Vozenin, Jean Bourhis, François O. Bochud, and Claude Bailat. High dose-per-pulse electron beam dosimetry: Usability and dose-rate independence of EBT3 Gafchromic films: Usability. *Medical Physics*, 44(2):725–735, 2017.

[201] Patrik Gonçalves Jorge, Maud Jaccard, Kristoffer Petersson, Maude Gondré, Maria Teresa Durán, Laurent Desorgher, Jean François Germond, Philippe Liger, Marie Catherine Vozenin, Jean Bourhis, François Bochud, Raphaël Moeckli, and Claude Bailat. Dosimetric and preparation procedures for irradiating biological models with pulsed electron beam at ultra-high dose-rate. *Radiotherapy and Oncology*, 139:34–39, 2019.

[202] Louis Archambault, Tina M. Briere, Falk Pönisch, Luc Beaulieu, Deborah A. Kuban, Andrew Lee, and Sam Beddar. Toward a real-time in vivo dosimetry system using plastic scintillation detectors. *International Journal of Radiation Oncology Biology Physics*, 78(1):280–287, 2010.

[203] Yu N. Kharzheev. Radiation Hardness of Scintillation Detectors Based on Organic Plastic Scintillators and Optical Fibers. *Physics of Particles and Nuclei*, 50(1):42–76, 2019.

[204] Chanho Kim, Wonhi Lee, Alima Melis, Abdallah Elmughrabi, Kisung Lee, and Chansun Park. A Review of Inorganic Scintillation Crystals for Extreme Environments. *Crystals*, 11(6):669, 2021.

[205] I Kawrakow, DWO Rogers, E Mainegra-Hing, F Tessier, RW Townson, and BRB Walters. Egsnrc toolkit for monte carlo simulation of ionizing radiation transport. doi:10.4224/40001303 [release v2021], 2000.

[206] J. Perl, J. Shin, J. Schumann, B. Faddegon, and H. Paganetti. TOPAS: An innovative proton Monte Carlo platform for research and clinical applications. *Medical Physics*, 39:6818, 2012.

[207] B. Faddegon, J. Ramos-Mendez, J. Schuemann, A. McNamara, J. Shin, J. Perl, and Paganetti H. The TOPAS Tool for Particle Simulation, a Monte Carlo Simulation Tool for Physics, Biology and Clinical Research. *Physica Medica*, 2020.

[208] Imke Schoepper, Sonja Dieterich, Earl Alonzo Trestrail, and Michael Sean Kent. Preclinical and clinical evaluation of the HYPERSCINT plastic scintillation dosimetry research platform for in vivo dosimetry during radiotherapy. *Journal of Applied Clinical Medical Physics*, 2022.

[209] Felix Y. Feng, Hyungjin M. Kim, Teresa H. Lyden, Marc J. Haxer, Mary Feng, Frank P. Worden, Douglas B. Chepeha, and Avraham Eisbruch. Intensity-Modulated Radiotherapy of Head and Neck Cancer Aiming to Reduce Dysphagia: Early Dose-Effect Relationships for the Swallowing Structures. *International Journal of Radiation Oncology Biology Physics*, 68(5):1289–1298, 2007.

[210] Jacques Bernier, Eric J Hall, and Amato Giaccia. Radiation oncology: a century of achievements. *Nature reviews. Cancer*, 4(9):737–747, 2004.

[211] Lucas Schoenauen, François Xavier Stubbe, Dirk Van Gestel, Sébastien Penninckx, and Anne Catherine Heuskin. C. elegans: A potent model for high-throughput screening experiments investigating the FLASH effect. *Clinical and Translational Radiation Oncology*, 45(November 2023), 2024.

[212] Sarah Rudigkeit, Thomas E Schmid, Annique C Dombrowsky, Jessica Stolz, Stefan Bartzsch, Ce-Belle Chen, Nicole Matejka, Matthias Sammer, Andreas Bergmaier, Günther Dollinger, and Judith Reindl. Proton-FLASH: effects of ultra-high dose rate irradiation on an in-vivo mouse ear model. *Scientific Reports*, 14(1):1418, 2024.

[213] Cameron Davidson-Pilon. lifelines: survival analysis in python. *Journal of Open Source Software*, 4(40):1317, August 2019.

[214] C. M. Ma, C. W. Coffey, L. A. DeWerd, C. Liu, R. Nath, S. M. Seltzer, and J. P. Seuntjens. AAPM protocol for 40-300 kV x-ray beam dosimetry in radiotherapy and radiobiology. *Medical Physics*, 28(6):868–893, 2001.

[215] Till Tobias Böhlen, Jean François Germond, Jean Bourhis, Marie Catherine Vozenin, Esat Mahmut Ozsahin, François Bochud, Claude Bailat, and Raphaël Moeckli. Normal Tissue Sparing by FLASH as a Function of Single-Fraction Dose: A Quantitative Analysis. *International Journal of Radiation Oncology Biology Physics*, 114(5):1032–1044, 2022.

[216] Jagdish Gopal Paithankar, K. Deeksha, and Rajashekhar K. Patil. Gamma radiation tolerance in different life stages of the fruit fly Drosophila melanogaster. *International Journal of Radiation Biology*, 93(4):440–448, 2017.

[217] Lisa J. Sudmeier, Steven P. Howard, and Barry Ganetzky. A Drosophila model to investigate the neurotoxic side effects of radiation exposure. *DMM Disease Models and Mechanisms*, 8(7):669–677, 2015.

[218] Koichiro Nakajima, Tian Xiang Gao, Kazuhiko Kume, Hiromitsu Iwata, Shuichi Hirai, Chihiro Omachi, Jun Tomita, Hiroyuki Ogino, Munekazu Naito, and Yuta Shibamoto. Fruit Fly, Drosophila melanogaster, as an in Vivo Tool to Study the Biological Effects of Proton Irradiation. *Radiation Research*, 194(2):143–152, 2020.

[219] C. DesRosiers, V. Moskvin, A. F. Bielajew, and L. Papiez. 150-250 MeV electron beams in radiation therapy. *Physics in Medicine and Biology*, 45(7):1781–1805, 2000.

[220] L. Whitmore, R. I. Mackay, M. van Herk, J. K. Jones, and R. M. Jones. Focused VHEE (very high energy electron) beams and dose delivery for radiotherapy applications. *Scientific Reports*, 11(1):1–14, 2021.

[221] Pierre Montay-Gruel, Audrey Bouchet, Maud Jaccard, David Patin, Raphael Serduc, Warren Aim, Kristoffer Petersson, Benoit Petit, Claude Bailat, Jean Bourhis, Elke Bräuer-Krisch, and Marie Catherine Vozenin. X-rays can trigger the FLASH effect: Ultra-high dose-rate synchrotron light source prevents normal brain injury after whole brain irradiation in mice. *Radiotherapy and Oncology*, 129(3):582–588, 2018.

[222] Anna A. Friedl, Kevin M. Prise, Karl T. Butterworth, Pierre Montay-Gruel, and Vincent Favaudon. Radiobiology of the FLASH effect. *Medical Physics*, 49(3):1993–2013, 2022.

[223] Nolan Esplen, Luca Egoriti, Bill Paley, Thomas Planche, Cornelia Hoehr, Alexander Gottberg, and Magdalena Bazalova-Carter. Design optimization of an electron-to-photon conversion target for ultra-high dose rate x-ray (FLASH) experiments at TRIUMF. *Physics in Medicine and Biology*, 67(10), 2022.

[224] Michele M. Kim, Arash Darafsheh, Jan Schuemann, Ivana Dokic, Olle Lundh, Tianyu Zhao, Jose Ramos-Mendez, Lei Dong, and Kristoffer Petersson. Development of Ultra-High Dose-Rate (FLASH) Particle Therapy. *IEEE Transactions on Radiation and Plasma Medical Sciences*, 6(3):252–262, mar 2022.

[225] M. McManus, F. Romano, N. D. Lee, W. Farabolini, A. Gilardi, G. Royle, H. Palmans, and A. Subiel. The challenge of ionisation chamber dosimetry in ultra-short pulsed high dose-rate Very High Energy Electron beams. *Scientific Reports*, 10(1):1–11, 2020.

[226] Vincent Favaudon, Jean Michel Lentz, Sophie Heinrich, Annalisa Patriarca, Ludovic de Marzi, Charles Fouillade, and Marie Dutreix. Time-resolved dosimetry of pulsed electron beams in very high dose-rate, FLASH irradiation for radiotherapy preclinical studies. *Nuclear Instruments and Methods in Physics Research, Section A: Accelerators, Spectrometers, Detectors and Associated Equipment*, 944(March):162537, 2019.

[227] Eleni Kanouta, Jacob Graversen Johansen, Gustavo Kertzscher, Mateusz Krzysztof Sitarz, Brita Singers Sørensen, and Per Rugaard Poulsen. Time structure of pencil beam scanning proton FLASH beams measured with scintillator detectors and compared with log files. *Medical Physics*, 49(3):1932–1943, 2022.

[228] Mahbubur Rahman, M. Ramish Ashraf, Rongxiao Zhang, Petr Bruza, Chad A. Dexter, Lawrence Thompson, Xu Cao, Benjamin B. Williams, P. Jack Hoopes, Brian W. Pogue, and David J. Gladstone. Electron FLASH Delivery at Treatment Room Isocenter for Efficient Reversible Conversion of a Clinical LINAC. *International Journal of Radiation Oncology Biology Physics*, 110(3):872–882, 2021.

[229] Michael Martyn, Wern Kam, Peter Woulfe, and Sinead O'Keeffe. Water Phantom Characterization of a Novel Optical Fiber Sensor for LDR Brachytherapy. *IEEE Sensors Journal*, 23(2):1146–1156, 2023.

[230] Kevin Byrne, Majed Alharbi, Nolan Esplen, Peter Woulfe, Sinead O'Keeffe, Magdalena Bazalova-Carter, and Mark Foley. Initial Evaluation of the Performance of Novel Inorganic Scintillating Detectors for Small Animal Irradiation Dosimetry. *IEEE sensors journal*, 20(9):4704–4712, 2020.

[231] Shahirah Shaharuddin, Alexander Hart, Daniel D. Cecchi, Magdalena Bazalova-Carter, and Mark Foley. Real-time dosimetry of ultrahigh dose-rate x-ray beams using scintillation detectors. In *2021 IEEE Sensors*, pages 1–4, 2021.

[232] CHUV, CERN and THERYQ partner to develop cancer radiotherapy device, 2022.

[233] Pierre Korysko. C-Robot Gibtlab Repository https://gitlab.cern.ch/CLEAR/arduino4d$_r$*obot*/.

[234] Pauli Virtanen, Ralf Gommers, Travis E. Oliphant, Matt Haberland, Tyler Reddy, David Cournapeau, Evgeni Burovski, Pearu Peterson, Warren Weckesser, Jonathan

Bright, Stéfan J. van der Walt, Matthew Brett, Joshua Wilson, K. Jarrod Millman, Nikolay Mayorov, Andrew R.J. Nelson, Eric Jones, Robert Kern, Eric Larson, C. J. Carey, İlhan Polat, Yu Feng, Eric W. Moore, Jake VanderPlas, Denis Laxalde, Josef Perktold, Robert Cimrman, Ian Henriksen, E. A. Quintero, Charles R. Harris, Anne M. Archibald, Antônio H. Ribeiro, Fabian Pedregosa, Paul van Mulbregt, Aditya Vijaykumar, Alessandro Pietro Bardelli, Alex Rothberg, Andreas Hilboll, Andreas Kloeckner, Anthony Scopatz, Antony Lee, Ariel Rokem, C. Nathan Woods, Chad Fulton, Charles Masson, Christian Häggström, Clark Fitzgerald, David A. Nicholson, David R. Hagen, Dmitrii V. Pasechnik, Emanuele Olivetti, Eric Martin, Eric Wieser, Fabrice Silva, Felix Lenders, Florian Wilhelm, G. Young, Gavin A. Price, Gert Ludwig Ingold, Gregory E. Allen, Gregory R. Lee, Hervé Audren, Irvin Probst, Jörg P. Dietrich, Jacob Silterra, James T. Webber, Janko Slavič, Joel Nothman, Johannes Buchner, Johannes Kulick, Johannes L. Schönberger, José Vinícius de Miranda Cardoso, Joscha Reimer, Joseph Harrington, Juan Luis Cano Rodríguez, Juan Nunez-Iglesias, Justin Kuczynski, Kevin Tritz, Martin Thoma, Matthew Newville, Matthias Kümmerer, Maximilian Bolingbroke, Michael Tartre, Mikhail Pak, Nathaniel J. Smith, Nikolai Nowaczyk, Nikolay Shebanov, Oleksandr Pavlyk, Per A. Brodtkorb, Perry Lee, Robert T. McGibbon, Roman Feldbauer, Sam Lewis, Sam Tygier, Scott Sievert, Sebastiano Vigna, Stefan Peterson, Surhud More, Tadeusz Pudlik, Takuya Oshima, Thomas J. Pingel, Thomas P. Robitaille, Thomas Spura, Thouis R. Jones, Tim Cera, Tim Leslie, Tiziano Zito, Tom Krauss, Utkarsh Upadhyay, Yaroslav O. Halchenko, and Yoshiki Vázquez-Baeza. SciPy 1.0: fundamental algorithms for scientific computing in Python. *Nature Methods*, 17(3):261–272, 2020.

[235] Verdi Vanreusel, Alessia Gasparini, Federica Galante, Giulia Mariani, Matteo Pacitti, Madalina Cociorb, Andrea Giammanco, Brigitte Reniers, Nathalie Reulens, Tunde Blessed Shonde, Hugo Vallet, Dirk Vandenbroucke, Marc Peeters, Paul Leblans, Biwu Ma, Giuseppe Felici, Dirk Verellen, and Luana de Freitas Nascimento. Point scintillator dosimetry in ultra-high dose rate electron "FLASH" radiation therapy: A first characterization. *Physica Medica*, 103(April):127–137, 2022.

[236] Arash Darafsheh, Rongxiao Zhang, Stephen Chad Kanick, Brian W. Pogue, and Jarod C. Finlay. Spectroscopic separation of Čerenkov radiation in high-resolution radiation fiber dosimeters. *Journal of Biomedical Optics*, 20(9):095001, 2015.

[237] M. Ramish Ashraf, Mahbubur Rahman, Xu Cao, Kayla Duval, Benjamin B. Williams, P. Jack Hoopes, David J. Gladstone, Brian W. Pogue, Rongxiao Zhang, and Petr

Bruza. Individual pulse monitoring and dose control system for pre-clinical implementation of FLASH-RT. *Physics in Medicine and Biology*, 67(9), 2022.

[238] Bianey Palma, Magdalena Bazalova-Carter, Björn Hårdemark, Elin Hynning, Bradley Qu, Billy W Loo, and Peter G Maxim. Assessment of the quality of very high-energy electron radiotherapy planning. *Radiotherapy and oncology*, 119(1):154–158, 2016.

[239] Emil Schüler, Kjell Eriksson, Elin Hynning, Steven L Hancock, Susan M Hiniker, Magdalena Bazalova-Carter, Tony Wong, Quynh-Thu Le, Billy W Loo Jr., and Peter G Maxim. Very high-energy electron (VHEE) beams in radiation therapy; Treatment plan comparison between VHEE, VMAT, and PPBS. *Medical Physics*, 44(6):2544–2555, 2017.

[240] Magdalena Bazalova-Carter, Michael Liu, Bianey Palma, Michael Dunning, Doug McCormick, Erik Hemsing, Janice Nelson, Keith Jobe, Eric Colby, Albert C. Koong, Sami Tantawi, Valery Dolgashev, Peter G. Maxim, and Billy W. Loo. Comparison of film measurements and Monte Carlo simulations of dose delivered with very high-energy electron beams in a polystyrene phantom. *Medical Physics*, 42(4):1606–1613, 2015.

[241] Nathan Clements, Nolan Esplen, and Magdalena Bazalova-Carter. A feasibility study of ultra-high dose rate mini-GRID therapy using very-high-energy electron beams for a simulated pediatric brain case. *Physica Medica*, 112(February):102637, 2023.

[242] Rachel Delorme, Thongchai A.M. Masilela, Camille Etoh, François Smekens, and Yolanda Prezado. First theoretical determination of relative biological effectiveness of very high energy electrons. *Scientific Reports*, 11(1):1–13, 2021.

[243] Hannah C. Wanstall, Florian Burkart, Hannes Dinter, Max Kellermeier, Willi Kuropka, Frank Mayet, Thomas Vinatier, Elham Santina, Amy L. Chadwick, Michael J. Merchant, Nicholas T. Henthorn, Michael Köpke, Blae Stacey, Sonja Jaster-Merz, and Roger M. Jones. First in vitro measurement of vhee relative biological effectiveness (rbe) in lung and prostate cancer cells using the ares linac at desy. *Scientific Reports*, 14(1), May 2024.

[244] K. Ilicic, G. Dollinger, A. Dombrowsky, C. Greubel, S. Girst, M. Sammer, C. Siebenwirth, E. Schmid, T. Friedrich, P. Kundrát, W. Friedland, M. Scholz, S. E. Combs, T. E. Schmid, and J. Reindl. Enhanced RBE of Particle Radiation Depends on Beam Size in the Micrometer Range. *Radiation research*, 201(2):140–149, 2024.

[245] V. Favaudon, C. Fouillade, and M. C. Vozenin. Radiothérapie flash à très haut débit de dose: Un moyen d'augmenter l'indice thérapeutique par minimisation des dommages aux tissus sains ? *Cancer/Radiotherapie*, 19(6-7):526–531, 2015.

[246] Stanislaw Szpala, Vicky Huang, Yingli Zhao, Alastair Kyle, Andrew Minchinton, Tania Karan, and Kirpal Kohli. Dosimetry with a clinical linac adapted to FLASH electron beams. *Journal of Applied Clinical Medical Physics*, 22(6):50–59, 2021.